This is to certify that the
dissertation entitled

INTEGRATING MULTISPECTRAL REFLECTANCE AND
FLUORESCENCE IMAGING FOR APPLE DISORDER
CLASSIFICATION

presented by

Diwan Prima Ariana

has been accepted towards fulfillment
of the requirements for the

Ph.D. degree in Biosystems Engineering

Major Professor's Signature

May 14, 2004

Date

MSU is an Affirmative Action/Equal Opportunity Institution

INTEGRATING MULTISPECTRAL REFLECTANCE AND FLUORESCENCE IMAGING FOR APPLE DISORDER CLASSIFICATION

By

Diwan Prima Ariana

A DISSERTATION

Submitted to
Michigan State University
in partial fulfillment of the requirements
for the degree of

DOCTOR OF PHILOSOPHY

Department of Agricultural Engineering

2004

ABSTRACT

INTEGRATING MULTISPECTRAL REFLECTANCE AND FLUORESCENCE IMAGING FOR APPLE DISORDER CLASSIFICATION

By

Diwan Prima Ariana

Multispectral imaging in reflectance and fluorescence modes was used to classify various types of apple disorder from three apple varieties (Honeycrisp, Redcort, and Red Delicious). Eighteen images from a combination of filter sets ranging from the visible region through the NIR region and three different imaging modes (reflectance, visible light induced fluorescence, and UV induced fluorescence) were acquired for each apple as a basis for pixel-level classification into normal or disorder tissue. Two classification schemes, a 2-class and a multiple class, combined with four different classifiers, nearest neighbor, neural network, linear discriminant function and quadratic discriminant function, were developed and tested in this study. In the 2-class scheme, pixels were categorized into normal or disorder tissue, whereas in the multiple class scheme, pixels were categorized into normal, bitter pit, black rot, decay, soft scald, and superficial scald tissues.

Total classification accuracy of the nearest neighbor classifier under the 2-class scheme for the full model, using all eighteen images, was 99.1, 96.8, 95.9, and 99.2% for Honeycrisp, Redcort, Red Delicious, and combined variety respectively. Furthermore, in the multiple-class scheme, the classification accuracy of Honeycrisp apple for normal, bitter pit, black rot, decay, and soft scald was 98.7, 99.3, 98.9, 98.5, and 100%

respectively. These results indicate the potential of this technique to accurately recognize different types of disorder.

Performance result comparison of the four classifiers demonstrated that for Honeycrisp and combined variety, the nearest neighbor classifier yielded the highest accuracy followed by neural network, linear discriminant and quadratic discriminant classifiers. However, there were no significant differences among the classifiers on Redcort and Red Delicious.

Feature selection analysis to develop reduced-feature models was carried out through three different approaches, i.e. imaging mode combinations, filter combinations, and feature combinations. Imaging mode combinations analysis indicates a potential of integrating UV induced fluorescence and reflectance mode. Furthermore, the use of UV induced fluorescence alone has a potential to detect superficial scald in Red Delicious, and was able to classify black rot and soft scald on Honeycrisp with high accuracy, 100 and 99.4% respectively. Several important wavelengths were identified from the filter combination analysis, i.e. 680, 740, 905 nm. Reflectance at 680 nm relates to red color, and fluorescence response at 680 and 740 nm relates to the peaks of chlorophyll fluorescence emission, whereas the 905 NIR responses may relate to tissue physical characteristics. Feature combination analysis found the best 4-feature model resulted in total accuracy up to 96.6%, 98.8%, and 99.4% for Honeycrisp, Redcort, and Red Delicious respectively.

Dedication

To my mother Tien Kartinasarie and my father Undi Syamsuddin,

who both passed away during my graduate study in Michigan State University.

ACKNOWLEDGMENTS

I would like to express my deepest appreciation and gratitude to my major professor, Dr. Daniel E. Guyer for the time and effort he devoted to me. His valuable guidance and assistance was essential to completing my Ph.D. degree. I appreciate the research assistantship given by Michigan State University through Dr. Guyer.

I would also like to thank the members of my committee, Dr. Renfu Lu, USDA; Dr. Randolph Beaudry, Department of Horticulture; and Dr. Clark Radcliffe, Department of Mechanical Engineering, for their support and timely advice. Gracious appreciation is extended to Dr. Roger Brook for his guidance and who has served as my major professor in the first four years of my study at Michigan State University.

I would like to thank The Department of Animal Science through Dr. Mike VandeHaar and Mr. Robert Kriegel for giving me research assistantships. I extend my great appreciations to The Indonesian Oil Palm Research Institute (IOPRI), who allowed me to continue my graduate study in US and initially supported my graduate study.

I would like to thank Dr. Bim Shrestha, member of our research group, for his suggestions and help throughout my research project. I also wish to acknowledge Dr. Sastry Jayanty and Melissa from The Postharvest Technology and Physiology Laboratory, Department of Horticulture who help me identify disorders on apples.

Finally, deepest appreciation to my beloved wife Endang Susilawati, my beloved sons Ega Prima, Fakhri Pranayanda, and Kevin Triananda, and my parents-in-law for their help, sacrifices, understanding, and patience during my graduate study.

TABLE OF CONTENTS

LIST OF TABLES

LIST OF FIGURES

1. INTRODUCTION

1.1. Background

Internal and external quality are important factors in the highly competitive market of stored apples. Important quality criteria for consumers are: appearance, including size, color, and shape; texture; flavor; nutritional value; and presence of defects or disorders. Many factors influence the quality, but can be generally categorized into preharvest, harvest, and postharvest factors.

Quality classification of fruits is an important procedure in marketing and processing. In the past, segregation of high- and low-quality fruit was performed manually, but in modern packinghouses it is performed automatically, although mainly is still limited to sorting fruit by color and size. Since manual fruit grading has drawbacks such as subjectivity, inconsistency, tediousness, labor availability, and cost, efforts to develop efficient and accurate automated fruit classification systems continue to be industry priorities.

Automated sorting technology can sort fruit and vegetables rapidly and consistently. Electronic sorting technology is in place, or is available, for sorting many commodity quality characteristics. The most sophisticated optical or electronic sorting equipment available today can sort with "good" accuracy. However, the ability to detect surface and sub-surface defects, disorders, and diseases is limited. This limitation results particularly from a lack of data on the spectral range, or set of ranges, needed to adequately detect as well as classify surface and sub-surface disorders.

Considerable work in the area of noninvasive / nondestructive techniques to inspect fruits and vegetables has been conducted. The techniques include surface reflectance and transmittance of various forms of (ultraviolet, visible, NIR, MIR) light energy, acoustic response, mechanical deformation, x-ray, computed tomography (CT), fluorescence, and magnetic resonance imaging (MRI). Diffuse reflectance in visible (VIS) and NIR regions provides useful information to detect bruises, chilling injury, scald, decay lesions, and numerous other defects (Abbott, 1999).

Diffuse reflectance measurement using spectrometers has been widely implemented in a variety of applications; however, spectroscopic assessment with relatively small point-source measurements has disadvantages compared to an imaging approach that characterizes the spatial variability of a sample material (Kim *et al.*, 2001b). In particular, imaging techniques are better suited for the detection of localized effects of a sample material.

Imaging techniques have been successfully used for classification or sorting of agricultural products. One of the imaging techniques that has been widely used is multi and hyperspectral imaging that captures a set of images at different wavelengths. Multispectral and hyperspectral imaging techniques have been adopted in many disciplines, such as airborne remote sensing, environmental monitoring, medicine, military operations, factory automation and manufacturing (Gat *et al.*, 1997; Shaw and Manolakis, 2002). In agricultural product quality assessment, the techniques have been studied for inspection of poultry carcasses (Park *et al.*, 1998), chicken skin tumor detection (Chao *et al.*, 2002), defect detection on cherries (Guyer and Yang, 2000), apples (Kavdir and Guyer, 2002; Lu, 2003; Mehl *et al.*, 2002), citrus (Aleixos *et al.*, 2002), and tomatoes (Polder *et al.*, 2002). Hyperspectral imaging techniques currently cannot be directly implemented in an online system for agricultural product sorting because the time required for image acquisition and analysis is too long. Multispectral imaging is a faster technique based on discrete spectral analysis at a few wavelengths as opposed to the continuous spectral analysis used in hyperspectral imaging (Mehl *et al.*, 2002).

Most of the studies in hyperspectral and multispectral imaging for agricultural product inspection involve reflectance imaging. An alternative, or additional inspection technique is fluorescence imaging. Chlorophyll fluorescence in plant/leaf tissue has been studied extensively but only recently has been applied to fruit post-harvest physiology and to even lesser degree to physical surface defects arising from handling or disorders. A fluorometer, which doesn't provide spatial information as in fluorescence imaging, was used in the majority of the studies of chlorophyll fluorescence. DeEll et al. (1999) summarized much of the past work related to fluorescence studies. The majority of the work focused on stress or disorders involving whole plant or whole commodity response, such as chilling injury, heat stress, environmental stress and maturity, with limited study on disorders which involve localized or smaller areas of the surface tissue. Several chlorophyll fluorescence studies on apples have been reported, such as in relation to superficial scald development (Mir et al., 1998), heat injury (Song *et al.*, 2001), freezing injury (Forney *et al.*, 2000), controlled-atmosphere disorders (DeEll *et al.*, 1995), and maturation (Song *et al.*, 1997).

Most plant leaves, when illuminated with UV radiation, exhibit a broad fluorescence emission with maxima at 440, 525, 685, and 740 nm (Chappelle *et al.*, 1985). These fluorescence emissions are indicative of the complex interactions of both physiological and biochemical processes in plants. Changes in fluorescence emission in response to environmental perturbations can be wavelength dependent and are usually species dependent as well. A multispectral fluorescence imaging system with UV excitation has been developed by Kim et al. (2001b) to capture fluorescence images of leaves in the blue, green, red, and far-red regions of the spectrum, using band pass filters centered at 450, 550, 680, and 740 nm respectively.

1.2. Objectives and Hypothesis

Although multispectral reflectance and fluorescence imaging have individually been studied widely in a variety of applications, most of the studies related to object classifications only deal with one of the two imaging modes at a time. Integrating reflectance and fluorescence information in the classification model may improve the classification accuracy considering both reflectance and fluorescence images carry different information as a result of interaction of light energy and matter. Therefore, the main objective of this study was to develop a detection technique for defects on apples based on integrated multispectral reflectance and fluorescence imaging. To accomplish this overall objective, the following sub-objectives were established:

(1) Design and build a multispectral imaging system to capture images of apples under reflectance and fluorescence imaging modes.

(2) Determine if imaging of light energy reflectance in the visible and near infrared regions, as well as imaging of chlorophyll fluorescence under

both visible and UV excitation, can successfully be used to detect different types of defects or disorders on apples.

(3) Optimize the combination of filters and lighting mode(s) for best classification success.

Integrating reflectance and fluorescence information in a single classification model represents the uniqueness of this study, resulting in the hypothesis that integrated multispectral imaging in reflectance and fluorescence modes can be used to enhance detection of different types of defects or disorders on apples.

2. LITERATURE AND TECHNICAL REVIEW

2.1. Interaction of Light and Matter

The interaction of light and matter is a highly complex phenomenon. The absorbing molecules of matter are excited to specific vibrational states or energy levels dependent on the energy of the incoming radiation. For example, long wavelength radiations (low energy) such as radio or microwaves can excite gases; short wavelength radiations (high energy) such as x-rays affect liquids and solids. According to quantum theory, molecules absorb light in the visible and ultraviolet regions because their electrons can move to higher energy states. Infrared light does not have enough energy to excite electrons in molecules. Instead, excitations resulting in molecular absorption come from vibration and rotation of molecules. Rotational absorption bands are predominantly in the far infrared. Vibrational absorption bands involve the near infrared, which has been applied extensively to component analysis of food and agricultural materials (Muir *et al.*, 1989).

When a light beam falls on an object, part of the incident beam is reflected by the surface and the rest is transmitted into the object where it is either absorbed, reflected back to the surface (body reflectance), or transmitted through the object. Part of the absorbed radiation may be transformed into another form of radiation, such as fluorescence and delayed-light emission (light emitted from the object after the source has been removed). The amounts of radiant energy in the reflectance, transmittance, absorption, or emission depend on the properties of the object and the incident radiation (Chen, 1978). When a fruit or vegetable is exposed to light, about 4% of the incident light is reflected at the outer surface, causing specular reflectance or gloss, and the remaining 96% of the incident energy is transmitted through the surface into the cellular structure of the product where it is scattered by the small interfaces within the tissue or absorbed by cellular constituents (Birth, 1976).

Plant tissues are optically dense, which is difficult to penetrate and alters the path length traveled by the light so that the amount of tissue interrogated is not known with certainty. Most light energy penetrates only a very short distance and exits near the point of entry; this is the basis of color. But some penetrates deeper (usually a few millimeters, depending on optical density) into the tissues and is altered by differential absorbance of various wavelengths before exiting and therefore contains useful chemometric information. Such light may be called diffuse reflectance or body reflectance (Abbott, 1999).

2.2. Spectral Imaging

Machine vision provides automated production processes with vision capabilities. Machine vision can be described as the integration of imaging devices, computers, algorithms, and robotics for automated inspection, characterization, and control. It has been applied widely in many sectors of industries, especially in electronic and automotive, and is increasingly applied in agricultural sectors in recent years.

The most common industrial applications of machine vision are inspection and quality controls. The majority of inspection tasks are highly repetitive and extremely boring, and their effectiveness depends on the efficiency of the human inspector. Since inspection or classification of agricultural products is tedious and repetitive, machine vision and image processing techniques are useful for agricultural and food industry applications, particularly in grading and inspection (Park *et al.*, 1998).

An important part of machine vision is imaging devices along with algorithms to accomplish the purpose of its application, for example to classify objects which are inspected. There are two main imaging systems currently used, the first captures spatial information only, the second captures both spatial and spectral information. While spatial imaging resolves objects into their morphological dimensions, spectral imaging resolves a phenomenon of the interaction of light and objects to be inspected (Park *et al.*, 1998).

Spectral imaging involves measuring the intensity of diffusely reflected light from a surface. The reflected light contains information about the absorbers near the surface of the material that modifies the reflection. By using different wavelengths across a waveband, it is possible to construct a characteristic of spectral features for the material (Muir, 1993). These spectral images are multi-dimensional and the process of distinguishing between them is known as spectral pattern recognition. Spectral imaging also known as imaging spectroscopy, is the application of reflectance/emittance spectroscopy to every pixel in a spatial image.

Multispectral or hyperspectral imaging systems permit acquisition of images at many wavelengths. Multispectral imaging system collects images at few, discrete, noncontiguous wavelengths. On the other hand, hyperspectral images are acquired at hundreds of narrow and contiguous wavelengths. The spectral image dataset can be visualized as a cube, with the X and Y dimensions being the length and width of the image or spatial information (in pixels) and the Z dimension being spectral wavelengths;

each data point is an intensity value. Alternatively, the dataset could be envisioned as a stack of single wavelength pictures of the object, with as many pictures as the number of wavelengths used. Since chemical bonds absorb light energy at specific wavelengths, some compositional information can be determined from spectral data, thus multispectral or hyperspectral imaging provides information about the spatial distribution of constituents (pigments, sugars, moisture, etc.) near the product's surface (Abbott, 1999). Figure 2.1 shows the conceptual representation of spectral imaging.

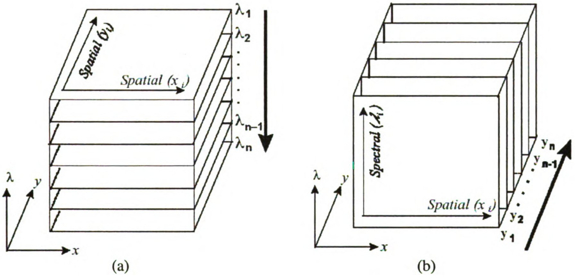

Figure 2.1. Conceptual representation of a volume of hyperspectral image data. Dark arrows indicate directions for sequential acquisitions to complete the volume of spatial and spectral data (Kim *et al.*, 2001a); a) wavelength scanning, b) spatial scanning (pushbroom)

There are two approaches of how a cube of spatial and spectral data can be acquired in spectral imaging. One approach, illustrated in Figure 2.1a, sequentially captures a full spatial scene at each spectral band to form a three-dimensional image cube. Multiple band-pass filters, a liquid-crystal tunable filter, or an acousto-optic tunable filter can be used for this approach. Another approach (Figure 2.1b) is a pushbroom method in which a line of spatial information with a full spectral range per spatial pixel is captured sequentially to complete a volume of spatial-spectral data (Kim *et al.*, 2001a).

2.3. Fluorescence

Fluorescence is the property of some atoms and molecules to absorb light of particular wavelengths and after a brief interval, termed the fluorescence lifetime, to re-emit light at longer wavelengths. Fluorescence requires an outside source of energy, is the result of the absorption of light, and involves the emission of electromagnetic radiation (light). This process is different from chemiluminescence, where the excited state is created via a chemical reaction (Herman, 1998).

Many agricultural materials fluoresce and nearly all horticultural application of fluorescence refers specifically to chlorophyll fluorescence (Abbott, 1999). Chlorophyll appears green to our eyes because it absorbs light in the red and blue parts of the spectrum, so only some of the light enriched in green wavelengths (about 550 nm) is reflected into our eyes. Equation 2.1 represents the absorption of light in which chlorophyll (Chl) in its lowest-energy, or ground, state absorbs a photon (represented by hv) and make a transition to a higher-energy, or excited, state (Chl*).

$$\mathrm{Chl} + h\nu \rightarrow \mathrm{Chl}^* \qquad (2.1)$$

The distribution of electrons in the excited molecule is somewhat different from the distribution in the ground state molecules. Figure 2.2 illustrates the absorption and emission of light by chlorophyll molecules. Absorption of blue light (about 430 nm) excites the chlorophyll to a higher energy state than absorption of red light (about 660 nm), because the energy of photons is higher when their wavelength is shorter. In the higher excited state, chlorophyll is extremely unstable, very rapidly gives up some of its energy to the surrounding as heat, and enters the lowest excited state, where it can be stable for a maximum of several nanoseconds (10^{-9} s) (Taiz and Zeiger, 1998).

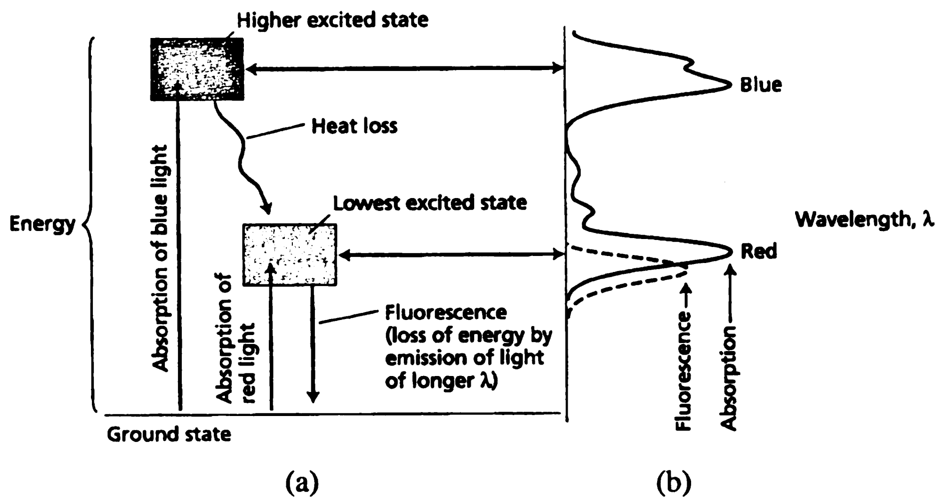

Figure 2.2. Light absorption and emission by chlorophyll (Taiz and Zeiger, 1998); (a) Energy level diagram, (b) the spectra absorption and fluorescence

In the lowest excited state, the excited chlorophyll has several possible pathways for disposing of its available energy such as (Taiz and Zeiger, 1998):

(1) Re-emit a photon and thereby return to its ground state, a process known as fluorescence.

(2) Return to its ground state by directly converting its excitation energy into heat, with no emission of photon.

(3) Transfer its energy to another molecule, a process known as energy transfer.

(4) Cause a chemical reaction to occur, known as photochemistry.

When the excited chlorophylls fluoresce, the wavelength of fluorescence is almost always slightly longer than the wavelength of absorption of the same electron state, because a portion of the excitation energy is converted into heat before the fluorescence photon is emitted. Conservation of energy therefore requires that the energy of the fluorescent photon be lower than that of the excitation photon – hence the shift to longer wavelength, known as stokes shift (Herman, 1998). Chlorophylls fluoresce in the red region of the spectrum.

Chlorophylls can be found in organized pigment/protein complexes in the chloroplast membrane. These protein/pigment complexes are referred to as photosystems I and II, each of which has a 'reaction center' wherein the light energy is converted and utilized. A portion of the absorbed energy is transferred to electrons (from water) in photosystem II (PSII). The electrons are, in turn, used to fuel the reduction of CO_2 to sugar and carbon skeletons in the process of photosynthesis. A small portion of the energy is not used and is reradiated as fluorescence (Mir *et al.*, 1998).

When the intensity of illuminating light is well below the capacity of the tissue to process the energy, PSII is able to pass on nearly all the electrons excited by the light to photosynthetic processes, such that its reaction center is essentially always 'open' for additional energy influx. Under these conditions, the fluorescence intensity is at a minimum, referred to as dark, background, or initial fluorescence (Fo). Conversely, when the intensity of the illuminating light is well above the capacity of the tissue to process the energy, PSII is able to pass on only a fraction of the electrons excited by the light. The reaction center is essentially 'closed' to energy influx and the excited electrons have a tendency to lose their energy as fluorescence. Under these conditions, the fluorescence intensity is at maximum, referred to as maximum fluorescence (Fm). The relationship between these two responses is more commonly expressed as the ratio between the increase in fluorescence from minimal to maximal (Fm-Fo) and the maximal (Fm). The quantity Fm-Fo is often referred to variable fluorescence (Fv). As long as PSII is functioning normally, the ratio of Fm to Fo is usually about 0.8. When PSII is functioning poorly, fluorescence characteristics are altered (Beaudry *et al.*, 1998).

2.4. Apple Disorders

The identification of fruit disorders at harvest, during storage, or after shipping is of utmost importance to producers, shippers, and consumers. Accurate recognition of disorders is needed before problems associated with orchard nutrition, cultural practices, or postharvest treatment can be corrected. In this section, detailed information is given on several apple disorders found in the samples used in this research including bitter pit, soft scald, superficial scald, black rot, and decay. It should be noted that some disorder are difficult for the human eye to distinguish, especially at early stage of disorder development.

2.4.1. Bitter Pit

Bitter pit is a disorder in which small, brown, somewhat dry, slightly bitter tasting lesions 3-5 mm in cross section develop in the flesh of the apple (Figure 2.3). The first symptoms of bitter pit may be small, darkened, slightly depressed spots under the skin, usually in the calyx end of the fruit. The disorder does not affect the skin directly. It may appear before harvest or develop during storage. Internal lesions are often associated with the vascular elements. In severe cases, several lesions may become confluent to form larger necrotic areas. With time, the lesions at the skin darken, sometimes becoming reddish and more sunken, especially in Newton and Golden Delicious (Meheriuk *et al.*, 1994).

Initiation of symptoms may begin four to six weeks after petal fall when affected tissues have a higher rate of respiration and ethylene production. This is a period of greater protein and pectin synthesis with greater migration of organic ions into the affected areas. Affected areas retain starch grains not seen in healthy tissue. A mineral imbalance in the apple flesh develops with low levels of calcium and relatively high concentrations of potassium and magnesium. Low levels of calcium impair the selective permeability of cell membranes leading to cell injury and necrosis (Meheriuk *et al.*, 1994).

Honeycrisp is one of the cultivars that are susceptible to bitter pit. This trait is most pronounced on young, vigorous trees with a small crop load and large fruit. The occurrence of bitter pit is greatly reduced as the trees mature and the crop load increases. Foliar applications of calcium also have proven very effective in preventing bitter pit on Honeycrisp. Avoiding excessive amounts of nitrogen may also help prevent its occurrence (Bedford, 2001).

2.4.2. Soft Scald

Soft scald is easily identified by the sharply defined, irregularly shaped, smooth brown areas in the skin of the apple (Figure 2.3). There may be one or more small lesions, or the disorder may affect most of the apple, irrespective of skin color, but usually not at the stem or calyx end. In its various stages, soft scald affects the skin only, but it may damage hypodermal tissue as the lesion continues to develop (Meheriuk *et al.*, 1994).

Soft scald is a low-temperature-induced disorder of apples. The disorder is likely to occur when highly respiring susceptible cultivars are cooled rapidly. Delayed cooling can advance the onset of the climacteric and thus render the fruit more prone to soft scald upon subsequent rapid cooling. The disorder is prevented if the apples are subjected to 20-30% CO_2 for 2 days during the cooling period (Meheriuk *et al.*, 1994). Dipping the fruit in an aqueous solution containing antioxidants such as diphenylamine (DPA) and edible oil markedly reduce or prevent the disorder (Wills and Scott, 1982).

2.4.3. Superficial Scald

Superficial scald is a postharvest disorder of apples characterized by diffuse browning of the skin, somewhat roughened in severe cases, which become more extensive after a few days at room temperature (Figure 2.3). On red cultivars, the scald lesion is often confined to the unblushed area of the skin (Meheriuk *et al.*, 1994).

A naturally occurring terpene, α-farnesene, has been found in the skin of apples. Its oxidation products are suggested as the cause of superficial scald. Lipoxygenase, in addition to α-farnesene, may be involved in the induction of scald and may be responsible for the browning (Ingle and D'Souza, 1989).

Factors that increase the severity of the disorder include immaturity, high fruit nitrogen, low fruit calcium, warm preharvest weather, delayed cold storage, high storage temperature, high relative humidity in storage, restricted ventilation, extended storage periods and (in controlled atmosphere storage) slow oxygen reduction and high oxygen concentration. Effective treatments to prevent the scald are DPA dips, hot water dips, ethrel sprays, calcium sprays, and fruit coating such as lecithin (Meheriuk *et al.*, 1994).

2.4.4. Decay

Postharvest diseases of fruit crops are caused mostly by fungal infection. The infected tissue, also known as decay, is typically different from surrounding healthy tissue in color and/or texture. In most cases, infected tissue forms a discrete zone, known as a lesion, which extends radially from an infection point in a characteristic pattern determined by the interaction between the host fruit and the pathogen (Figure 2.3). In some postharvest diseases, the border between infected and apparently healthy tissue is sharply defined, in others it is more diffuse (Sugar, 2002). Some of the diseases common on apples along with the causal fungi are: bitter rot (*Glomerella cingulata)*, black rot (*Physalospora obtusa*), gray mold (*Botrytis cinerea*), blue mold (*Penicilium expansum*), bull's-eye rot (*Pezicula malicorticis* (Jacks.)), white rot (*Botryospheria ribis*), flyspeck (*Microthyriella rubi*), and side rot (*Phialophora marolum*) (Pierson *et al.*, 1971).

Organisms rot fruit and vegetables while still immature and attach to the plant or during the harvesting and subsequent handling and marketing operations. The infection process, particularly postharvest, is greatly aided by mechanical injuries to the skin of the produce, such as fingernail scratches and abrasions, rough handling, insect punctures and stem cuts. Furthermore, the physiological condition of the produce, the temperature, and the formation of the periderm significantly affect the infection process and the development of the infection (Wills *et al.*, 1998).

2.4.5. Black Rot

Black rot is identified as a firm brown spot on any part of the apple (Figure 2.3). The affected surface may be marked with concentric zones of different shades of brown, especially if the fruit rotted on the tree. In advanced rots, which can involve the whole fruit, the skin is dark brown or even black and sometimes dotted with numerous small black fungal fruiting bodies called pycnidia. The presence of pycnidia and their random distribution help to distinguish black rot from most other apple rots (Pierson *et al.*, 1971).

The black rot fungus, *Physalospora obtusa*, attacks the leaves, wood, and fruits of apple. While immature fruits may be attacked, the disease is primarily a rot of ripe fruits. Infections may occur at insect injuries and wound sites. Calyx end infections may follow spray and frost injury. Core and calyx end rots may result from fungal invasion of the open calyx tubes in varieties such as Delicious. The disease develops very slowly in green or immature fruits. Black rot ordinarily does not spread from one fruit to another. Black rot should be controlled in the orchard (Pierson *et al.*, 1971).

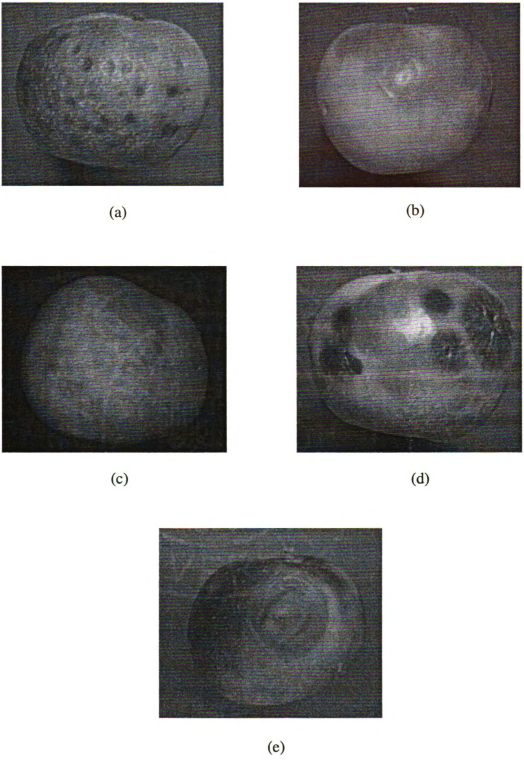

Figure 2.3. Examples of some disorders on apples. (a) bitter pit, (b) soft scald, (c) superficial scald, (d) black rot, (e) decay

2.5. Classification Techniques

Classification, the assignment of an object to one of a number of predetermined groups, is of fundamental importance in many areas of science and technology. For the most part, unless the classification is obvious and trivial we still depend on human expertise to classify on the basis of observation. As the computer has become more and more accessible so it has become attractive to try and use it to either replace the experts or at the very least to guide and help them. Classification is an important component in pattern recognition systems, which usually consists of sensing, segmentation, feature extraction, classification, and post-processing components (Duda *et al.*, 2001). This section will present theoretical background of three classification techniques used in the research, i.e. artificial neural network, discriminant analysis, and k-nearest neighbor.

2.5.1. Artificial Neural Network Classifier

Artificial neural networks (ANN) provide an emerging paradigm for pattern recognition implementation that involves large interconnected networks of relatively simple and typically nonlinear units. A neural network is designed to model the way in which the brain performs a particular task or function of interest. Basically, three entities characterize an ANN (Schalkoff, 1992):

(1) The network topology, or interconnection of neural units,

(2) The characteristics of individual units or artificial neurons, and

(3) The strategy for pattern learning or training.

A neuron is an information-processing unit that is fundamental to the operation of a neural network. The block diagram of Figure 2.4 shows the model of a neuron, which form the basis for designing ANNs. There are three basic elements of the neuronal model:

(1) A set of synapses or connecting links, each of which is characterized by a weight or strength of its own, denoted by w_{kj}. A signal x_j at the input of synapse j connected to neuron k is multiplied by the synaptic weight w_{kj}.

(2) An adder for summing the input signals, weighted by the respective synapses of the neuron; the operation described here constitutes a linear combiner.

(3) An activation function for limiting the amplitude of the output of neuron.

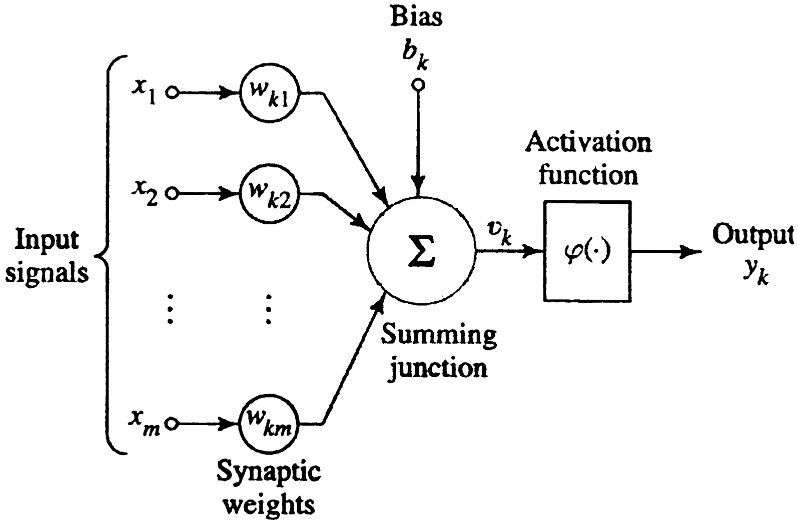

Figure 2.4. Nonlinear model of a neuron (Haykin, 1999)

The neuronal model of Figure 2.4 also includes an externally applied bias, denoted by b_k, which has the effect of increasing or lowering the net input of the activation function, depending on whether it is positive or negative, respectively.

In mathematical terms, we may describe a neuron k by writing the following pair of equations:

$$v_k = \sum_{j=1}^{m} w_{kj} x_j \tag{2.2}$$

and

$$y_k = \varphi(v_k + b_k) \tag{2.3}$$

where $x_1, x_2, \ldots, x_m$ are the input signals; $w_{k1}, w_{k2}, \ldots, w_{km}$ are the synaptic weights of neuron k; v_k is the linear combiner output due to the input signal; b_k is the bias; $\varphi(\cdot)$ is the activation function; and y_k is the output signal of the neuron.

The most common form of activation function used in construction of ANNs is the sigmoid function, whose graph is s-shaped. It is defined as a strictly increasing function that exhibits a graceful balance between linear and nonlinear behavior (Haykin, 1999). An example of the sigmoid function is the logistic function, defined by:

$$\varphi(v) = \frac{1}{1+\exp(-av)} \tag{2.4}$$

where *a* is the slope parameter of the sigmoid function. By varying the parameter *a*, we obtain sigmoid functions of different slopes, as illustrated in Figure 2.5.

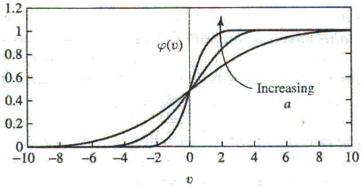

Figure 2.5. Sigmoid function with varying slope parameter a (Haykin, 1999)

Network Architectures

In general, there are three fundamentally different classes of network architectures (Haykin, 1999): (1) single-layer feedforward networks, (2) multilayer feedforward networks, and (3) recurrent networks. A multilayer feedforward network is distinguished from a single-layer feedforward network by the presence of one or more hidden layers, whose computational nodes are correspondingly called hidden neurons or hidden units. The function of hidden neurons is to intervene between the external input and the network output in some useful manner. By adding one or more hidden layers, the network is enabled to extract higher-order statistics, which is valuable when the size of the input layer is large (Haykin, 1999). A recurrent neural network distinguishes itself from a feedforward neural network in that it has at least one feedback loop. The presence of feedback loops has a profound impact on the learning capability of the network and on its performance. Feedforward networks with a back-propagation learning algorithm are commonly used for classification purposes.

Learning Process

A neural network learns about its environment through an interactive process of adjustments applied to its synaptic weights and bias level. Ideally, the network becomes more knowledgeable about its environment after each iteration of the learning process. There are two learning paradigms, first is learning with a teacher or supervised learning and second is learning without a teacher or unsupervised learning. In supervised learning, there is a targeted output to which the neural network approaches. The objective of the learning process is then to minimize the difference between the target output (correct class) and the neural network output by adjusting network parameters. The adjustment is carried out iteratively in a step-by-step fashion with the aim of eventually making the neural network emulate the teacher. In unsupervised learning there is no external teacher to oversee the learning process. Rather, provision is made for a task-independent measure of the quality of representation that the network is required to learn, and the parameters of the network are optimized with respect to that measure (Haykin, 1999).

Pattern recognition or classification tasks are in the category of supervised learning. A neural network performs pattern recognition by first undergoing a training session, during which the neural network is repeatedly presented a set of input patterns along with the category to which each particular pattern belongs. Later, a new pattern is presented to the network that has not been seen before, but which belongs to the same population of patterns used to train the network.

Multilayer feed forward networks, also known as multilayer perceptrons, have been applied successfully to solve some difficult and diverse problems by training them in a supervised manner with a highly popular algorithm known as the error back-propagation algorithm. This algorithm is based on the error-correction learning rule.

Basically, error back-propagation learning consists of two passes through the different layers of the network; a forward pass and a backward pass. In the forward pass, an input vector is applied to the sensory nodes of the network, and its effect propagates through the network layer by layer. Finally, a set of outputs is produced as the actual response of the network. During the forward pass the synaptic weights of the networks are all fixed. During the backward pass, on the other hand, the synaptic weights are all adjusted in accordance with an error-correction rule. Specifically, the actual response of the network is subtracted from a desired (target) response to produce an error signal. This error signal is then propagated backward through the network, against the direction of synaptic connection – hence the name "error back-propagation". The synaptic weights are adjusted to make the actual response of the network move closer to the desired response in a statistical sense. The error back-propagation algorithm is also referred to as the back propagation algorithm. The error signal at the output of neuron j at iteration n is defined by:

$$e_j(n) = d_j(n) - y_j(n) \tag{2.5}$$

where $d_j(n)$ is the target response for neuron j; $y_j(n)$ is the neural network output of neuron j at iteration n.

The back-propagation algorithm applies a correction $\Delta w_{ji}(n)$ to the synaptic weight $w_{ji}(n)$ connecting neuron i to neuron j, which is defined by the delta rule:

$$\Delta w_{ji}(n) = \eta \delta_j(n) y_i(n) \tag{2.6}$$

where η is learning rate parameter; δ_j is local gradient and y_i is input signal of neuron j. The local gradient δ_j depends on whether neuron j is an output node or a hidden node. If neuron j is an output node,

$$\delta_j(n) = e_j(n) \varphi_j'(v_j(n)) \tag{2.7}$$

If neuron j is a hidden node,

$$\delta_j(n) = \varphi_j'(v_j(n)) \sum_k \delta_k(n) w_{kj}(n) \tag{2.8}$$

where k is index for neurons in the next hidden or output layer that are connected to neuron j.

The back-propagation algorithm provides an "approximation" to the trajectory in weight space computed by the method of steepest descent. The smaller we make the learning-rate parameter η, the smaller the changes to the synaptic weights in the network will be from one iteration to the next, and the smoother will be the trajectory in weight space. This improvement, however, is attained at the cost of a slower rate of learning. If, on the other hand, we make the learning-rate parameter η large in order to speed up the rate of learning, the resulting large changes in the synaptic weights cause the network to become unstable. A simple method of increasing the rate of learning yet avoiding the danger of instability is to modify the delta rule of Eq. 2.6 by including a momentum term as shown by (Rumelhart *et al.*, 1986)

$$\Delta w_{ji}(n) = \alpha \Delta w_{ji}(n-1) + \eta \delta_j(n) y_i(n) \tag{2.9}$$

where α is usually a positive number called the momentum constant.

2.5.2. Discriminant Functions

Bayes decision theory is a fundamental statistical approach to the problem of pattern classification (Duda *et al.*, 2001). This approach is based on the assumption that the decision problem is posed in probabilistic terms, and that all of the relevant probability values are known. Bayes decision theory is a basis for developing a discriminant function.

A decision rule partitions a space into regions Ω_i, i=1,...,N, where N is the number of classes. An object is classified as coming from class ω_k if its corresponding vector representation, x, lies in region Ω_k. Bayes rule can be expressed as (Hand, 1981):

$$P(\omega_i \mid x) = \frac{p(x \mid \omega_i)P(\omega_i)}{p(x)} \tag{2.10}$$

where $P(\omega_i \mid x)$ is posterior probability of ω_i given x; $P(\omega_i)$ is a prior probability for class ω_i; $p(x)$ is the probability that x occurs; $p(x \mid \omega_i)$ is a class-conditional probability density function. If $p(x \mid \omega_i)$ are known then the problem is solved – we simply substitute the x vector, for the object to be classified, into equation 2.10 and find the largest value of $p(x \mid \omega_i)P(\omega_i)$. But the $p(x \mid \omega_i)$ are usually unknown and are estimated from the set of classified samples.

If the class-conditional probability density function is assumed Gaussian distributed, then:

$$p(x \mid \omega_i) = \frac{1}{(2\pi)^{d/2} \mid \Sigma \mid^{1/2}} \exp\left[-\frac{1}{2}(x-\mu_i)^T \Sigma^{-1}(x-\mu_i)\right] \tag{2.11}$$

where μ and Σ are mean and covariance matrix of a class. The parameters (μ, Σ) are sufficient to uniquely characterize the normal (Gaussian) distribution. The parameters (μ, Σ) are estimated from the training samples using Maximum Likelihood Estimation (MLE) given as follows:

$$\hat{\mu} = \frac{1}{n}\sum_{i=1}^{n} x_i \tag{2.12}$$

$$\hat{\Sigma} = \frac{1}{n}\sum_{i=1}^{n}(x_i-\mu)(x_i-\mu)^T \tag{2.13}$$

A discriminant function for the i-th class is defined as:

$$g_i(x) = P(\omega_i \mid x) \tag{2.14}$$

Given a feature vector x, the classification rule is based on finding the largest discriminant function. Assuming equal *a priori* probabilities, this means choosing the class for which $p(x|\omega_i)$ is largest. Any monotonically increasing function of $g_i(x)$ is also a valid discriminant function. The log function meets this requirement, that is, an alternative discriminant function is:

$$g_i'(x) = \log\{P(\omega_i \mid x)\} \tag{2.15}$$

$$g_i'(x) = -\frac{1}{2}(x-\mu_i)^T \Sigma_i^{-1}(x-\mu_i) - \frac{1}{2}\log(|\Sigma_i|) + \log(P(\omega_i)) \tag{2.16}$$

Equation 2.16 is known as a Quadratic Discriminant Function. If we further assume that the population covariance matrices Σ_i are all the same, we can simplify the quadratic discriminant score in Equation 2.16 into the linear discriminant score:

$$g_i'(x) = \mu_i^T \Sigma_i x - \frac{1}{2}\mu_i^T \Sigma^{-1}\mu_i + \log(P(\omega_i)) \tag{2.17}$$

2.5.3. Nearest Neighbor Classifier

The Nearest Neighbor (NN) classifier is an example of a nonparametric classifier. Using the label information of the training sample, an unknown observation **x** is compared with all the cases in the training sample. N distances between a pattern vector x and all the training patterns are calculated, and the label information, with which the minimum distance results, is assigned to the pattern **x**. That is, the NN rule allocates the **x** to w_k class if the closest sample $\mathbf{x_c}$ is with the label k =L($\mathbf{x_c}$) (Micheli-Tzanakou, 2000):

$$x_c = \arg\min_i \{d(x_0, x_i)\}, i = 1,2,\ldots,N \tag{2.18}$$

$$x_0 \in w_k = L(x_k) \tag{2.19}$$

The distance measure between the unknown and the training sample has a general quadratic form:

$$d(x, x_k) = (x_0 - x_k)^T M (x_0 - x_k) \tag{2.20}$$

If the Mahalanobis distance is used, M is equal to Σ^{-1}, which is the inverse of the covariance matrix in the sample. If Euclidean distance is used, M is equal to I, which is the identity matrix.

The K-Nearest Neighbor (KNN) rule is the same as the NN rule except that the algorithm finds the K nearest point within the points in the training set from the unknown observation **x** and assigns the class of the unknown observation to the majority class in K points. In the example in Figure 2.6, there are three classes, and the value of K is 5. Of the 5 closest neighbors, 4 belong to ω_1 and 1 belongs to ω_3, so x_u is assigned to ω_1, the predominant class.

The only parameter that should be determined is "K", the number of the nearest neighbors to consider. The value of K depends on the number of training data. With a larger number of samples, larger numbers of K can be chosen.

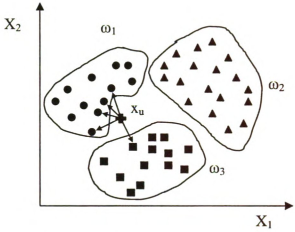

Figure 2.6. 5-Nearest Neighbor classifier in the case of 3 classes

KNN is considered a lazy learning algorithm, which exhibit three characteristics that distinguish them from other learning algorithms: (1) defers processing of their input until they receive requests for information; they simply store their inputs for future use, (2) replies to information requests by combining their stored (training) data, and (3) discards the constructed answer and any intermediate results. In contrast, eager learning algorithms have three characteristics: (1) compiles its input data into a compressed description or model (for example density parameters in statistical pattern recognition and associated weights in neural network pattern recognition, (2) discards the training data after compilation of the model, and (3) classifies incoming patterns using the induced model, which is retained for future requests. There is a tradeoff between the lazy and eager algorithms, lazy algorithms have fewer computational costs than the eager algorithms during training, but they typically have greater storage requirements and higher computational costs on recall (Aha, 1997).

2.6. Feature Selections

For any given classification problem there is an unlimited number of measurements that could be made on the objects to be classified. It is therefore necessary to choose a finite subset of these which leads to good classification results. The most straightforward reason to use smaller subsets is cost. If it is excessively expensive or time-consuming to gather measurements, then, the fewer, the better. If an adequate subset of the original measurements can be found, then only this subset need be measured on all future objects to be classified. Another reason for reducing the dimensionality of the space in which classifications are made is simply to eliminate redundancy. There is no point in measuring a feature that does not add to the accuracy of the classification achieved without this feature. Furthermore, a lower misclassification rate can sometimes be achieved by using fewer features (Hand, 1981).

Basically, the feature selection problem is to find the best set of $d<D$ features from $\binom{D}{d} = \frac{D!}{d!(D-d)!}$ possible sets, evaluate each one with a selected criteria, and choose the one which results in the highest classification accuracy. In practice, however, this often not feasible because $\binom{D}{d}$ is very large and computationally excessive for sets of even moderate size, so heuristic techniques for choosing feature subset are required (Mucciardi and Gose, 1971). This section will present various feature selection techniques.

2.6.1. Branch-and-Bound

Feature selection via exhaustive search can become computationally prohibitive. However, it may be possible to determine the optimal feature set without explicit evaluation of all the possible combinations of d measurements with the help of the branch-and-bound algorithm. The algorithm is applicable under the assumption that a feature selection criterion satisfies the monotonicity property. Denoting by χ_j a candidate feature set containing j features, the monotonicity property implies that for nested feature set χ_j related as

$$\chi_1 \subset \chi_2 \subset \cdots \subset \chi_j \subset \cdots \subset \chi_D \tag{2.21}$$

the criterion function $J(\chi_j)$ satisfies

$$J(\chi_1) \leq J(\chi_2) \leq \cdots \leq J(\chi_D) \tag{2.22}$$

(Kittler, 1986)

To illustrate the basic idea of branch-and-bound algorithm, consider the problem of selecting two features out of five features. The tree in Figure 2.7 represents all the possible triplets of features, which include the ones that have to be discarded to obtain the optimal set of two features. Each node designates an eliminated feature.

Suppose we evaluate our feature selection criterion at every node of the tree in a top down manner starting with the right most branch. At each node we compare the criterion function value with that of the current best feature set, denoted J_o. If the value exceeds J_o, then there is still a chance that a better feature set will be discovered, and the search must therefore continue along the right most unexplored branch. If we reach the bottom of the tree and the corresponding criterion value is greater than J_o, then this node defines a new best feature set and J_o is updated accordingly.

If, on the other hand, the value of the criterion function at some node is less than J_o, then the branches originating from that node need not be explored, since by virtue of the monotonicity property the elimination of additional features will only result in a further decrease of the function value. The search will be particularly efficient if the features y_j for the successor nodes to each node of the tree are selected from left to right in the order of increasing magnitude of the criterion function (Kittler, 1986).

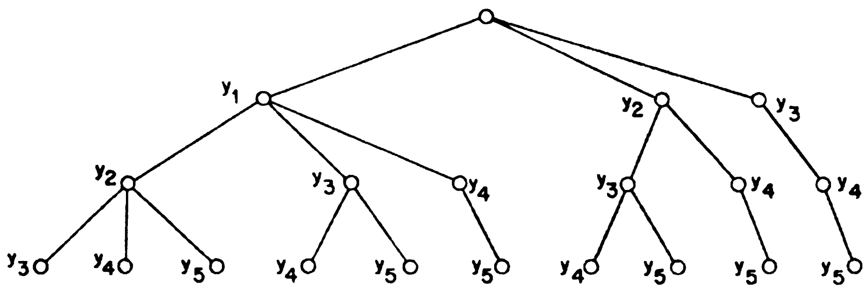

Figure 2.7. Tree representation of a branch-and-bound algorithm (Kittler, 1986)

2.6.2. Sequential Forward and Sequential Backward Selection

In many situations the determinations of the optimum feature set will not be computationally feasible even with the branch-and-bound algorithm. Another alternative is to seek a suboptimal solution. The simplest suboptimal procedures are the sequential forward and sequential backward selection algorithms.

Sequential forward selection (SFS) is a bottom-up process. Starting from an empty set, select the first feature as the individually best feature. At each subsequent stage the next feature is picked from the remaining available features so that in combination with features already selected, it yields the best value of the criterion function. Sequential backward selection (SBS) is a top-down process. Starting from the complete set of available features, eliminate one feature at a time. At each stage the feature selected for elimination is the one that results in the lowest decrease in the value of the criterion function.

The main source of the suboptimality of SFS is that it has no mechanism for removing from the feature set, the features that have become superfluous as a result of including other features. Similarly, once features have been discarded, SBS does not allow any revision of their merit. From the point of view of computational complexity, SFS is simpler than SBS since it requires that the criterion function be evaluated at most in d-dimensional spaces. In contrast, in SBS the criterion function must be computed in spaces of the dimensionality ranging from d to D. However, the advantage of the SBS is the ability to monitor continuously the amount of information loss incurred (Kittler, 1986).

2.6.3. Principal Component Analysis

Principal component analysis (PCA) is one of the most widely used multivariate techniques. The analysis consists of a linear transformation that produces new uncorrelated features (i.e. components) from the original features. One of its most popular uses is that of dimensionality reduction, since frequently just a few of these components are sufficient to represent adequately the original data.

Suppose that p features $X_1, X_2, \ldots, X_p$ have been observed on each of n individuals and that the observation vector for the ith individual is denoted by $X^{(i)} = (X_{i1}, X_{i2}, \ldots, X_{ip})'$.

PCA linearly transforms the features X_1, X_2, ..., X_p to new feature Y_1, Y_2,..., Y_p, the principal components, and hence the data observation $X^{(i)}$ to corresponding principal component scores $Y^{(i)} = (Y_{i1}, Y_{i2},..., Y_{ip})'$. Dimensionality reduction is affected if q ($<p$) of the components Y_i convey "most of the sample information" inherent in the p features X. In this case the original observations $X^{(i)}$ can be replaced by the first q elements of the corresponding principal scores. We can then write $Y^{(i)} = (Y_{i1},..., Y_{iq})'$. The major deficiency of this approach to dimensionality reduction is that, while the dimensionality of the space may indeed be reduced from p to q, all p original features are, in general, still needed in order to define the q new features Y_i (Krzanowski, 1987). This deficiency is also highlighted by McCabe (1984), who states: "In many applications, it is desirable not only to reduce the dimension of the space, but also to reduce the number of features which are to be considered or measured in the future". The use of PCA to discard redundant features has been outlined and criteria for choosing p features have been identified in Jolliffe (1972), McCabe (1984), and Krzanowski (1987).

2.6.4. Neural Network Weights

A number of heuristic measures have been proposed to estimate the relative importance or contribution of input features of neural networks to the output variable. Several saliency measures of input features explicitly consider both input and hidden weights and their interactions on the network output. An important saliency measure is proposed by Garson (1991) who partitions the hidden layer weights into components associated with each input node and then the percentage of all hidden nodes weights attributable to a particular input node is used to measure the importance of that input feature. Many researchers have studied Garson's measure and some modifications and extension have been made (Glorfield, 1996; Nath *et al.*, 1997; and Mak and Blanning, 1998).

Nath *et al.* (1997) experimentally evaluated the Garson's saliency measure and conclude that the measure works very well under a variety of conditions. Glorfield (1996) used a combination of backward elimination procedure and Garson's method to build models with different numbers of input features. An optimized backpropagation network is developed using the full set of available input features. The Garson methodology is then used to determine the input features' importance relative to the output. The feature that makes the smallest contribution to the output is then dropped. This procedure is repeated for the remaining set of features. This process continues until only a single input feature remains to develop the final backpropagation network model. At each step, the output objective function value is recorded. For a classification network, this value would correspond to the rate of correct classification (or error rate).

2.7. Empirical Studies

In this section, past studies in spectral reflectance and fluorescence related to fruits, especially apples, are reviewed.

2.7.1. Spectral Reflectance

Assessing fruit quality both for maturity and for defects using spectral reflectance dates back to the early 1940's. Lott (1943) used a spectrophotometer (General Electric

Automatic Recording Photoelectric Spectrophotometer) to measure reflectance of skin and flesh of several varieties of mature apples in 400 to 700 nm spectral ranges. Reflectance values in the 400 to 700 nm region are the most important for characterizing appearance, but information from a wider wavelength region is required for a full understanding of the optical properties of a sample. Reflectance measurement in a wider range, 250 to 2100 nm, has been conducted by Bittner and Norris (1968) for selected varieties of apples, peaches and pears. They used a Cary model 14R spectrophotometer with a multiplier-type phototube for the visible and ultraviolet region and a lead sulfide cell for the near-infrared (NIR) region. They suggested ratios of two wavelengths, 580/620 and 670/730, appears promising for indicating stage of maturation. Neither study, however, included measurement for defective fruit.

The earliest study on bruise detection on apple was conducted by Ingle and Hyde (1968). Bruised apple pulp consistently had a lower reflectance at 600 nm. Later, it was recognized that apple bruising ruptured cells releasing cell fluid filling the intercellular air spaces under the apple skin resulting in a reduction of the near-infrared reflectance from the apple surface (Brown *et al.*, 1974). They concluded the difference in reflectance for wavelengths around 800, 1200, and 1700 nm or a ratio of reflectance at some wavelength between 1400 and 2000 nm might be useful for bruise detection. It was further suggested that for processed apples, different wavelengths could be used to discriminate between apple defects, flesh, skin, stem or calyx ends. Further study of the mechanics of the trimming and orientation mechanisms was indicated to make sensing feasible (Reid, 1976). Some other spectrophotometric studies on apple bruise using reflectance measurement are Pen *et al.* (1985), Upchurch *et al.* (1990), and Upchurch *et al.* (1991).

These studies, along with the spectral curves presented, demonstrated the ability of light energy, especially in the NIR region, to distinguish differences in various tissues. Chemical bonds absorb light energy at specific wavelengths. Williams and Norris (1987) list some of the major absorption wavelengths for pigments, fats, proteins, carbohydrates and water. Within the visible wavelength range, the major absorbers are the pigments: chlorophylls, carotenoids, anthocyanins and other colored compounds. Water, carbohydrates, fats and proteins have absorption bands in the NIR region. This past research and related findings were primarily conducted utilizing spectrophotometer or spectral radiometer instrumentation. With such instrumentation, an object is measured as one value over a given surface. In other words, the instrument measures the integrated energy over a certain area with the size of the area defined by the detection set up. These studies demonstrate that various tissue, in fact, possess different spectral signatures when illuminated properly, which is potentially very valuable information for defect analysis and identification. However, past spectral radiometric work has some limitations in only being capable of providing spectral curves over a relatively large surface area instead of acquiring sufficient spatial information necessary for detailed defect inspection and quality sorting (Guyer and Yang, 2000).

Machine vision provides information about the spatial distribution of the intensity as well as the spectral content of the light. Coupling a camera with a computer enables machines to automatically perform visual-based inspection tasks. The various functions performed by a machine vision system include image capture, image processing, and pattern recognition (Abbott *et al.*, 1997). Machine vision systems have been used increasingly in the food and agricultural industry for inspection and evaluation purposes as they provide suitably rapid, economic, consistent and objective assessment (Brosnan and Sun, 2002).

The study of apples using machine vision has attracted much interest and can reflect the progress of machine vision technology for fruit inspection. Machine vision has been used for such tasks as shape classification, defects detection, and quality grading. Rehkugler and Throop (1986) developed an apple handling and sorting device using machine vision for bruise detection and classification into USDA grades with throughput of 30 apples per minute. A 64 pixels line scan camera with 750 nm highpass filter was used in the study to capture NIR images. Bruise patterns were determined by image filtering, differencing, binary image thresholding, and measurement of the shape of the areas representative of bruises by using thinness ratios. Later, they tried the same algorithm for detecting defects other than bruising such as scab, bird pecks, insect stings and hail damage and found out they have grey level NIR reflectance 10 levels below bruise tissue (Rehkugler and Throop, 1989). To increase the speed of image capturing Davenel *et al.* (1988) used a rectangular matrix camera instead of line scan camera for surface defect detection on apple. They used a 208x144 charged coupled device (CCD) camera equipped with a bandpass filter centered on 550 nm with 100 nm bandwidth. The best contrast between sound and damaged tissue is obtained at around this wavelength. Their system was able to analyze more than five fruit per second with a classification accuracy of 69% with selective thresholding within a zone image processing algorithm.

Various other techniques based on monochrome imaging have been explored for detecting blemishes and bruises on apple. These approaches include cooccurrence texture analysis (Throop *et al.*, 1995), structured lighting (Yang, 1993), and a flooding algorithm (Yang, 1994). The flooding algorithm can overcome the difficulties caused by the variation in light reflectance. It was found that this method of feature identification is applicable to other types of produce with uniform skin color. This technique was improved by Yang and Marchant (1996) who applied a 'snake' algorithm to closely surround the defects. Li *et al.* (2002) used fractal features as neural network inputs for identifying defects and stem-calyx area of Fuji apples from apple images captured at 840 nm. Crowe and Delwiche (1996a) and Crowe and Delwiche (1996b) developed a unique prototype of hardware for fruit handling and image acquisition. A combination of structured illumination (from laser line generated at 780 nm) and uniform diffuse illumination was used to illuminate fruit. Two cameras with 750 and 780 nm bandpass filters respectively were used to generate a composite image. A narrow band centered at 750 nm was used for detection of dark spots under diffuse illumination and a second band centered at 780 nm allowed concavity identification (stem/calyx) with structured illumination.

There are many studies in color imaging for detection of agricultural product quality. Heinemann *et al.*, (1995) used color imaging to discriminate russet in Golden Delicious apples using a global approach and mean hue on the apples. A discriminant function sorted the apple as accepted or rejected. The accuracy reached 82.5%, which is poor compared with European standards (Heinemann *et al.*, 1995). Other studies involving Golden Delicious apples were performed for the purpose of classification into yellow or green groups using HSI (hue, saturation, intensity) color system method (Tao *et al.*, 1995). The results show that an accuracy of over 90% was achieved for the 120 samples tested. To segment defects, Leemans *et al.*, (1998) used Mahalanobis distance between each pixel of an apple color image and a global model of healthy apples. The algorithm gave satisfactory results to detect various defects such as bruises, russet, scab, fungi, and wounds. Another method of defect segmentation from color images is based on a Bayesian classification process (Leemans *et al.*, 1999). Nakano (1997) used two neural network models for pixel-based color grading of apples and whole apple grading. Steinmetz *et al.*, (1999) investigated sensor fusion for the purpose of sugar content prediction in apples by combining image analysis and a near-infrared spectrophotometric sensor.

Multispectral imaging provides spectral information at two or more wavelengths in addition to spatial information. Color imaging is a special case of multispectral imaging, which uses broad bandwidth signals (Abbott *et al.*, 1997). Multispectral imaging is not limited to color; multiple images can be captured at different wavelengths in the visible and near-infrared regions. Generally, an interference filter on the lens of the camera allows an image to be acquired at a specific wavelength (narrow band); however, a filter wheel or multiple cameras are required when more than one wavelength is specified. More advance multispectral imaging systems use acoustical optical tunable filters (AOTF) and liquid crystal tunable filters (LCTF).

Aneshansley *et al.* (1997) gathered visible and NIR reflectance images for a large number of defects found in five varieties of apples, i.e. Red Delicious, Golden Delicious, Crispin, McIntosh, and Empire. There were eighteen defects reported. Some of the apple defects found were bitter pit, blister spot, codling moth, flyspeck, leaf roller, rot, russet, scab, scald, and sunburn. They used two camera/lens/tunable filter combinations. The first one is to capture visible images ranging from 460 to 750 nm, the second one is to capture NIR images ranging from 750 to 1030nm. They concluded there are 4 wavelengths, 540, 750, 970, and 1030 nm, for specific groups of defects that give the greatest contrast, measured by Mahalanobis distance, between damage and undamaged tissue.

A similar study by Miller *et al.* (1998) used the same imaging device as Aneshansley *et al.*, (1997) was conducted to analyze 8 varieties of apples from two fall harvest seasons, i.e. Empire, Gala, Golden Delicious, Granny Smith, Red Delicious, Rome, Red Stayman, and York. Pattern recognition models based on back propagation neural network, nearest cluster, K-nearest neighbor, and unimodal Gaussian were compared. Overall, the back propagation neural network models provided the highest correct classification rate ranging from 83 to 85% for 1996 data and from 94 to 96% for 1995 data. They concluded the most significant wavelengths were in the 690-750 nm range and 530 nm when considering data from both seasons.

Wen and Tao (2000) proposed a dual camera system to solve a persistent problem in the discrimination between true defects and the stem-end/calyx of fruit. A near-infrared (NIR) camera and a mid-infrared (MIR) camera were used simultaneously to capture apple images. The NIR camera at 700 to 1000 nm is sensitive to both stem-end/calyx and true defects; whereas the MIR camera at 3400 to 5000 nm or 8000 to 12000 nm is only sensitive to the stem-end/calyx. True defects can be quickly and reliably extracted by logical comparison between the processed NIR and MIR images. A

98.86% recognition rate for stem-ends and a 99.34% recognition rate for calyxes were achieved using this system.

Another method to capture multispectral images is using a monochrometer as the illumination source. Guyer and Yang (2000) used a combination of an enhanced NIR black and white camera with sensing range of 400-2000 nm and a monochrometer controlled light source to detect defects on cherries. Spectral images were collected over the 680 – 1280 nm range at increments of 40 nm. Genetic artificial neural networks were applied to pixel-based classification. An average of 73% classification accuracy was achieved for correct identification as well as quantification of all types of cherry defects. Kavdir and Guyer (2002) acquired apple images using the same imaging configuration. They used the image-based classification instead of pixel-based for the classification using neural networks. Classification accuracy of 89.2 to 100% was achieved in the 2-class model to separate defective apples and non-defective apples without confusing the stem-end/calyx with defects.

The Instrumentation and Sensing Laboratory, USDA at Beltsville, Maryland, has developed a laboratory-based hyperspectral imaging system for food safety and quality research (Kim *et al.*, 2001a). The system is capable of reflectance and fluorescence measurements in the 430 to 930 nm region with 1 mm spatial resolution. The system uses a line-by-line scanning technique to acquire hyperspectral images. Mehl *et al.* (2002) used the hyperspectral imaging system to acquire hyperspectral images of three apple cultivars. A principal component analysis of the hyperspectral image of normal and abnormal apples (with defects including bruises, diseases, and soil contaminations) was performed to help in choosing the best three potential wavelengths to be used in a multispectral imaging system with a three-channel common aperture camera for discriminating all the defects. The three selected bands are 705±40, 575±20, and 460±20 nm. In their study, good separation between normal and defective apples is obtained for Gala (95%) and Golden Delicious (85%), however, separation is limited for Red Delicious (76%). The laboratory-based hyperspectral imaging system has also been used for study on fecal contamination on apples in reflectance mode (Kim *et al.*, 2002a) and fluorescence mode (Kim *et al.*, 2002b). An imaging spectrograph combined with an InGaAs area array camera used by Lu (2003) to acquire hyperspectral images on apples in the extended NIR region of 900-1700 nm that has not been much explored before for bruise detection. A combination of principal component analysis and noise fraction transforms was used to detect both new and old bruises resulting in a correct detection rates up to 88% for Red Delicious and up to 94% for Golden Delicious. The study found that the 1000-1340 nm region was the most appropriate for bruise detection.

2.7.2. Fluorescence

The response of plants to a diverse range of environmental, chemical, and biological stresses has been assessed by changes in chlorophyll fluorescence. However, application of chlorophyll fluorescence techniques to the field of fruit postharvest physiology has been made only recently, even though the kinetics and fluorescence emission spectra of several fruits are similar to those of green leaves (DeEll *et al.*, 1999).

Application of chlorophyll fluorescence as a rapid nondestructive technique to detect low-O_2 or high-CO_2 stress in apples during storage has been evaluated by DeEll *et al.* (1995). Chlorophyll fluorescence was determined using a fluorometer. Apple fruit stored in 1% to 1.5% O_2 or 11% to 12% CO_2 for five days caused variable fluorescence (Fv) to decrease compared to those held in standard atmospheres, and suggested that chlorophyll fluorescence techniques can detect low-O_2 and high-CO_2 stress in apples before the development of associated disorders. Another application of chlorophyll fluorescence in apple measured by a fluorometer is as an indicator of freezing injury (Forney *et al.*, 2000). The reductions on chlorophyll fluorescence were associated with freezing damage in treated Northern Spy apples held at –8.5°C for 24 hours. Chlorophyll fluorescence also decreases in heat-treated apples thus it is useful for indicator of heat injury in apples (Song *et al.*, 2001).

Most of the study of chlorophyll fluorescence imaging is evaluation of fluorescence from leaves. One of the earliest applications of plant fluorescence imaging was reported by Omasa *et al.*, (1987). They captured chlorophyll fluorescence patterns with a single-band imaging system. Meyer and Gentry (1998) also reported the use of chlorophyll fluorescence imaging system for photochemical yield of photosystem II (PSII) of *Rosa rubiginosa* leaflets. Multispectral laser-induced fluorescence (LIF) imaging systems were reported by several investigators (Lang *et al.*, 1996; Lichtenthaler *et al.*, 1996). They used pulse lasers as the excitation source where the laser beam was expanded (~20-cm-diameter area) to illuminate the entire surface of leaf samples for imaging applications. Kim *et al.* (2001b) used a stable nonpulsed light as the excitation source for their multispectral fluorescence imaging system applied to plant leaves. The system captures fluorescence images at four spectral bands using interference filters attached to a filter wheel in the blue, green, red and far-red regions of the spectrum centered at 450, 550, 680, and 740 nm respectively. A UV lamp with a 400 nm low pass filter was used as the excitation source.

Application of chlorophyll fluorescence imaging for fruit quality evaluation has not been fully explored. A study by Nedbal *et al.* (2000) used chlorophyll fluorescence imaging to predict lemon quality. The technique is able to distinguish between mold-infected areas that will eventually spread over the surface of the fruit, and damaged areas that do not increase in size during lemon ripening. A laboratory-based hyperspectral reflectance and fluorescence imaging system has been used to explore the characteristic of fluorescence images of defective apples (Kim *et al.*, 2001a). Fluorescence images at 530 nm show fungal contamination (sooty blotch) and bruised spots on apples with greater contrast than the reflectance images. Furthermore, they used the imaging system to detect fecal contamination on Red Delicious, Fuji, Golden Delicious and Gala apples (Kim *et al.*, 2002b). Their result indicates that the multispectral fluorescence technique can be used to effectively detect fecal contamination on apple surfaces. They identified four optimal bands (450, 530, 685, and 735 nm) for discrimination of contaminated apple surface. Codrea *et al.* (2002) used a chlorophyll fluorescence imaging system for apple classification with blue actinic light as an excitation source and a red filter to capture fluorescence images at the red region.

3. MATERIALS AND METHODS

3.1. Multispectral Imaging System

A multispectral imaging system (Figure 3.1) was designed and built to capture images of apples under reflectance and fluorescence modes. One important consideration in the design of the imaging system was to be able to capture apple images at different wavelengths (multispectral) and under different lighting modes without moving the apple.

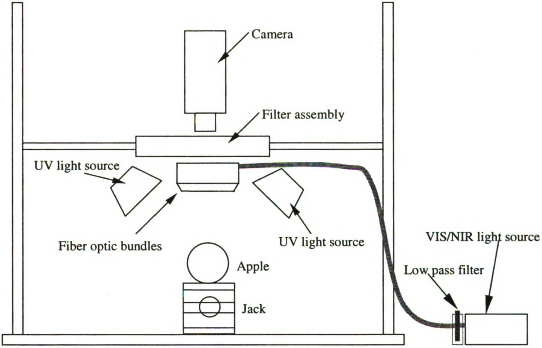

Figure 3.1. Schematic diagram of the multispectral imaging system

The main components of the multispectral imaging system were:

(1) Monochrome CCD camera

Pulnix TM-9701 (Pulnix America Inc., Sunnyvale, California) was used as an image sensor. The camera spatial resolution was 640 x 480 with 8-bit grayscale. Two different lenses were mounted to the CCD camera head: a 16 mm lens with maximum aperture 1.4 and a close up lens #4. The combination of the lenses allowed a captured whole apple image to fill the frame at a distance of 220 mm. The camera integration was enabled through a microcontroller to allow control of exposure time. Extended exposure time (around 5000 ms) was needed for fluorescence measurement due to the low fluorescence energy emission.

(2) Filters

Seven bandpass filters (450, 550, 680, 740, 880, 905, and 940 nm peak transmittance) and a 710 nm high pass filter were used in capturing images as a means to create multispectral data. Bandpass filters at 450, 550, and 680 nm are associated with blue, green and red color respectively. Additionally, past study on plant leaf fluorescence indicates leaves exhibit fluorescence emission with a maximum at 450 nm and a shoulder peak at 530 nm as well as narrower emission at 680 and 740 nm (Kim *et al.*, 2001b). The bandpass filters 880, 905, and 940 were selected to capture NIR images. These wavelengths may relate to starch, cellulose, and water respectively (Williams and Norris, 1987).

All bandpass filters used in this research had 10 nm FWHM (full width half maximum) properties. The filter transmittance characteristic (measured by FieldSpec FR spectroradiometer, Analytical Spectra Device Inc., Boulder, Colorado) along with camera sensitivity provided by the manufacturer is shown in Figure 3.2.

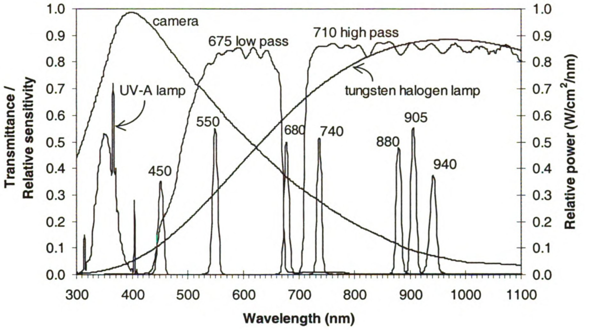

Figure 3.2. Spectral characteristics of the camera, filters, and light sources

The filter assembly made of a filter wheel (model AB300, CVI Laser Corp., Albuquerque, New Mexico) stacked with a lab-made sliding filter frame was used to hold the filters and was positioned underneath the camera lenses. The filter wheel held up to 5 circular filters and the sliding filter frame was also manufactured to hold up to 5 circular filters. The filters placed in the filter wheel were the 450, 550, 680 and 740 bandpass filters; the remaining one empty slot in the filter wheel was used to allow the light to pass to the other filters placed in the sliding filter frame (880, 905, 940 nm bandpass filters and 710 nm highpass filter). The sliding filter frame also had one empty slot, which could be used in combination with one empty slot from the filter wheel to capture images in broad range (without any filter). An AB300 filter wheel controller and stepper motor with microcontroller were used to control the movement of the filter wheel and sliding filter frame, respectively.

(3) Light sources

Two different light sources were used independently to provide illumination for fluorescence and reflectance measurement. Two UV-A fluorescent lamp assemblies (model XX-15A 365 nm, Spectronics Corp., Westbury, New York) were used for UV-induced fluorescence measurements. The fluorescent lamp assemblies were arranged at 45° to the top surface of the apple and positioned under the filter wheel at the front and rear of the imaging system enclosure. Each fluorescent lamp assembly contained two fluorescent light bulbs coated with UG1 filter material to prevent transmittance of radiations greater than approximately 400 nm, thus providing radiation below 400 nm as the excitation source. The other light source was a tungsten halogen light source powered by a regulated DC power supply (Fiber-Lite A-240P, Dolan-Jenner Industries, Inc., Lawrence, Massachusetts) for visible-light-induced fluorescence and visible and NIR (VNIR) reflectance measurements. The spectrum of UV-A lamp and tungsten halogen lamp is shown in Figure 3.2. Light from a 150 W tungsten halogen bulb was transmitted through two randomly arranged rectilinear fiber bundles. These line lights were positioned under the filter wheel on the left and right side of the imaging enclosure at 45° to the top surface of the apple. To prevent specular reflectance and provide uniform illumination, a hollow-truncated-cone-shaped diffuser was used to cover the apple during image acquisition under this light source. The diffuser was made of two layers of material, transparent plastic sheet in the inner surface and white copier paper in the outer surface. The dimension of the truncated-cone diffuser was 140, 55, and 180 mm for base diameter, top diameter, and height, respectively. The tungsten halogen light source was set to remote mode to allow adjustment of light intensity by an external microcontroller through a 8-bit data line, thus an integer value between 0 to 255 was used as the digital light level value. The relationship between digital light level value and actual light intensity measured by an illuminometer measured at the apple surface point/location (Model 93-1065, Greenlee Textron Inc., Rockford, Illinois) is shown in Figure 3.3. For visible-light-induced fluorescence measurements only, a 675 nm low pass filter was placed in a slot positioned between the tungsten halogen light source and the fiber optic to prevent light transmittance greater than 675 nm (Figure 3.1), thus, providing radiation below 675 nm as the excitation source. A stepper motor was used to slide the low pass filter in or out the slot.

A micro controller (model BasicX-24, Net Media Inc., Tucson, Arizona) along with custom made software in Microsoft Windows environment were used to automate the image acquisition process including control of camera's exposure time, filter wheel movement, lighting, and communication with the imaging software QuantIm (Zedec, Inc., Morrisville, North Carolina).

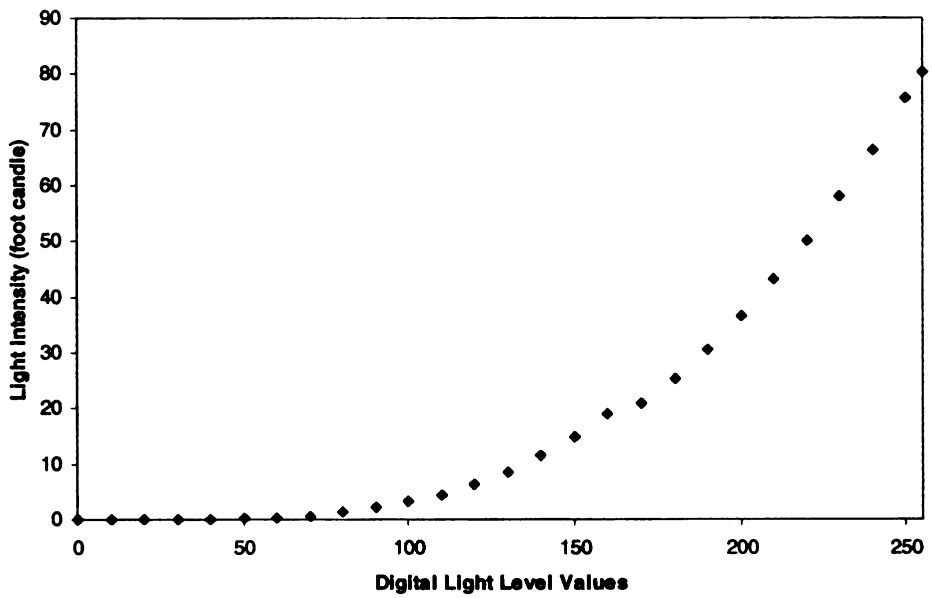

Figure 3.3. Relation between digital light level value and light intensity of tungsten halogen light model A-240P Dolan-Jenner Industries, Inc. (measured at 160 mm distance)

3.2. Apples

Honeycrisp, Redcort (a strain of Cortland), and Red Delicious varieties were used for the experiments. The apples were harvested from Michigan State University experimental orchards in Clarksville (Clarksville Horticultural Experiment Station) in September-October 2002, and were kept in cold storage at 0°C or 3°C for 4 months. These temperatures were selected, as they were likely to induce certain disorders. The selection of apple variety was based on the known occurrence of disorders in these varieties after storage. Bitter pit, soft scald, black rot, and decay were found on Honeycrisp apples, and superficial scald was found on Redcort and Red Delicious apples. The number of apples for multispectral image acquisition was 91, 83, and 19 of

Honeycrisp, Red Delicious, and Redcort, respectively. Apples were held at room temperature for 2 hours before image acquisition.

3.3. Image Acquisition

Three imaging modes were used in data acquisition:

(1) Visible and NIR (VNIR) reflectance using tungsten-halogen light (referred to as R),

(2) Visible light induced fluorescence using a tungsten-halogen light filtered by a 675 nm low pass filter (referred to as FVIS),

(3) UV induced fluorescence using UV-A fluorescent lamps with a built-in 400 nm UG1 low pass filter (referred to as FUV).

The three modes of imaging used different filter sets. Even though there were 3 imaging modes and 8 filters available, a preliminary study showed that not all the imaging mode and filter combinations provided acceptable response based on reflectance and fluorescence captured by the camera. Table 3.1 shows images captured for each imaging mode. A total of 18 images per apple were captured with these three modes and filter combinations. A different camera exposure time was used for each of the 18 images captured to take advantage of the full 8-bit dynamic range, therefore, avoiding under exposed or over exposed images. The lowest acceptable camera exposure time was 50 ms, beyond that the camera produced images with inconsistent brightness/exposure. This limitation, therefore, forced the use of different light levels for each filter in reflectance mode. Exposure time ranged from 50 to 5000 ms in fluorescence mode, and 50 to 400 ms in reflectance mode (Table 3.2.).

Table 3.1. Acquired image for each imaging mode and filter combinations (indicated by √)

Filters[1]	VNIR Reflectance	VIS-induced fluorescence	UV-induced fluorescence
450	√		√
550	√		√
680	√	√	√
740	√	√	√
880	√		
905	√		√
940	√		
710	√	√	√
NF	√		

[1] Numbers indicate peak wavelength (nm) of bandpass filters except 710 is cut-off wavelength (nm) of the highpass filter; NF=no filter.

Table 3.2. Lighting level and exposure time for each imaging mode and filter combinations

Imaging Mode	Filters[1]	Lighting Level	Exposure Time (ms)
VNIR reflectance (R)	450	255	400
	550	150	200
	680	150	100
	740	120	100
	880	255	100
	905	255	200
	940	255	300
	710	50	100
	NF	50	50
VIS-induced fluorescence (FVIS)	680	255	800
	740	255	5000
	710	255	500
UV-induced fluorescence (FUV)	450	-	2000
	550	-	5000
	680	-	1500
	740	-	1500
	905	-	5000
	710	-	50

[1] Numbers indicate peak wavelength (nm) of bandpass filters except 710 is cut-off wavelength (nm) of the highpass filter; NF=no filter.

Images were collected in a dark room with only the light source, coming through either two optic fibers to a line light illuminator from the tungsten-halogen source or from the UV-A fluorescent lamps, cast on the apple. Dark images were collected prior to the measurements. Presentation of apples to the camera was done by hand randomly with the location of defect on the apple facing the camera. Once an apple was positioned in its desired orientation on a black matte background, all eighteen images were acquired without moving the apple. After finishing an image acquisition session, color digital images of the same orientation of apples were captured using a digital color camera. These images were used as a tool to guide selection of the defective area pixels.

The distance between the camera and the surface of the apples being imaged was about 220 mm. Resolution of the original images was 640 x 480 pixels in 8-bit grayscale tagged image file (TIF) format.

3.4. Image Processing

Original images were cropped to 480 x 480 pixels to reduce the image size by discarding background pixels on the left and right. Dark images and reference images from a white reference panel (Model Spectralon, Labsphere, Inc., Sutton, New Hampshire), obtained in reflectance mode using the same light level and camera's exposure time as each corresponding sample image, were used for reflectance image corrections. The following equations were used to create corrected reflectance images:

$$IC_\lambda = \frac{IS_\lambda - ID_\lambda}{IR_\lambda - ID_\lambda} \tag{3.1}$$

where IC is corrected image; IS is sample image; ID is dark image; and IR = reference image.

Since the nature of fluorescence is different than reflectance, fluorescence image correction employed the following equation:

$$IC_{\lambda} = (IS_{\lambda} - ID_{\lambda}) \times \left(\frac{CE_{\lambda}}{CC_{\lambda} \times CF_{\lambda}} \right) \tag{3.2}$$

where IC is corrected image; IS is sample image; ID is dark image; CC is camera sensitivity factor; CF is filter factor; and CE is exposure time factor. The lens characteristic factor was assumed to have flat absorption spectral over the visible and NIR range, therefore, it is not included in equation 3.2.

Filter factors and camera sensitivity factors were extracted from normalized values of the camera sensitivity and filter characteristic chart shown in Figure 3.2. Filter factors were obtained from the peak values at the corresponding band pass filter and the camera sensitivity factors were obtained from the camera sensitivity curve at the particular wavelength. Since the fluorescence response was very low, exposure time needed to be set longer in fluorescence mode than in reflectance mode without sacrificing image quality due to noise. Exposure time of 5000 ms was the maximum value that still yielded good image quality and was used as a basis for fluorescence image correction. Therefore, CE was calculated as 5000 divided by actual exposure time for a particular band pass filter.

Using MATLAB (The Math Works Inc., Natick, Massachusetts), each set of eighteen corrected images from an apple sample was then put together into one multi-image TIF file to be more manageable for further analysis.

3.5. Pixel Sampling

Pixel gray values from the multispectral reflectance and fluorescence images were the only features for classification. A graphical user interface program written in MATLAB was developed for interactive sampling of pixels from apple images to create a data set of multispectral pixel gray values. The program allowed viewing four apple images simultaneously from different imaging mode and filter combinations to better guide in pixel selection. Pixels were randomly selected but represented various defective and normal tissues. The total number of sampled pixels was 1320, selected from the three apple varieties (Table 3.3).

Table 3.3. Total number of pixels selected for each tissue type from images of Honeycrisp, Redcort, and Red Delicious

Variety	Tissue type	Number of selected pixel
Honeycrisp (91 apples)	Normal	395
	Bitter Pit	125
	Black Rot	125
	Decay	125
	Soft Scald	130
	Total Honeycrisp	900
Redcort (83 apples)	Normal	125
	Superficial Scald	125
	Total Redcort	250
Red Delicious (19 apples)	Normal	95
	Superficial Scald	75
	Total Red Delicious	170
	Total Selected Pixels	1320

Once a pixel was selected from an image, the program captured 18 values at the same coordinate from the corresponding 18 images in the image set and assigned a label specifying the kind of defective tissue the pixel represented. Verification of defect types on the apples was confirmed by experts from Department of Horticulture, Michigan State

University. These values served as the tissue spectral signature and as the 18 inputs to the classifier.

3.6. Classification

In this study, classification was applied to the sampled pixels. Since pixels are the building blocks of an image, pixel-based classification could be extended to image-based classification to classify the apple. Figures 3.4 illustrates the concept of pixel classification.

Four different classifiers were used for classifying pixels into different disorder classes, i.e. backpropagation neural network, nearest neighbor, linear discriminant function, and quadratic discriminant function. The first two are non-parametric and the last two are parametric classifiers.

Two schemes of classification, 2-class and multiple-class were developed and evaluated. Apple tissues were categorized into normal tissues or disorder tissues in the 2-class scheme, with bitter pit, black rot, decay, soft scald and superficial scald pixels grouped into a single disorder tissue class. For the multiple-class scheme, each sampled pixel was labeled as one of six different types of tissues, i.e. normal, bitter pit, black rot, decay, soft scald and superficial scald.

All 18 multispectral pixel gray values (referred to as the full model) were used as input features to the classifiers. The reduced models used subsets of the 18 features. Feature selection methodologies were used to find optimal subsets and are discussed separately in section 3.7.

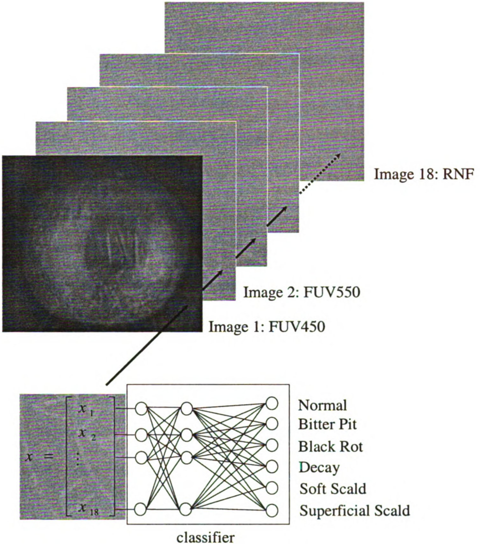

Figure 3.4. Pixel classification from multispectral images

Classification of pixels was evaluated for three varieties of apples, i.e. Honeycrisp, Redcort and Red Delicious. "Combined variety" was also evaluated by unifying the three data sets, to evaluate the performance of the classifier over the large variation of data.

A K-fold cross validation technique was used to assess the performance of the classifiers. In this study, K equal to 10 was chosen. This value is recommended and sufficiently accurate for practical purposes (Glorfield, 1996). The basic K-fold methodology is as follows. Data is split randomly into K groups of approximately equal size. The first of the K groups is held out for model testing while the actual model is trained using the remaining K-1 groups. The classifier is developed using the combined K-1 group sample and its performance is assessed with the held-out group sample. The second group is then removed from the K-1 group sample and the first group is included in this sample. Again, the model is developed with K-1 group samples and its performance is determined using the held-out second group. This process is repeated K times. The total performance is the average from each held-out group. For the neural network classifier, in addition to one held-out group for testing, three held-out groups were used as validation sets for the early stopping method. Thus, the remaining K-4 groups were used for training.

Performance of the classifiers was evaluated by calculating the classification accuracy for each class and the total accuracy from a confusion matrix. The confusion matrix is an n x n contingency table of actual group to classified group. For the 2-class scheme, the accuracy for normal tissues was calculated as the percentage of normal tissue pixels classified into normal tissue. Similar calculation was applied to the accuracy for disorder, i.e. the percentage of disorder tissue pixels classified into disorder tissue. The total accuracy was calculated as the percentage of total correctly classified pixels. Similar calculation was applied to the multiple-class scheme for each disorder class.

3.6.1. Classification Using Artificial Neural Network

An Artificial Neural Network (ANN) with feed forward multilayer topology and backpropagation learning was used as the classifier. A MATLAB code using Neural Network toolbox was used for the classification. The number of input nodes was 18 for the full model; each was connected to the multispectral pixel gray values. The number of neurons in the output layer was two for the 2-class scheme and six for the multiple-class scheme. One hidden layer was the most efficient configuration with 20 neurons on the layer based on trial and error. Using two or more hidden layers was avoided, as it would increase the training time. A log-Sigmoid transfer function was used in each layer of neurons. The function generates outputs between 0 and 1 as the neuron's net input goes from negative to positive infinity.

Before training, the weights and biases were randomly initialized. Early stopping method was used, by splitting sampled pixel data into three subsets, to improve generalization of the ANN classifier. The first subset was the training set, which was used for computing the gradient and updating the network weights and biases. The second subset was the validation set. The error on the validation set was monitored during the training process. The validation error will normally decrease during the initial phase of training, as does the training set error. However, when the network begins to overfit the data, the error on the validation set will typically begin to rise. When the validation error increases for a specified number of iterations, the training is stopped, and the weights and biases at the minimum of the validation error were returned. The third subset was the test set. It was used to test the performance of the neural network classifier when it is exposed to the new data set.

A typical method of assessing the performance of a neural network is to run a number of simulations, each beginning from a different starting point in weight space. Ten simulations for each one held-out testing group were performed and the results were averaged.

3.6.2. Classification Using Discriminant Functions

The theoretical background of the Bayes rule as a basis for discriminant functions was explained in detail in section 2.5.2. Data was assumed to have multivariate Gaussian distribution given in Equation 2.11. Prior probabilities of $P(\omega_i)$ in Equation 2.10, where i=1,2 for the 2-class scheme and i=1,..,5 for the multiple class scheme, were assumed to be equal for each class. Unknown parameters of μ and Σ, which are the mean and covariance matrix for each class, were estimated from the training data set using Equations 2.12 and 2.13.

All the calculation of the parameters and discriminant functions for each class was performed by DISCRIM procedure in SAS (SAS Institute Inc., Cary, North Carolina) statistical software with METHOD options set to NORMAL. Two types of discriminant functions were calculated: a linear discriminant function (the within-class covariance matrices are assumed to be equal) and a quadratic discriminant function (the within-class covariance matrices are assumed to be unequal).

3.6.3. Classification Using K-Nearest Neighbor

Detailed information on the K-Nearest Neighbor (KNN) classifier is given in section 2.5.3. Since this classifier is a nonparametric approach, no assumptions of the data distribution were made. The only parameter that had to be chosen was the value of K, which was the number of the neighbor members included in the distance measurements. K equal to one was the best value based on trial and error. Procedure DISCRIM from SAS was used to perform all the calculations with METHOD options set to NPAR.

3.7. Feature Selection

The full model of this system utilized 18 images (each image refer to as a feature) from a combination of lightings and filters to be captured for each apple; thus the model would not be feasible for practical implementation of an automatic sorting technique that requires fast image acquisition and processing. Furthermore, problems can occur when developing multivariate models and the best sets of input to use are not known. This is particularly true when using a neural network. Unrequired inputs can significantly increase learning complexity. Input feature selection is aimed to determine which input features are required for a model. Problems that can occur due to poor selection of inputs according to Back and Trappenberg, (2001): 1) as the input dimensionality increases, the computational complexity and memory requirements of the model increase, 2) learning is more difficult with unrequired inputs, 3) misconvergence and poor model accuracy may result from additional unrequired inputs, and 4) understanding a complex model is more difficult than simple models which give comparable results.

Three approaches were used in feature selection. The first approach was grouping features (images) by imaging mode(s). The second approach was grouping features by individual filters, and the third approach was individually considering each of the 18 features. A complete search method, meaning evaluating the performance of all possible combinations, was used in the first two approaches to find best combinations of grouped features. In the latter approach, various search methods including complete search, backward elimination, principal component analysis, and neural network weights were used to find best feature subsets from the 18 features.

3.7.1. Imaging Mode Combinations

There were 7 possible combinations of imaging modes to incorporate in the classification models, i.e. three single-imaging modes (FUV, FVIS, and R), three dual-imaging modes (FUV+FVIS, FUV+R, and FVIS+R) and one triple-imaging mode (FUV+FVIS+R). Any classification model involved all images in the imaging mode(s) that appeared in a combination, noting that each imaging mode contains different numbers of features or filters (Table 3.1). The number of features (images) acquired for FUV, FVIS, and R was 6, 3, and 9 respectively. Features included in each imaging mode combination are shown in Table 3.4.

Table 3.4. Features included in imaging mode combinations (indicated by √)

Imaging Mode Combination[1]	Feature[2]																	
	FUV450	FUV550	FUV680	FUV740	FUV905	FUV710	FVIS680	FVIS740	FVIS710	R450	R550	R680	R740	R880	R905	R940	R710	RNF
FUV	√	√	√	√	√	√												
FVIS							√	√	√									
R										√	√	√	√	√	√	√	√	√
FUV+FVIS	√	√	√	√	√	√	√	√	√									
FUV+R	√	√	√	√	√	√				√	√	√	√	√	√	√	√	√
FVIS+R							√	√	√	√	√	√	√	√	√	√	√	√
FUV+FVIS+R	√	√	√	√	√	√	√	√	√	√	√	√	√	√	√	√	√	√

[1] FUV=UV-induced fluorescence, FVIS=visible-light-induced fluorescence, R=reflectance

[2] Prefixes referred to in [1]; Numbers followed after FUV, FVIS, or R indicate peak wavelength (nm) of bandpass filter except 710 is cut-off wavelength (nm) of the highpass filter, and NF=no filter

3.7.2. Filter Combinations

Two different approaches were used in filter combinations. In the first approach, feature groups were based on filters. The number of features for each filter was different depending on whether a particular imaging mode captured an image at the selected filter. The number varies from 1 to 3. There were 9 filters (including NF) used in the experiment. The classification models were built based on combinations of filters from 1 to 9 filters. Any classification model involved all images related to the filter that appeared in a combination. An example of features included in the model for the 1-filter models is shown in Table 3.5. The purpose of this approach is to find the best filter combination if multiple-imaging modes are involved in the model.

In the second approach, filter combinations involved only features within a given imaging mode. Only FUV and R modes were used using the second approach, because preliminary study showed classification accuracy for FVIS was low. The purpose of this approach is to find the best filter combination if a single imaging mode is used in the model.

Table 3.5. Feature included in 1-filter model (indicated by √)

Filter[1]	Feature[2]																	
	FUV450	FUV550	FUV680	FUV740	FUV905	FUV710	FVIS680	FVIS740	FVIS710	R450	R550	R680	R740	R880	R905	R940	R710	RNF
450	√									√								
550		√									√							
680			√				√					√						
740				√				√					√					
880														√				
905					√										√			
940																√		
710						√			√								√	
NF																		√

[1] Numbers indicate peak wavelength (nm) of bandpass filters except 710 is cut-off wavelength (nm) of the highpass filter; NF=no filter.
[2] Prefixes FUV=UV-induced fluorescence, FVIS=visible-light-induced fluorescence, R=reflectance; Numbers followed prefixes referred to in [1].

The optimum number of filters was determined by selecting a combination with the least number of filters that statistically is not different from the full model.

3.7.3. Feature Combinations

The total number of combinations from a 1-feature model through an 18-feature model is 262,143 combinations, which is computationally very exhaustive if we want to find the best subsets by searching through all the combinations. Several search methods were used to find best subsets by avoiding an exhaustive search.

3.7.3.1. Complete Search

A feature selection method using a complete search is guaranteed to find the optimal subset of features among the available features. However, as the number of features increased, the number of combinations to be evaluated could become computationally exhaustive. Up to four-feature combinations were evaluated in this study using the complete search. The number of combinations for 1, 2, 3, and 4-features from the full set of 18 features is 18, 153, 816, and 3060 combinations.

3.7.3.2. Backward Elimination

Backward elimination started from the full model (involving 18 images). In each step, one feature (image) was eliminated from the model until the model contained only one feature. The feature to be eliminated in each step was selected based on the evaluation of the total accuracy in the test data set. The feature being least detrimental to the total accuracy when it was eliminated from the model was selected from elimination in that step.

The optimum model was determined by selecting the simplest model, the model with least features, which statistically was not different from the full model.

3.7.3.3. Principal Component Analysis

Two methods described by Jolliffe (1972) were used for feature selection. Principal component analysis was performed on all original K features (K=18 in this study), and the eigenvectors (principal components) along with their eigenvalues were inspected. In the first method, referred to as Method B2, if p features are to be retained, the K-p principal components, which had smallest eigenvalues, are selected, starting with the component corresponding to the smallest eigenvalues, then to the second smallest eigenvalues and so forth. One feature associated with the highest eigenvector coefficient (i.e. the highest loading) is then discarded from each of the K-p components. Method B4 retains features by starting with the first p components with highest eigenvalues and keeping the feature with the highest loading from each selected component.

The optimum model was determined by selecting the simplest model, the model with least features, which statistically was not different from the full model.

3.7.3.4. Neural Network Weights

Neural network models with the full set of available inputs (18 inputs) were trained using 10-fold cross validation described in section 3.6. A model yielding maximum total accuracy was selected for further analysis of its connection weights for feature selection purposes. The Garson methodology (Garson, 1991) was used to determine the input features' importance relative to the output using equation 3.3.

$$VI_{X_p} = \frac{\sum_{j=1}^{n_H}\left[\frac{|I|_{P_j}}{\sum_{k=1}^{n_p}|I|_{P_{j,k}}}|O|_j\right]}{\sum_{i=1}^{n_p}\left[\sum_{j=1}^{n_p}\left(\frac{|I|_{P_{i,j}}}{\sum_{k=1}^{n_p}|I|_{P_{i,j,k}}}|O|_j\right)\right]} \tag{3.3}$$

Where VI_{Xp} is the feature importance measure for the P^{th} input feature, n_p is the number of input feature, n_H the number of hidden layer processing elements, $|I|_{Pj}$ is the absolute value of the hidden layer weight corresponding to the P^{th} input feature and j^{th} hidden layer processing element, and $|O|_j$ is the absolute value of the output layer weight corresponding to the j^{th} hidden layer processing element.

The feature that makes the smallest contribution to the output was then dropped. This procedure was repeated for the remaining set of features. This process continues until only a single input feature remains to develop the final neural network model. At each step the output objective function value was recorded, in this case, the classification accuracy.

The optimum model was determined by selecting the simplest model, the model with least features, which statistically was not different from the full model.

4. RESULTS AND DISCUSSION

4.1. Captured Images

Example images of how various types of apple defects appeared under different filters and three imaging modes, reflectance (R), visible light induced fluorescence (FVIS), and UV induced fluorescence (FUV) are shown in Figure 4.1. Fluorescence images from FVIS at 880, 905, and 940 nm and also fluorescence images from FUV at 880 and 940 nm were not acquired because the camera was not sensitive enough to capture low fluorescence emission at these wavelengths.

Under reflectance mode, bitter pit on Honeycrisp appeared clearly through 450, 680 and 740 nm bandpass filters and also broadband images through the 710 nm highpass filter and the image captured without filter (NF). It was unclear in the 550 nm image and in NIR images captured through 880, 905 and 940 nm bandpass filters. Under FVIS mode, bitter pit was also clearly visible through 680 and somewhat visible at 740 nm bandpass filter and 710 nm highpass filter. Highest contrast of bitter pit was achieved under FUV mode through the 680 nm filter. However, FUV mode did not reveal bitter pit at all through 550 and 905 nm filters (Figure 4.1a).

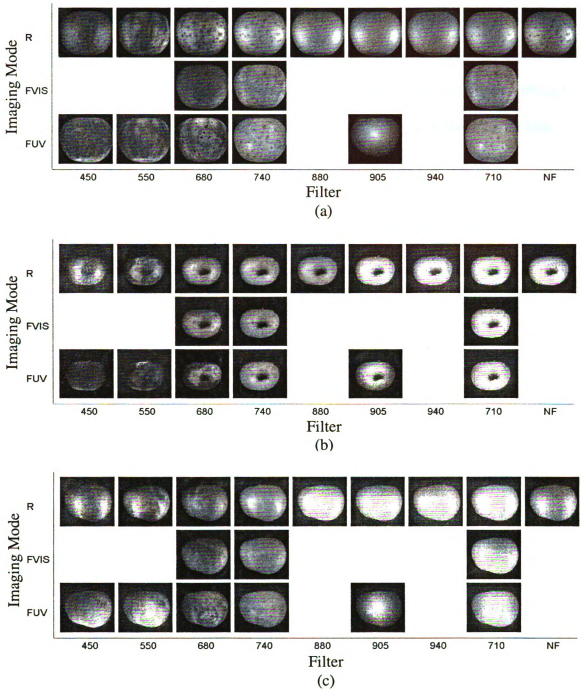

Figure 4.1. Examples of single apple image sets with various defect types. (a) bitter pit on Honeycrisp, (b) soft scald, decay, and black rot on Honeycrisp, (c) superficial scald on Red Delicious. (Each individual image was linearly stretched to achieve optimal visual contrast). Imaging modes: reflectance (R); visible-light-induced fluorescence (FVIS); and UV-induced fluorescence (FUV). Filters: numbers indicate peak wavelength (nm) of bandpass filters except 710 is cut-off wavelength (nm) of the highpass filter and NF=no filter.

Combined defects of soft scald, decay and black rot on a single Honeycrisp apple appeared in some samples (for example Fig 4.1b). Through this mix of defects in images, we can better compare how each defect appears under different lighting modes. Black rot and decay appeared in all filters under reflectance mode except with the 450 nm filter where only decay appeared predominantly compared to black rot. These defects were hardly detectable under FUV mode through 450 and 550 nm filters. Soft scald and its border were only clearly distinguishable under reflectance mode through the 550 nm filter and under FUV mode through the 550 and 680 nm filters.

Superficial scald on Red Delicious apple (Fig 4.1c) was clearly visible only under reflectance mode through the 550 nm filter and FUV mode through 550 and 680 nm filters, with the latter yielding the best contrast among the three.

4.2. Spectral Responses

4.2.1. Reflectance

Each type of disorder, as well as normal tissue, exhibits a unique spectral signature. Disorders on Honeycrisp (Figure 4.2a) generally had separation in response at many of the observed wavelengths, which is likely to benefit classification. Under reflectance mode, multiple comparisons tests showed that normal tissues were significantly different from some defective tissues at the following filters: 550, 680, 740, 905 nm bandpass filters and 710 nm highpass filter. From those wavelengths, 680 and 740 nm bandpass filters as well as 710 nm highpass filter were able to distinguish all five tissue types on Honeycrisp (Table 4.1). These results demonstrate the potential of NIR images at 740 nm and a broadband NIR image greater than 710 nm to detect different types of defects on apple. At other NIR wavelengths such as 880, 905 and 940, decay and black rot tissues were indistinguishable. The use of a 680 nm bandpass filter, which is a red filter, has a potential to differentiate defects on apple.

Normal tissues exhibited patterns similar to that of superficial scald tissue on Redcort and Red Delicious. Reflectance response in the visible region at 450, 550, and 680 nm, both on Redcort and Red Delicious, resulted in significantly different response between normal and superficial scald tissue with the exception of reflectance response at 550 nm on Red Delicious.

NIR region response at 880, 905, 940 nm on Redcort (Figure 4.2b) demonstrated a level of difference as well as at 740 nm on Red Delicious (Figure 4.2c), as did the broadband NIR image using the 710 nm highpass filter for both varieties (Table 4.2).

In general, the responses at 450 and 680 nm were lower than at other wavelengths (Figure 4.2), especially for normal tissue. This lower value might be due to strong absorption of chlorophyll-a at blue (about 430 nm) and red (about 660 nm) portions of the spectrum (Taiz and Zeiger, 1998).

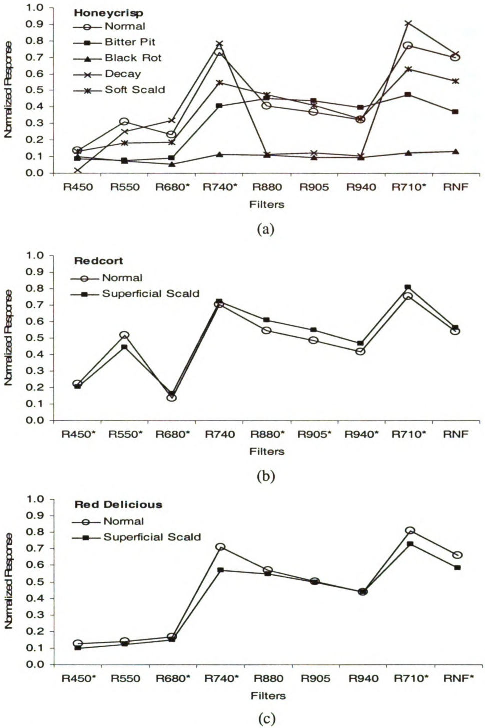

Figure 4.2. Response of VNIR reflectance of sampled pixels for various disorders of a) Honeycrisp, b) Redcort, and c) Red Delicious apple. Values are the average of the selected pixels (Table 3.3). Filters: R indicate reflectance mode, numbers indicate peak wavelength (nm) of bandpass filters except 710 is cut-off wavelength (nm) of the highpass filter and NF=no filter, * indicates significantly distinguished all tissue types.

Table 4.1. Means[1] of normalized sampled pixel values on Honeycrisp for each type of tissue

Filters[2]	Normal (n=395)	Bitter Pit (n=125)	Black Rot (n=125)	Decay (n=125)	Soft Scald (n=130)
FUV450	0.094a	0.044C	0.036c	0.074b	0.066b
FUV550	0.053a	0.028Bc	0.021c	0.046a	0.034b
FUV680	0.117b	0.033C	0.047c	0.101b	0.241a
FUV740	0.522a	0.372D	0.073e	0.444b	0.417c
FUV905	0.200a	0.187A	0.026b	0.200a	0.192a
FUV710	0.210a	0.173B	0.037c	0.204a	0.184b
FVIS680	0.312b	0.200C	0.101d	0.120d	0.395a
FVIS740	0.107a	0.062B	0.009c	0.059b	0.100a
FVIS710	0.166a	0.092C	0.019d	0.155ab	0.132b
R450	0.138a	0.086B	0.099b	0.018c	0.134a
R550	0.312a	0.078D	0.075d	0.252b	0.182c
R680	0.232b	0.093d	0.057e	0.321a	0.185c
R740	0.730b	0.409d	0.113e	0.786a	0.550c
R880	0.406b	0.451ab	0.109c	0.116c	0.477a
R905	0.370b	0.436a	0.096c	0.123c	0.412a
R940	0.324b	0.398a	0.096c	0.105c	0.330b
R710	0.770b	0.475d	0.123e	0.907a	0.629c
RNF	0.698a	0.371c	0.134d	0.720a	0.558b

[1] Means with the same letter in a row are not significantly different at α=0.05

[2] Prefixes FUV=UV-induced fluorescence, FVIS=visible-light-induced fluorescence, R=reflectance; Numbers followed prefixes indicate peak wavelength (nm) of bandpass filters except 710 is cut-off wavelength (nm) of the highpass filter and NF=no filter.

Table 4.2. Means[1] of normalized sampled pixel values on Redcort and Red Delicious for each type of tissue

Filters[2]	Redcort Normal (n=125)	Redcort Superficial Scald (n=125)	Red Delicious Normal (n=95)	Red Delicious Superficial Scald (n=75)
FUV450	0.158a	0.147a	0.139a	0.115b
FUV550	0.093a	0.072b	0.040a	0.037a
FUV680	0.317a	0.206b	0.133a	0.046b
FUV740	0.675a	0.601b	0.515a	0.378b
FUV905	0.246a	0.258a	0.212a	0.176b
FUV710	0.220a	0.216a	0.195a	0.168b
FVIS680	0.389a	0.438b	0.438a	0.338b
FVIS740	0.221a	0.213a	0.135a	0.101b
FVIS710	0.266a	0.261a	0.170a	0.136b
R450	0.224a	0.204b	0.128a	0.102b
R550	0.517a	0.444b	0.140a	0.123a
R680	0.139a	0.163b	0.166a	0.147b
R740	0.706a	0.723a	0.711a	0.571b
R880	0.546a	0.608b	0.569a	0.549a
R905	0.484a	0.549b	0.503a	0.496a
R940	0.419a	0.470b	0.441a	0.438a
R710	0.756a	0.811b	0.811a	0.728b
RNF	0.539a	0.566a	0.662a	0.585b

[1] Means with the same letter in a row for a variety are not significantly different at α=0.05
[2] Prefixes FUV=UV-induced fluorescence, FVIS=visible-light-induced fluorescence, R=reflectance; Numbers followed prefixes indicate peak wavelength (nm) of bandpass filters except 710 is cut-off wavelength (nm) of the highpass filter and NF=no filter.

4.2.2. Fluorescence

Average values of normalized responses of sampled pixels from visible light induced fluorescence and UV induced fluorescence images are shown in Figure 4.3 and Figure 4.4. In most cases, normal tissues have higher chlorophyll fluorescence emission than defective tissues, except for Redcort (Figure 4.3b) This might be due to the fact that necrotic tissues are much less likely to fluoresce (Abbott *et al.*, 1997).

Measured filter characteristics (Figure 3.2) show that the cut-off wavelengths of the 675 nm low pass intersects the 680 nm bandpass filter. Thus, in visible light induced fluorescence, some portion of reflected excitation energy was captured in the 680 nm fluorescence emission band resulting in higher response compared to 740 nm due to combined response between reflectance and fluorescence. Emission from visible light induced fluorescence had better separation of defects at 680 nm compared to 740 nm and broadband emission with the 710 nm highpass filter. For all three varieties, emission at 680 nm from visible light induced fluorescence was able to distinguish all types of tissue except black rot and decay on Honeycrisp (Table 4.1 and Table 4.2) with the recognition of the fact that it was a combined response between reflectance and fluorescence. Emission at 740 nm from visible light induced fluorescence was not able to differentiate normal from superficial scald tissues on Redcort, or normal from soft scald and bitter pit from decay tissues on Honeycrisp. Broadband emission greater than 710 nm was also unable to distinguish normal and soft scald from decay tissues on Honeycrisp, and normal from superficial scald tissues on Redcort under visible light induced fluorescence.

Under UV induced fluorescence mode, the emission patterns were similar for normal tissues and defective tissues except for black rot tissues (Figure 4.4a). Again, the normal tissues tended to give higher response compared to defective tissues. Unlike emission at 740 nm from visible light induced fluorescence, UV induced fluorescence at this bandpass resulted in better separation of defects. All types of tissues were distinguishable from each other for all three varieties at 740 nm under UV induced fluorescence. Emission at 680 nm from UV induced fluorescence also resulted in good separation of defects on Redcort and Red Delicious. On Honeycrisp, emissions at 450 and 550 nm, and broadband emission greater than 710 nm were not able to distinguish all types of tissues.

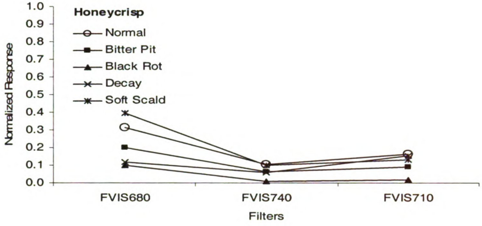

(a)

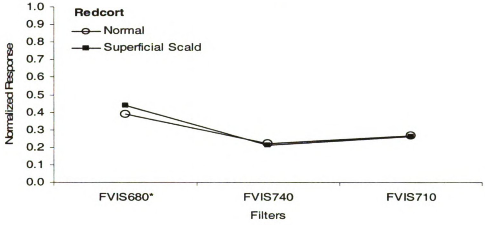

(b)

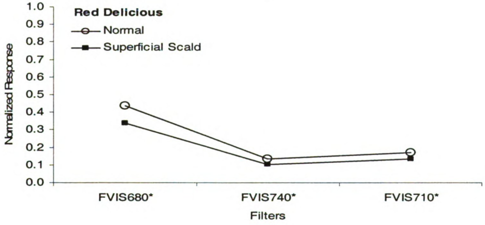

(c)

Figure 4.3. Response of visible induced fluorescence of sampled pixels for various disorders of a) Honeycrisp, b) Redcort, and c) Red Delicious apple varieties. Values are the average of selected pixels (Table 3.3) . Filters: FVIS indicate visible induced fluorescence mode, numbers indicate peak wavelength (nm) of bandpass filters except 710 is cut-off wavelength (nm) of the highpass filter and NF=no filter, * indicates significantly distinguished all tissue types.

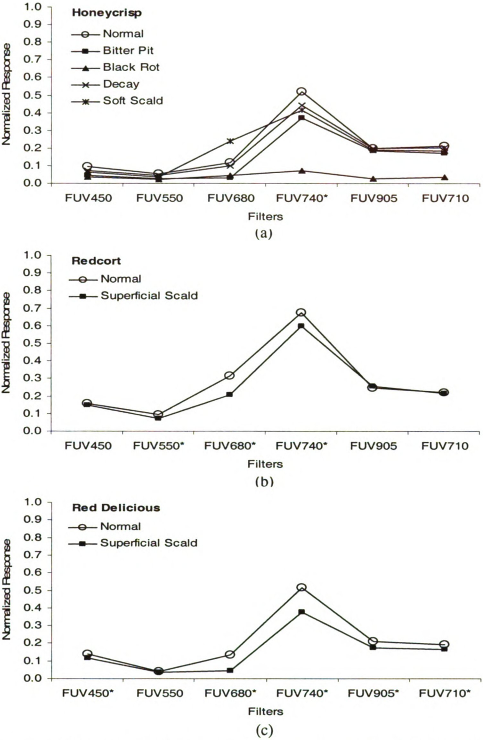

Figure 4.4. Response of UV induced fluorescence of sampled pixels for various disorders of a) Honeycrisp, b) Redcort, and c) Red Delicious apple varieties. Values are the average of selected pixels (Table 3.3). Filters: FUV indicate UV induced fluorescence mode, numbers indicate peak wavelength (nm) of bandpass filters except 710 is cut-off wavelength (nm) of the highpass filter and NF=no filter, * indicates significantly distinguished all tissue types.

4.3. Full Model Classification

Four classifiers, neural network, linear discriminant, quadratic discriminant and nearest neighbor were used to classify different disorders on apples. Table 4.3 and Table 4.4 show the classification accuracy of the full model (involving all 18 images) from two-class and multiple-class schemes respectively. Only Honeycrisp is shown under the multiple-class model as it was the only variety with multiple classes (>2) of tissues. Each entry of the tables represents the mean value from 10-fold cross validations results.

4.3.1. Two-class scheme

The total classification accuracy of Red Delicious was generally higher than the other two varieties with neural network, linear discriminant, and quadratic discriminant classifiers. The total accuracy of Red Delicious was 100% using quadratic discriminant, meaning all normal and disorder pixels were correctly classified. The classification accuracies of Red Delicious for disorder tissues were also 100% with all classifiers except with nearest neighbor classifier the accuracy was only 94%. However, the nearest neighbor classifier was superior in Honeycrisp and combined variety.

Superficial scald was the only disorder associated with Redcort and Red Delicious and thus a 2-class scheme was the only one applicable. The classification accuracy for Honeycrisp was somewhat lower than that for Redcort and Red Delicious with all classifiers except with nearest neighbor. This likely may be because of the greater number of disorders involved, i.e. bitter pit, black rot, decay, and soft scald.

The total classification accuracy for combined variety was only 83 and 88% with linear and quadratic discriminant classifiers respectively, but accuracy was good with neural network and nearest neighbor classifiers with a total accuracy of 94 and 99% respectively, which was about the same as its performance with Honeycrisp alone with nearest neighbor. However, the need for combined variety classification is unlikely to occur in real applications because usually the packinghouses only run batches of apples of the same variety. It was included in the analysis to test the performance of classifier with a broader range of data.

Table 4.3. Classification accuracy[1] of full model for 2-class scheme

Classifier/Variety	Normal	Disorder	Total
Neural Network			
Honeycrisp	94.23(0.95)	95.60(0.51)	94.90(0.67)
Redcort	96.57(1.88)	98.60(1.03)	98.00(0.89)
Red Delicious	98.00(2.00)	100.00(0.00)	99.40(0.60)
Combined[2]	92.80(0.95)	95.53(0.80)	94.17(0.53)
Linear Discriminant			
Honeycrisp	92.63(1.12)	89.97(1.28)	91.30(1.04)
Redcort	95.08(1.79)	97.47(1.32)	96.27(1.28)
Red Delicious	98.00(2.00)	100.00(0.00)	99.00(1.00)
Combined[2]	84.15(1.47)	82.35(1.21)	83.25(0.78)
Quadratic Discriminant			
Honeycrisp	89.21(1.50)	89.32(1.48)	89.26(0.73)
Redcort	95.32(2.01)	99.00(1.00)	97.16(1.17)
Red Delicious	100.00(0.00)	100.00(0.00)	100.00(0.00)
Combined[2]	90.67(1.07)	85.82(1.45)	88.24(0.73)
Nearest Neighbor			
Honeycrisp	98.68(0.61)	99.36(0.32)	99.11(0.32)
Redcort	97.29(1.11)	96.62(1.40)	96.80(0.80)
Red Delicious	98.09(1.27)	94.05(2.44)	95.88(1.53)
Combined[2]	98.85(0.42)	99.44(0.30)	99.16(0.18)

[1] means (standard error), n=10.
[2] Honeycrisp + Redcort + Red Delicious

The analysis of variance to compare the classifiers in each variety resulted in no significant differences among the classifiers for Redcort and Red Delicious at 95% confidence level except the total accuracy of Red Delicious with nearest neighbor was significantly low. In contrast, classification accuracies for Honeycrisp and combined variety were significantly different among the four classifiers. For Honeycrisp, the nearest neighbor classifier yielded the highest accuracy followed by neural network, linear discriminant and quadratic discriminant with the same order for normal, disorder and total accuracy. Similarly for combined variety, the highest accuracy was from nearest neighbor followed by neural network, quadratic discriminant, and linear discriminant consistently in this order for normal, disorder and total accuracy.

4.3.2. Multiple-class

Honeycrisp was the only variety with multiple disorders; therefore, in addition to the combined variety, it was included in multiple-class scheme classification. There were some significant differences among classifiers at the 95% confidence level both for Honeycrisp and combined variety. The nearest neighbor classifier yielded the highest total accuracy for both cases (Table 4.4), with total accuracy of 99.0% for each. The classifier perfectly recognized soft scald tissue on Honeycrisp and decay on combined variety.

Compared to the two-class scheme classification, linear and quadratic discriminant performance in multiple-class scheme was better. This might be because of the assumption of unimodal Gaussian distribution in the two-class scheme was not true, since there were actually more than one class in the 'disorder' category, therefore resulting in a multi-modal distribution.

Table 4.4. Classification accuracy[1] of full model for multiple-class scheme

Classifier/ Variety	Normal	Bitter pit	Black rot	Decay	Soft scald	Superficial Scald	Total
Neural Network							
Honeycrisp	91.6(1.7)	98.3(1.0)	94.3(2.2)	87.0(4.3)	99.3(0.5)	- -	93.6(0.9)
Combined[2]	91.2(1.1)	96.0(1.7)	90.8(1.9)	81.0(3.7)	93.9(4.0)	91.8(1.5)	91.1(0.7)
Linear Discriminant							
Honeycrisp	77.3(1.7)	99.0(1.0)	98.9(1.1)	91.8(1.2)	97.7(1.2)	- -	92.9(0.5)
Combined[2]	63.2(1.0)	98.5(1.0)	99.1(0.9)	100.0(0.0)	98.9(1.1)	87.7(2.0)	91.2(0.5)
Quadratic Discriminant							
Honeycrisp	92.2(1.2)	97.8(1.5)	98.1(1.3)	95.2(1.8)	99.4(0.6)	- -	96.5(0.8)
Combined[2]	88.9(1.1)	97.0(1.8)	98.2(1.2)	96.2(1.7)	96.9(1.6)	97.4(1.1)	95.8(0.5)
Nearest Neighbor							
Honeycrisp	98.7(0.6)	99.3(0.7)	98.9(1.1)	98.5(1.0)	100.0(0.0)	- -	99.0(0.3)
Combined[2]	98.9(0.4)	99.2(0.8)	99.3(0.7)	100.0(0.0)	99.4(0.6)	98.9(0.8)	99.0(0.2)

[1] means (standard error), n=10.
[2] Honeycrisp + Redcort + Red Delicious

4.4. Feature Selection

To find optimum subsets of the full model set of 18 features, three approaches were used: grouping features by imaging mode, grouping features by filter, and treating features individually. Then, search method(s) were applied to find optimum subsets.

4.4.1. Imaging Mode Combinations

The imaging mode combinations analyses were mainly aimed to assess the importance of each imaging mode and their combinations compared to the full model. The classification accuracy of imaging mode combinations for each classifier and variety is shown in Appendix Table A.1 through A.6. Figures 4.5 and 4.6 show the result of total classification accuracy for the 2-class and the multiple-class scheme respectively based on the nearest neighbor classifier. The nearest neighbor classifier significantly yielded the most accurate classification compared to the other three classifiers (neural network, linear discriminant, and quadratic discriminant) for each image mode combination on Honeycrisp and combined variety.

The three mode (FUV+FVIS+R) combination was equal to the full model presented in Table 4.3 and 4.4, and was the most effective combination based on the nearest neighbor classifier in all varieties although statistically was not significant from some other combinations. Therefore, there is potential to use simpler models using subsets of the 18 features, with their classification performance equal to the full model.

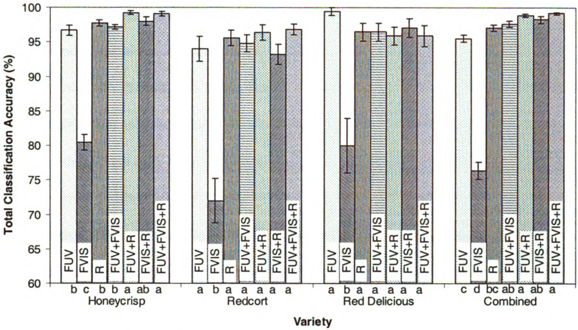

Figure 4.5. Total classification accuracy of imaging mode combinations in 2-class scheme (based on nearest neighbor classifier). Imaging mode combinations with the same letter for a variety are not significantly different at α=0.05.

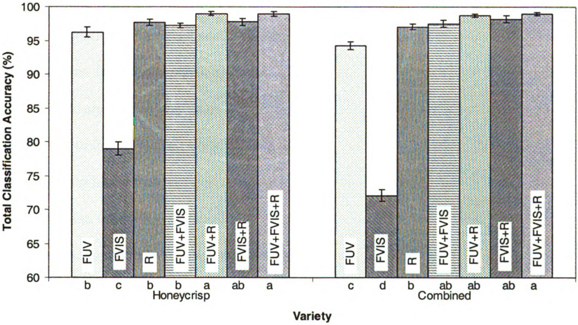

Figure 4.6. Total classification accuracy of imaging mode combinations in multiple-class scheme (based on nearest neighbor classifier). Imaging mode combinations with the same letter for a variety are not significantly different at α=0.05.

Dual-imaging models such as FUV+FVIS, FUV+R, or FVIS+R can be considered as the absence of one imaging mode from the full model, in this case the absence of R, FVIS, and FUV respectively. For all varieties, when FVIS was not present, the classification accuracy was not significantly different from the full model possibly because there were only three features in FVIS. The absence of R, or the FUV+FVIS combination, resulted in significantly lower accuracy than that of the full model in Honeycrisp. Furthermore, the FUV+FVIS combination, which can be considered fluorescence information, resulted in no significant difference in accuracy compared to R in both classification schemes indicating the classification potential of fluorescence features.

The FUV+R combination had highest accuracy of the possible dual-imaging mode combinations and was not significantly different from the full model both in the 2-class and multiple-class scheme. This result indicates the importance of integration of fluorescence and reflectance imaging for classification.

The single-imaging mode, FVIS, resulted in significantly lower accuracy compared to that of the full model for all varieties. FUV or R modes individually were significantly lower than the full model on Honeycrisp and combined variety in both classification schemes. Although FUV mode was not different from the full model in Red Delicious, its accuracy was higher (99.4%) than the full model (95.9%), indicating a potential of FUV mode to be used in detecting superficial scald in Red Delicious. FUV mode also classified black rot and soft scald on Honeycrisp with high accuracy, 100 and 99.4% respectively (Table A5 in Appendix A).

4.4.2. Filter Combinations

The results of filter combinations using all images available at a particular filter are tabulated in Appendix Table B.1 through B.6. Only the top-five combinations from each number of filters that yielded high total accuracy are presented in the table. Similarly for filter combinations within FUV and R mode only; the results are presented in Appendix Table C.1 through C.6, and D.1 through D.6. All calculations of classification accuracy were based on the nearest neighbor classifier. The maximum value of classification accuracy from each number of combined filters is plotted in Figure 4.7, 4.8, and 4.9 for all available image, FUV mode only, and R mode only respectively.

Generally, total accuracy increased as number of filters used in the model increased, but this is not the case for Redcort and Red Delicious. The total accuracy decreased after 6 and 5 filters in the model for Redcort and Red Delicious respectively (Fig 4.7 and Fig 4.9). This result suggests that classification accuracy is not a monotonic function, which is as the number of input features increase, the function output also increases. Therefore, the use of the branch and bound method to find optimum subsets might not be appropriate using classification accuracy as the evaluation function.

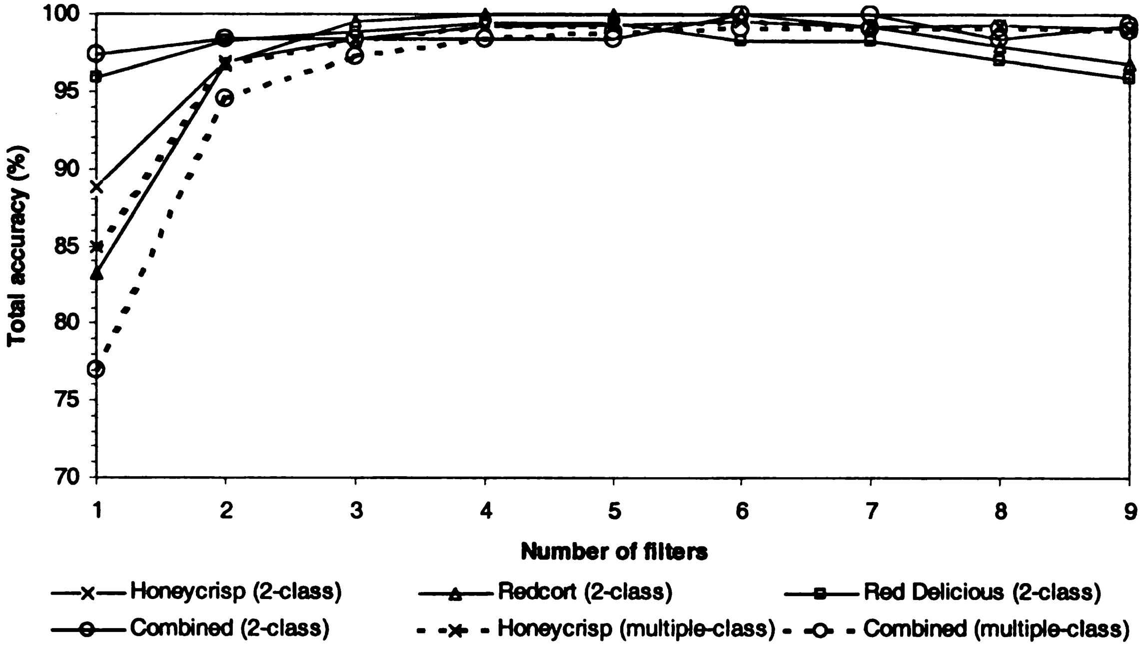

Figure 4.7. Maximum total classification accuracy from each number of combined filters using all available images in each filter

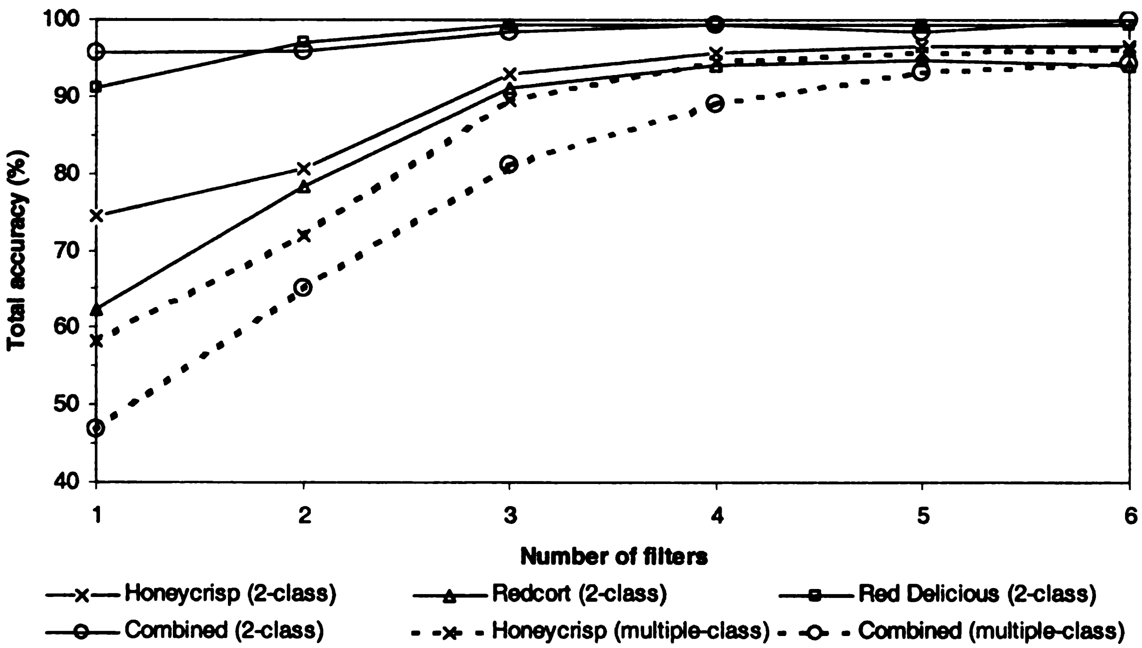

Figure 4.8. Maximum total classification accuracy from each number of combined filters within UV-induced fluorescence mode

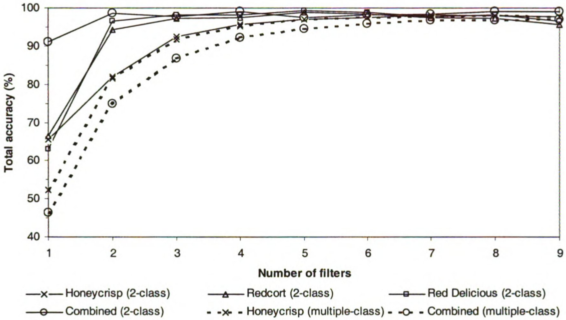

Figure 4.9. Maximum total classification accuracy from each number of combined filters within reflectance mode

The optimum number of filters was determined as the least number of filters that is not significantly different from the full model. For Honeycrisp, Redcort, Red Delicious, and combined variety the optimum number of filters was 3, 3, 2, and 4 with total classification accuracies of 98.4, 99.6, 98.2, and 98.6% respectively in the 2-class scheme. For the multiple-class scheme of Honeycrisp and combined variety the optimum number of filters was 3 and 4 with total classification accuracy 98.3 and 98.4% respectively (Table 4.5)

Filter combinations analysis derived from using all available images appeared to yield higher accuracy compared to filter combination analysis under FUV or R mode only. Eventhough the analysis using all available images resulted in a smaller filter subset, the actual number of images for the analysis was greater because it involved all three imaging modes.

The filter combination analyses under FUV or R mode alone are actually similar to the feature combinations we will discuss in Section 4.4.3, but here the combinations are restricted among features associated to FUV or R images only. These two approaches were employed based on practical consideration in a real application. It is easier to develop a sorting system with single imaging mode than multiple imaging modes.

The filter combinations analysis with three different approaches resulted in different filter sets. However, there were some filters that appeared often in each set that might be indicating the importance of the filter for the classification. For instance, the 680 and 740 nm bandpass, and 710nm high pass filters often appeared in high classification accuracy filter combinations for Honeycrisp. The 680 nm bandpass filter was also selected in most high accuracy subsets for Redcort and Red Delicious. The total accuracy of the 680 nm bandpass filter under combined imaging mode at 680 nm was 95.9% for Red Delicious (Appendix Table B.3); the major contribution was from the UV induced fluorescence image, which gave 91.2% total accuracy (Appendix Table C.3). The importance of 680 and 740 nm bandpass filter may be associated with the peak of chlorophyll fluorescence emission at 680 and 740 nm (Kim *et al.*, 2001b).

Red Delicious was the only variety that required only two filters to get high (>95%) classification accuracy; under the FUV mode the best filter combination was 450 and 680 nm bandpass filters, whereas under R mode it was the 740 and 905 nm bandpass filters. As indicated in the imaging mode combinations, FUV or R mode alone surpassed the full model on Red Delicious, therefore supporting the findings in the filter combination analysis.

Table 4.5. Optimum number[1] of filters for each variety following filter combination approach

Variety	All available images	FUV images only	R images only
Honeycrisp (2-Class)	3 (98.44) {680,740,710}	4 (95.67) {450,680,740,710}	5 (97.00) {740,880,905,940,710}
Redcort (2-Class)	3 (99.60) {550,680,905}	4 (94.00) {450,550,680,905}	3 (97.20) {740,905,NF}
Red Delicious (2-Class)	2 (98.24) {740,905}	2 (97.06) {450,680}	2 (96.47) {740,905}
Combined[2] (2-Class)	4 (98.56) {450,680,740,940}	5 (94.39) {450,680,740,905,710}	6 (96.52) {450,550,680,740,905,710}
Honeycrisp (multiple-class)	3 (98.33) {680,740,710}	4 (94.56) {450,680,740,710}	5 (97.00) {740,880,905,940,710}
Combined[2] (multiple-class)	4 (98.41) {450,680,740,940}	5 (93.11) {450,550,680,740,710}	6 (95.83) {450,550,680,740,905,NF}

[1] Numbers in parentheses indicate total classification accuracy; numbers in curly bracket indicate filter set

[2] Honeycrisp + Redcort + Red Delicious

4.4.3. Feature Combinations

Four search methods to find the best subsets of features were employed, i.e. complete search, backward elimination, principal component analysis, and neural network weights.

4.4.3.1. Complete Search

Feature selection using a complete or exhaustive search can become computationally infeasible, even though the optimality of the feature subset is guaranteed. The branch and bound method has been introduced to find optimal subsets without doing a complete search, however, this method required the assumption of a monotonic function during the search of optimal subsets (Narendra and Fukunaga, 1977). Classification accuracy or classification error is not a monotonic function as shown in the results in section 4.4.2.

In this study, a complete search method from subset features of size one through four is still computationally feasible and was employed to find optimal subsets from the 18 features. The choice of subsets up to four features was based on practical consideration in real applications. Common aperture cameras with up to four filters have become increasingly popular in multispectral imaging applications.

Table E.1 through E.6 in Appendix shows the top-five highest accuracy feature combinations resulting from the complete search with the nearest neighbor classifier from one through four feature combinations. The plot of classification accuracy of each of the 18 features is shown in Figure 4.10. Using only one feature (images), the average total classification accuracy under 2-class scheme was only about 60%. However, FUV680 for Red Delicious yielded 95% total accuracy, a quite high accuracy considering only one feature involved. FUV680 significantly yielded higher accuracy than R680 on Redcort and Red Delicious. FUV740 also yielded high total accuracy (about 75%) for Honeycrisp, Red Delicious and combined variety and significantly higher than R740. These results demonstrate the value of fluorescence mode especially its emission at 680 and 740 nm.

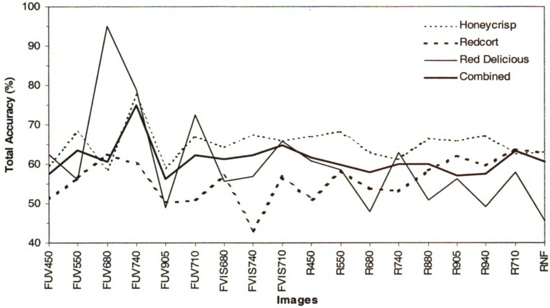

(a)

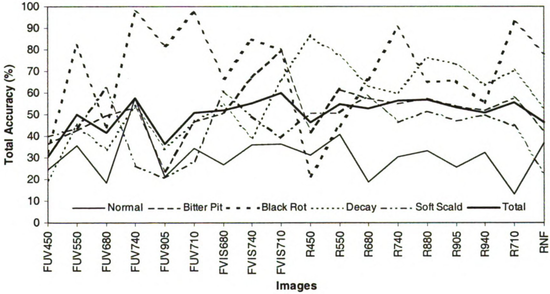

(b)

Figure 4.10. Total classification accuracy based on nearest neighbor using single image: a) 2-class scheme, b) multiple-class scheme on Honeycrisp. Prefixes FUV=UV-induced fluorescence, FVIS=visible-light-induced fluorescence, R=reflectance; Numbers followed prefix indicate peak wavelength (nm) of bandpass filters except 710 is cut-off wavelength (nm) of the highpass filter and NF=no filter.

In the multiple-class scheme on Honeycrisp, black rot could easily recognized with several single different features, such as FUV740, FUV710, R740, and R710 with accuracy 97.3, 97.3, 90.1, and 90.2% respectively. Similarly, decay can be recognized using R450 with accuracy 86.6%.

Total classification accuracy of Honeycrisp in the 2-class scheme reached a maximum of 93% using three features (FUV680, FUV740, and FUV710), and 96.6% using four features (FUV680, FUV740, FUV710, and FVIS740). For Redcort, the two-feature combination R905 and R710 yielded 94.4% accuracy, three-feature combination R740, R905, and RNF yielded 97.2% accuracy, and four-feature combination FUV680, R740, R905, and RNF yielded 98.8% accuracy, surpassing the full model accuracy (96.8%). The combination of fluorescence images FUV450 and FUV680 for Red Delicious yielded 97.1% accuracy, three-feature combination FUV740, FUV905, and FUV710 achieved 99.4% accuracy, and four-feature combination FUV680, R740, R905, and R710 achieved 99.4%, all surpassing the full model accuracy (95.9%). From these optimum subset features, either fluorescence imaging alone, or combined with reflectance imaging, make a significant contribution to the classification accuracy.

4.4.3.2. Backward Elimination

Figure 4.11 shows the performance of total accuracy as features were eliminated from the full model. For Honeycrisp in the 2-class scheme, the total accuracy started to significantly decrease after elimination of 11 features. At this point the total accuracy was 98.3% and the remaining features in the model were FUV450, FUV680, FUV740, FUV710, R450, R880, and R940. For Redcort, the accuracy started to decrease after elimination of 13 features. Total accuracy was 98.4% and the remaining features in the model were FUV740, R550, R680, R740, and R905. For Red Delicious, total accuracy started to decrease significantly after elimination of 16 features, meaning only two features were left in the model, where total accuracy was 94.7% and the remaining features were R740 and R940. For Honeycrisp in multiple-class scheme, after elimination of 11 features, the total accuracy started to significantly decrease. At this point the accuracy was 98.0% and the remaining features in the model were FUV740, FVIS740, R450, R740, R880, R940, and RNF. Some important filters identified from filter combination analysis such as 680 and 740 nm also appeared in the results of the backward elimination process.

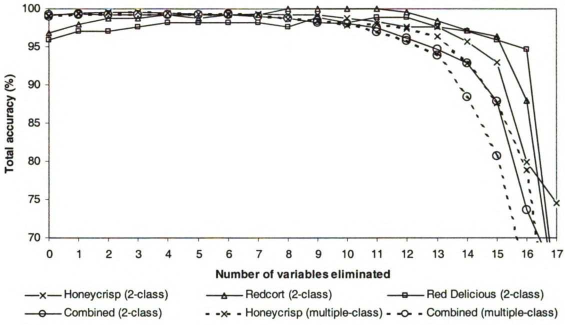

Figure 4.11. Total classification accuracy based on nearest neighbor on each step of backward elimination process

A heuristic search such as backward elimination results in suboptimal subsets compared to a complete search that is guaranteed to find optimal subsets. This suboptimality can be seen from the Red Delicious result. The complete search found FUV450 and FUV680 to be the best 2-features combination with 97.1% accuracy, meanwhile, backward elimination found R740 and R940 combination with 94.7%. However, the backward elimination process has the advantage of having a lower computational load.

4.4.3.3. Principal Component Analysis

The first four principal components contributed to at least 90% of the variation of the data set. There was similarity in the pattern of the absolute value of the eigenvector coefficient for each feature for each variety. The most important features were identified from each principal component as a base for feature selection. For example, in the first and second principal component the most important features were R710 and R880 for Honeycrisp (Figure 4.12).

The results of principal component analysis were different from the results of backward elimination, but some features were selected in both the backward elimination method and PCA, such as FUV680 and FUV740 on Honeycrisp. Generally, the optimum number of features based on PCA is larger than findings based on the backward elimination process. For example, PCA concluded the optimum number of feature for Honeycrisp was 10 with total accuracy 98.3% (Table 4.6); meanwhile, the backward elimination result was only 7 features with the same accuracy.

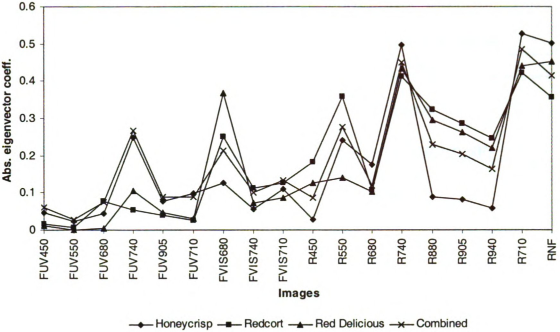

(a)

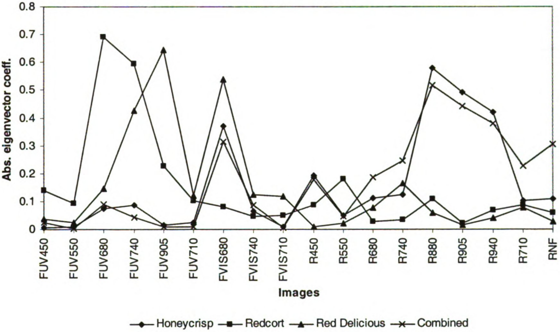

(b)

Figure 4.12. Absolute value of eigenvector coefficient of: a) first principal component, b) second principal component

Table 4.6. Optimum number[1] of filters for each variety based on PCA method

Variety	Method B2	Method B4
Honeycrisp	10 (98.33) {FUV:680,740,905, FVIS:710} R:550,680,740,940,710,NF}	10 (98.00) {FUV:680,740,905, FVIS:710, R:550,680,740,880,710,NF}
Redcort	5 (98.00) {FUV:680,905, FVIS:680, R:550,880}	5 (96.80) {FUV:680,905, FVIS:680, R:550,710}
Red Delicious	5 (97.06) {FUV:740, FVIS:680, R:550,905,NF}	4 (96.47) {FUV:680,905, FVIS:680, R:NF}
Combined[2]	10 (97.95) {FUV:680,740,905, FVIS:680,710, R:550,740,905,710,NF}	10 (97.95) {FUV:680,740,905, FVIS:680,710, R:550,740,880,710,NF}

[1] Numbers in parentheses indicate total classification accuracy; numbers in curly bracket indicate feature
[2] Honeycrisp + Redcort + Red Delicious

PCA method B2 and method B4 resulted in the same number of features except in Red Delicious; and also the selected features were similar, only one or two features were different.

The advantage of this analysis compared to backward elimination was less computation load, because determination of selected features in each step is based on rank of eigenvector coefficients and is not based on classifier evaluation.

4.4.3.4. Neural Network Weights

Table 4.7 summarizes the result of applying neural network weight methodology for feature selection. Note that the classification accuracy presented in the table was the nearest neighbor results because its result surpassed the neural network's; although neural network was used to select features by examining its weights in each backward elimination step.

The optimum subset selected by the neural network weight evaluation method was different compared to previous methods such as backward elimination and principal component analysis. The accuracy of the optimum subset features resulting from the neural network method was somewhat lower compared to the regular backward elimination and principal component method. It might be because the instability of the neural network. Small changes in training data or learning parameters could lead to a very different model. An ensemble solution has been proposed (Cunningham *et al.*, 2000), but it would lead to a more complex model.

Despite the results, the interpretation of neural network weights as a means to select input features takes a definite step toward overcoming what is possibly the primary criticism of neural networks as complex and mysterious black boxes.

Table 4.7. Optimum number of filter for each variety based on neural network weight method

Variety	Number of features	Accuracy[1]	Feature list
Honeycrisp (2-class)	9	97.78	{FUV:450,680, FVIS:740,710, R:550,680,905,940,710}
Redcort (2-class)	6	94.00	{FVIS:740,710, R:740,905,940,710}
Red Delicious (2-class)	4	90.59	{FUV550, R:450,905,710}
Combined[2] (2-class)	9	97.73	{FUV:550,740, FVIS740, R:450,550,740,905,940,710}
Honeycrisp (multiple-class)	8	97.78	{FUV:550,710, FVIS:740 R:450,550,680,940,710}
Combined[2] (multiple-class)	9	97.20	{FUV:550, FVIS:740,710, R:450,550,740,905,940,710}

[1] calculated based on nearest neighbor classifier
[2] Honeycrisp + Redcort + Red Delicious

5. CONCLUSIONS

5.1. Spectral Responses

Spectral reflectance responses at 680 or 740 nm were able to distinguish all five different tissue types on Honeycrisp. These results demonstrate that the utilization of a 680 nm bandpass filter, which is a red filter, and also NIR images at 740 nm, have a potential to differentiate defects on apple.

Normal tissues exhibited spectral patterns similar to those of superficial scald tissue on Redcort and Red Delicious. However, NIR reflectance at 880, 905, and 940 nm on Redcort demonstrated a level of difference between the two tissue types. Tissue response differences for Red Delicious were noted at 740 nm. Broadband NIR images using the 710 nm highpass filter showed tissue differences for both Red Delicious and Redcort.

Emission at 680 nm from visible light induced fluorescence was able to distinguish all types of tissue for all three varieties, except black rot and decay on Honeycrisp. However, emission at 680 nm from UV induced fluorescence was only effective in distinguishing normal from defective tissue for Redcort and Red Delicious. Fluorescence emission at 740 nm from UV excitation was also able to distinguish all different types of tissue for all three varieties.

5.2. Full Model

For the full model, integrating all three imaging modes, the total classification accuracy from the nearest neighbor classifier under the 2-class scheme was 99.1, 96.8, 95.9, and 99.2% for Honeycrisp, Redcort, Red Delicious, and combined variety respectively. Furthermore, in the multiple-class scheme, the classification accuracy of Honeycrisp apple for normal, bitter pit, black rot, decay, and soft scald was 98.7, 99.3, 98.9, 98.5, and 100%, respectively. These results demonstrate the potential of this technique to accurately recognize different types of disorder.

For Honeycrisp and combined variety, the nearest neighbor classifier yielded the highest accuracy followed by neural network, linear discriminant and quadratic discriminant classifiers. There were no significant differences among classifiers on Redcort and Red Delicious.

5.3. Reduced-feature Models

Classification accuracy from the dual-imaging mode of FUV+R performed equally to the full model in the 2-class scheme for all varieties. Especially on Honeycrisp, the classification accuracy of single imaging mode FUV or R alone is significantly lower than that of the full model, but the combination of the two imaging modes, FUV+R, is equal to that of the full model. This result demonstrates the potential of integrating fluorescence and reflectance.

The FUV mode has a potential to detect superficial scald in Red Delicious. The FUV mode also classified black rot and soft scald on Honeycrisp with high accuracy, 100 and 99.4% respectively. Furthermore, FUV680 yielded significantly higher accuracy than R680 on Redcort and Red Delicious. FUV740 also yielded higher total accuracy than R740 for Honeycrisp, Red Delicious and combined variety. These results demonstrate the value of fluorescence mode especially its emission at 680 and 740 nm. These results, especially fluorescence emission at 740 nm agreed with Beaudry *et al.*, (1998) who found this wavelength useful for non-destructive detection of fruit and vegetable quality.

Several important wavelengths were identified from the filter combination analysis, i.e. 680, 740, 905 nm. Reflectance at 680 relates to red color, and fluorescence response at 680 and 740 relates to the peaks of chlorophyll fluorescence emission, whereas, the 905 NIR responses may relate to tissue physical characteristics.

Red Delicious required only two filters to achieve high classification accuracy; in the FUV mode the best filter combination was 450 and 680 nm bandpass filters with accuracy 97.1%, whereas in R mode the best combination was 740 and 905 nm bandpass filters with accuracy 96.5%. Honeycrisp and Redcort both required 4 filters in FUV mode; 5 and 3 respectively in R mode.

Complete search found the best 4-feature model under 2-class classification scheme for Honeycrisp was FUV680, FUV740, FUV710, and FVIS740 with 96.6% accuracy; for Redcort it was FUV680, R740, R905, and RNF with 98.8% accuracy, surpassing the full model accuracy (96.8%); for Red Delicious was FUV680, R740, R905, and R710 with 99.4% accuracy, also surpassing the full model accuracy (95.9%); and for combined variety it was FVIS710, R740, R905, and R710 with 94.7% accuracy.

Three heuristic search methods: backward elimination, principal component analysis and neural network weights were also used to find the best subsets of features.

Although the results were suboptimal compared to a complete search, these methods provided the versatility of less computational load to evaluate subsets. The methods resulted in different subsets of features.

5.4. General

It was demonstrated multispectral imaging under fluorescence and reflectance modes is a useful tool for apple disorder classification. In addition to spatial information, multispectral imaging gives spectral information, which is useful for distinguishing different types of disorders.

The classifier performed better in single variety training as opposed to combined variety training. This result is also in line with the current operation in packing houses that runs batches of apples of the same variety.

6. APLICATIONS AND PERSPECTIVE

6.1. Image-based classification

Pixel-based classification was demonstrated to have a potential in classification of normal from disorder tissue on apple, furthermore recognizing specific types of disorder on apple. Throughout the dissertation the use of multispectral images, especially the spectral dimension, has been explored mainly for the purpose of feature (image) selection to be used in practical application. However, the spatial information from the multispectral images has not been fully utilized. In this section, an example is showed of how we can extend the pixel-based classification to image-based classification by utilizing spatial information, which is truly the important factor in the real application.

The best subset of the 4-features models from the complete search method on Honeycrisp under the multiple-class scheme was FVIS710, R740, R905 and R940. Figure 6.1 displays the raw image of an apple captured on wavelength under FUV mode and the classification results using all features and the optimum 4-features. Figure 6.1a shows composite disorder image of Honeycrisp containing soft scald (large irregular area), decay (area inside soft scald) and black rot (black area inside decay). The result of pixel-based classification with the full model clearly segmented these disorder areas (Figure 6.1b). In Figure 6.1b, the outer border pixels of apples were classified to black rot.

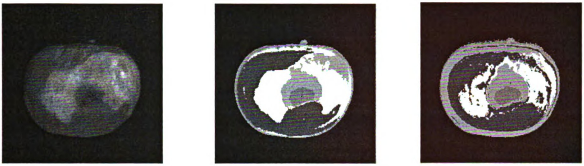

(a) (b) (c)

Figure 6.1. Images built from pixel-based classification. (a) Original FUV550 image, (b) Full model, (c) 4-feature model.

On the other hand, the classification model using 4-features produced results with less clear separation of disorders (Figure 6.1c). In the 4-feature model the classification of pixels near the edge of the apple were not properly classified and some soft scald area was classified into normal tissue. This problem might be affected by the apple curvature. As curvature of the apple comes strongly into play, further utilization of imaging and image processing potential by incorporating spatial information becomes an important step in apple disorder detection. Some image enhancement techniques in the spatial domain applied to original multispectral images and/or to classification result images may be used to obtain better segmentation of disorder areas. An adaptive spherical image transform proposed by Tao and Wen (1999) has been proven to effectively compensate for the reflectance intensity gradient on curved objects such as apple, and it may be applied to the original multispectral data. Furthermore, as an example, spatial filtering such as smoothing, which takes into consideration neighboring pixels, may be applied to classification result images to enhance classification of the specific areas of tissue.

Computation speed becomes a main concern in on-line applications, therefore, an efficient algorithm needs to be applied. Although from the classification results the nearest neighbor classifier performed better than the neural network classifier, computation-wise, neural network is preferred during the classification task of new images. Neural networks have more computational load during training compared to nearest neighbor; on the other hand, neural networks have less computational load during classification of new images compare to nearest neighbor operations.

6.2. Generality of the classification model

It might be preferable if there is a set of features that works for all different varieties. The best 4-feature model from combined variety resulting from the complete search method was chosen to assess the performance of a set of features when it is applied to every different variety. Randomly selected pixels from Honeycrisp, Redcort and Red Delicious were classified with this model using the nearest neighbor classifier. The result is shown in Table 6.1.

Table 6.1. Classification accuracy of the best 4-feature model (FVIS710, R740, R905, R710) of combined variety applied to each variety (based on nearest neighbor classifier)

Variety	Normal	Disorder	Total
Honeycrisp (n=225)	91.8	96.9	94.7
Redcort (n=62)	96.4	91.2	93.5
Red Delicious (n=42)	85.7	81.0	83.3

There is a considerable classification accuracy drop if we compare the total accuracy from Table 6.1 to the total accuracy if we select the best 4-feature model for each variety (see Appendix Table E.1 through E.3), which is 96.6, 98.8, and 99.4% for Honeycrisp, Redcort, and Red Delicious respectively. Thus, the convenience of having a set of features that works for all varieties resulted in lower classification accuracy.

Another issue related to the generality or robustness of the classification model is how well the classification model with an optimal combination of features applies to the same variety of apples from different orchards or from different harvest seasons. Inclusion of data acquired from different orchards and harvest seasons in the training set may produce more robust classifiers.

6.3. Recommendations

It has been demonstrated that fluorescence imaging has a potential to detect disorder on apples. However, due to low fluorescence emission, longer exposure time is needed to acquire the image, which may not be feasible for on-line application. To shorten exposure time, the use of more sensitive and cooled cameras to reduce noise is recommended in addition to methods to increase incident light onto the apples.

Uniform illumination is very important in machine vision applications; therefore, better lighting design is a critical step. A good diffuser design is necessary to provide uniform illumination, however, it must be noted that diffusers also block some light energy. Dome-like light housing incorporated with LED lighting may be a good alternative for illumination.

APPENDICES

APPENDIX A. Classification accuracy of imaging mode combination models

Table A.1. Classification accuracy[1] of imaging mode combination models on Honeycrisp (2-class scheme)

Lighting Mode	Normal	Disorder	Total
Neural Network			
FUV	82.80(3.21)	73.87(1.77)	77.44(1.66)
FVIS	11.66(2.17)	97.17(0.61)	59.63(1.51)
R	88.07(1.43)	92.70(1.32)	90.70(1.12)
FUV+FVIS	84.90(1.25)	85.09(1.93)	84.78(0.96)
FUV+R	93.22(0.91)	96.29(0.69)	94.93(0.50)
FVIS+R	87.70(1.86)	92.98(0.95)	90.63(0.93)
FUV+FVIS+R	92.63(0.94)	95.97(0.65)	94.44(0.52)
Linear Discriminant			
FUV	86.50(1.48)	76.91(1.71)	81.71(0.80)
FVIS	73.00(1.87)	70.88(2.26)	71.94(1.07)
R	77.98(1.72)	81.22(1.52)	79.60(1.30)
FUV+FVIS	85.68(2.23)	81.45(1.96)	83.56(1.06)
FUV+R	90.26(1.45)	87.52(1.44)	88.89(1.02)
FVIS+R	80.93(1.37)	84.41(1.04)	82.67(0.79)
FUV+FVIS+R	92.62(1.12)	89.97(1.28)	91.30(1.04)
Quadratic Discriminant			
FUV	90.58(1.43)	79.91(1.32)	85.24(1.09)
FVIS	63.28(2.92)	77.61(1.46)	70.44(1.67)
R	79.61(2.03)	85.94(1.10)	82.77(1.32)
FUV+FVIS	87.74(1.83)	86.76(1.43)	87.25(0.60)
FUV+R	90.34(1.71)	89.89(1.33)	90.12(0.99)
FVIS+R	84.63(1.80)	84.31(1.19)	84.47(1.34)
FUV+FVIS+R	89.21(1.50)	89.32(1.48)	89.26(0.73)
Nearest Neighbor			
FUV	94.27(1.19)	98.61(0.53)	96.67(0.72)
FVIS	74.05(2.19)	85.16(1.85)	80.44(1.13)
R	96.23(0.69)	99.01(0.33)	97.78(0.44)
FUV+FVIS	95.61(0.94)	98.40(0.51)	97.23(0.34)
FUV+R	98.69(0.70)	99.60(0.27)	99.22(0.29)
FVIS+R	96.50(0.90)	99.17(0.47)	98.00(0.59)
FUV+FVIS+R	98.68(0.61)	99.36(0.32)	99.11(0.32)

[1] means (standard error), n=10.

Table A.2. Classification accuracy[1] of imaging mode combination models on Redcort (2-class scheme)

Lighting Mode	Normal	Disorder	Total
Neural Network			
FUV	93.94(2.23)	96.93(1.35)	95.60(1.50)
FVIS	58.19(6.29)	79.58(4.76)	70.27(3.58)
R	93.58(2.30)	94.80(1.93)	94.67(1.38)
FUV+FVIS	93.09(2.69)	96.99(1.35)	95.60(1.27)
FUV+R	96.98(2.01)	98.61(1.03)	98.13(0.98)
FVIS+R	96.61(1.33)	96.35(1.28)	96.67(0.75)
FUV+FVIS+R	96.78(1.88)	98.61(1.03)	98.13(0.87)
Linear Discriminant			
FUV	87.49(3.27)	93.55(2.00)	90.52(1.90)
FVIS	66.98(4.19)	71.54(3.32)	69.26(2.18)
R	91.81(3.61)	97.26(1.40)	94.53(1.99)
FUV+FVIS	89.03(2.80)	93.62(1.57)	91.32(1.69)
FUV+R	95.08(1.79)	99.00(1.00)	97.04(1.07)
FVIS+R	93.73(2.63)	96.63(1.41)	95.18(1.58)
FUV+FVIS+R	95.08(1.79)	97.47(1.32)	96.27(1.28)
Quadratic Discriminant			
FUV	94.36(2.54)	91.51(2.45)	92.93(1.96)
FVIS	70.82(1.75)	72.18(3.18)	71.50(2.08)
R	93.30(2.71)	94.48(1.99)	93.89(1.36)
FUV+FVIS	94.31(2.34)	92.44(2.06)	93.38(1.38)
FUV+R	91.91(3.74)	97.61(1.25)	94.76(1.79)
FVIS+R	94.11(1.78)	99.00(1.00)	96.55(1.04)
FUV+FVIS+R	95.32(2.01)	99.00(1.00)	97.16(1.17)
Nearest Neighbor			
FUV	92.50(3.36)	94.62(2.45)	94.00(1.81)
FVIS	71.63(4.45)	71.60(3.52)	72.00(3.21)
R	95.87(1.78)	94.79(1.90)	95.60(1.11)
FUV+FVIS	91.65(3.33)	96.75(1.85)	94.80(1.20)
FUV+R	97.17(1.53)	95.62(1.48)	96.40(1.11)
FVIS+R	92.56(2.77)	93.21(2.74)	93.20(1.47)
FUV+FVIS+R	97.29(1.11)	96.62(1.40)	96.80(0.80)

[1] means (standard error), n=10.

Table A.3. Classification accuracy[1] of imaging mode combination models on Red Delicious (2-class scheme)

Lighting Mode	Normal	Disorder	Total
Neural Network			
FUV	99.00(1.00)	100.00(0.00)	99.41(0.59)
FVIS	83.67(3.28)	45.19(8.03)	67.45(3.97)
R	96.06(2.26)	97.86(1.68)	96.86(1.90)
FUV+FVIS	97.33(2.04)	99.44(0.56)	98.63(1.01)
FUV+R	98.36(1.33)	99.72(0.28)	99.22(0.60)
FVIS+R	96.70(2.11)	99.17(0.83)	98.04(1.24)
FUV+FVIS+R	97.70(1.99)	100.00(0.00)	99.22(0.60)
Linear Discriminant			
FUV	96.00(2.21)	100.00(0.00)	98.00(1.11)
FVIS	67.43(4.67)	81.15(4.04)	74.29(2.91)
R	96.18(2.16)	100.00(0.00)	98.09(1.08)
FUV+FVIS	98.00(2.00)	100.00(0.00)	99.00(1.00)
FUV+R	97.09(2.10)	100.00(0.00)	98.55(1.05)
FVIS+R	96.18(2.55)	98.57(1.43)	97.38(1.35)
FUV+FVIS+R	98.00(2.00)	100.00(0.00)	99.00(1.00)
Quadratic Discriminant			
FUV	99.00(1.00)	100.00(0.00)	99.50(0.50)
FVIS	64.84(5.34)	83.45(4.64)	74.15(3.86)
R	97.09(2.10)	94.96(2.16)	96.03(1.54)
FUV+FVIS	100.00(0.00)	99.17(0.83)	99.58(0.42)
FUV+R	100.00(0.00)	99.17(0.83)	99.58(0.42)
FVIS+R	100.00(0.00)	100.00(0.00)	100.00(0.00)
FUV+FVIS+R	100.00(0.00)	100.00(0.00)	100.00(0.00)
Nearest Neighbor			
FUV	99.00(1.00)	100.00(0.00)	99.41(0.59)
FVIS	81.55(3.63)	77.54(5.99)	80.00(3.94)
R	96.09(2.19)	96.63(1.77)	96.47(1.30)
FUV+FVIS	96.18(1.56)	98.33(1.67)	96.47(1.30)
FUV+R	95.27(2.17)	97.74(1.57)	95.88(1.26)
FVIS+R	98.00(1.33)	96.03(2.04)	97.06(1.31)
FUV+FVIS+R	98.09(1.27)	94.05(2.44)	95.88(1.53)

[1] means (standard error), n=10.

Table A.4. Classification accuracy[1] of imaging mode combination models on combined variety (2-class scheme)

Lighting Mode	Normal	Disorder	Total
Neural Network			
FUV	84.98(1.11)	66.09(1.12)	74.97(0.77)
FVIS	22.42(2.14)	90.50(1.27)	58.84(0.94)
R	88.04(1.39)	90.18(0.75)	89.12(0.58)
FUV+FVIS	84.76(1.13)	83.44(1.04)	84.04(0.46)
FUV+R	91.28(1.32)	95.29(0.48)	93.36(0.71)
FVIS+R	87.01(1.05)	91.64(0.45)	89.47(0.38)
FUV+FVIS+R	91.88(1.08)	94.90(0.78)	93.51(0.38)
Linear Discriminant			
FUV	84.12(1.58)	68.80(1.73)	76.46(1.19)
FVIS	65.91(1.86)	64.47(1.82)	65.19(1.38)
R	74.87(1.93)	74.95(0.91)	74.91(0.77)
FUV+FVIS	80.83(1.61)	71.20(1.54)	76.01(1.05)
FUV+R	83.50(1.74)	81.51(1.25)	82.50(0.77)
FVIS+R	75.47(1.69)	75.51(1.10)	75.49(0.91)
FUV+FVIS+R	84.15(1.47)	82.35(1.21)	83.25(0.78)
Quadratic Discriminant			
FUV	87.80(1.54)	69.86(1.18)	78.83(1.03)
FVIS	50.95(1.66)	72.09(1.69)	61.52(1.31)
R	79.50(1.42)	80.26(1.48)	79.88(0.78)
FUV+FVIS	82.57(1.25)	76.48(1.36)	79.53(0.59)
FUV+R	90.19(1.32)	84.02(1.16)	87.10(0.84)
FVIS+R	77.67(1.73)	83.27(1.10)	80.47(1.14)
FUV+FVIS+R	90.67(1.07)	85.82(1.45)	88.24(0.73)
Nearest Neighbor			
FUV	93.00(0.74)	97.77(0.56)	95.53(0.55)
FVIS	71.72(2.20)	80.30(1.07)	76.36(1.23)
R	96.14(0.75)	97.87(0.78)	97.05(0.41)
FUV+FVIS	96.75(0.63)	98.46(0.48)	97.65(0.48)
FUV+R	98.36(0.56)	99.29(0.24)	98.86(0.23)
FVIS+R	97.75(0.42)	98.70(0.73)	98.26(0.52)
FUV+FVIS+R	98.85(0.42)	99.44(0.30)	99.16(0.18)

[1] means (standard error), n=10.

Table A.5. Classification accuracy[1] of imaging mode combination models on Honeycrisp (multiple-class scheme)

Lighting Mode	Normal	Bitter Pit	Black Rot	Decay	Soft Scald	Total
Neural Network						
FUV	90.68(2.24)	40.09(6.09)	70.55(4.56)	24.60(4.42)	86.51(2.65)	71.26(2.03)
FVIS	84.44(2.34)	41.23(8.19)	0.00(0.00)	51.24(5.26)	0.00(0.00)	49.85(1.44)
R	90.25(1.69)	91.42(3.58)	91.54(2.79)	74.72(6.15)	81.97(6.61)	87.33(2.03)
FUV+FVIS	86.28(1.70)	59.68(7.71)	89.49(2.73)	70.23(4.51)	92.10(4.06)	81.33(1.14)
FUV+R	92.72(1.09)	91.84(3.67)	90.35(2.19)	87.31(3.43)	93.97(3.25)	92.04(1.19)
FVIS+R	87.28(1.61)	95.68(1.30)	93.11(2.43)	80.29(3.24)	84.35(4.11)	88.15(1.27)
FUV+FVIS+R	92.96(1.23)	96.78(1.13)	94.06(2.16)	85.03(3.56)	97.85(0.92)	93.48(0.79)
Linear Discriminant						
FUV	68.08(2.37)	78.24(4.03)	98.17(1.25)	57.06(3.62)	95.02(2.30)	79.31(0.89)
FVIS	32.77(1.77)	75.91(4.00)	95.29(1.65)	49.16(5.44)	65.12(3.81)	63.65(2.05)
R	53.34(1.73)	93.82(1.58)	98.89(1.11)	94.05(1.83)	90.40(2.25)	86.10(0.72)
FUV+FVIS	70.32(2.36)	89.96(2.54)	98.17(1.25)	76.75(4.75)	96.31(1.54)	86.30(0.96)
FUV+R	73.48(1.45)	98.23(1.19)	98.89(1.11)	94.29(1.80)	96.84(1.32)	92.35(0.67)
FVIS+R	64.90(2.05)	99.23(0.77)	98.89(1.11)	91.67(1.70)	89.88(3.34)	88.91(0.87)
FUV+FVIS+R	77.26(1.70)	99.00(1.00)	98.89(1.11)	91.84(1.17)	97.67(1.21)	92.93(0.47)
Quadratic Discriminant						
FUV	66.19(1.49)	94.98(1.87)	95.35(2.54)	75.39(4.36)	98.50(1.03)	86.08(1.21)
FVIS	21.89(2.17)	86.72(3.54)	98.30(1.20)	52.97(5.85)	89.34(2.82)	69.85(1.43)
R	79.82(1.78)	96.32(1.99)	98.30(1.20)	97.62(1.74)	98.26(1.16)	94.06(0.52)
FUV+FVIS	78.03(1.14)	95.76(2.47)	95.35(2.54)	94.62(2.34)	98.50(1.03)	92.45(0.79)
FUV+R	91.16(1.17)	95.60(1.92)	98.30(1.20)	96.04(1.82)	98.50(1.03)	95.92(0.70)
FVIS+R	86.38(1.72)	99.23(0.77)	96.47(1.50)	95.21(1.81)	99.09(0.91)	95.28(0.46)
FUV+FVIS+R	92.17(1.17)	97.80(1.55)	98.06(1.31)	95.21(1.81)	99.41(0.59)	96.53(0.83)
Nearest Neighbor						
FUV	94.27(1.19)	95.90(2.15)	100.00(0.00)	95.97(1.92)	99.41(0.59)	96.22(0.76)
FVIS	74.05(2.19)	79.35(3.05)	91.73(2.60)	93.19(2.25)	65.34(2.87)	79.00(0.96)
R	96.23(0.69)	98.52(0.99)	98.89(1.11)	97.79(1.13)	100.00(0.00)	97.67(0.45)
FUV+FVIS	95.61(0.94)	95.57(1.52)	100.00(0.00)	98.38(1.09)	100.00(0.00)	97.23(0.34)
FUV+R	98.69(0.70)	99.17(0.83)	97.89(1.41)	99.29(0.71)	100.00(0.00)	99.00(0.26)
FVIS+R	96.50(0.90)	99.17(0.83)	97.89(1.41)	97.62(1.74)	100.00(0.00)	97.78(0.52)
FUV+FVIS+R	98.68(0.61)	99.29(0.71)	98.89(1.11)	98.45(1.04)	100.00(0.00)	99.00(0.35)

[1] means (standard error), n=10.

Table A.6. Classification accuracy[1] of imaging mode combination models on combined variety (multiple-class scheme)

Lighting Mode	Normal	Bitter Pit	Black Rot	Decay	Soft Scald	Superficial Scald	Total
Neural Network							
FUV	92.31(0.71)	43.44(6.22)	67.45(6.23)	19.10(2.82)	77.78(6.56)	32.24(3.83)	67.85(0.98)
FVIS	95.67(0.69)	0.00(0.00)	0.00(0.00)	37.14(5.01)	0.00(0.00)	0.00(0.00)	48.03(0.98)
R	89.21(1.39)	79.91(5.39)	86.53(4.66)	70.87(6.88)	61.83(6.73)	87.23(3.11)	83.86(1.18)
FUV+FVIS	86.19(1.24)	44.86(10.55)	85.70(1.73)	59.10(6.95)	90.95(2.98)	69.08(5.71)	77.65(1.15)
FUV+R	90.41(1.38)	93.35(3.58)	89.47(4.13)	89.65(2.66)	96.48(1.08)	93.57(0.83)	91.77(0.80)
FVIS+R	87.46(1.70)	91.60(4.01)	89.03(3.53)	82.86(3.23)	70.96(4.24)	87.68(2.05)	86.06(1.22)
FUV+FVIS+R	91.33(1.46)	96.63(1.67)	89.30(4.02)	85.23(2.93)	91.09(6.47)	84.68(7.18)	90.38(1.43)
Linear Discriminant							
FUV	48.61(1.72)	77.21(4.84)	98.33(1.14)	36.17(5.10)	88.17(3.52)	43.88(2.32)	65.40(1.22)
FVIS	9.90(1.11)	75.80(3.71)	93.61(1.53)	64.82(3.41)	66.79(3.43)	62.56(2.61)	62.25(1.15)
R	48.25(1.38)	85.09(3.79)	99.09(0.91)	99.44(0.56)	90.82(2.17)	79.13(2.83)	83.64(1.06)
FUV+FVIS	46.54(1.84)	90.55(2.35)	98.42(1.07)	92.71(1.84)	93.99(1.75)	76.61(1.36)	83.14(0.65)
FUV+R	62.74(1.36)	94.53(2.33)	99.09(0.91)	100.00(0.00)	97.64(1.58)	83.26(2.02)	89.54(0.53)
FVIS+R	50.07(1.54)	98.57(1.43)	99.09(0.91)	99.44(0.56)	94.27(2.01)	79.19(3.27)	86.77(0.90)
FUV+FVIS+R	63.24(1.03)	98.45(1.04)	99.09(0.91)	100.00(0.00)	98.89(1.11)	87.72(1.99)	91.23(0.54)
Quadratic Discriminant							
FUV	63.28(1.56)	93.62(2.02)	95.85(1.73)	73.09(3.64)	95.17(2.82)	79.93(3.25)	83.49(0.58)
FVIS	14.97(2.11)	86.40(4.76)	98.09(1.27)	59.28(3.73)	83.10(2.42)	71.45(3.18)	68.88(1.33)
R	69.95(1.75)	96.07(2.74)	98.18(1.21)	96.86(1.72)	97.90(1.09)	96.44(1.59)	92.57(0.55)
FUV+FVIS	65.44(1.19)	94.39(2.49)	95.85(1.73)	94.76(2.15)	98.19(1.31)	97.00(1.23)	90.94(0.70)
FUV+R	84.56(1.66)	94.61(3.44)	97.27(1.39)	96.86(1.72)	97.48(1.39)	97.38(1.14)	94.69(0.59)
FVIS+R	74.25(2.12)	100.00(0.00)	97.52(1.28)	97.44(1.44)	98.17(1.25)	97.41(1.13)	94.13(0.56)
FUV+FVIS+R	88.90(1.11)	96.99(1.76)	98.18(1.21)	96.19(1.71)	96.92(1.62)	97.38(1.14)	95.76(0.52)
Nearest Neighbor							
FUV	93.00(0.74)	92.91(2.34)	100.00(0.00)	94.08(1.77)	98.19(1.31)	91.93(1.34)	94.24(0.57)
FVIS	71.72(2.20)	76.02(4.09)	93.36(2.63)	95.99(1.85)	57.30(3.66)	52.59(2.08)	72.12(1.40)
R	96.14(0.75)	99.17(0.83)	99.09(0.91)	96.94(1.67)	99.44(0.56)	96.01(1.43)	97.05(0.41)
FUV+FVIS	96.75(0.63)	96.20(2.02)	99.09(0.91)	100.00(0.00)	99.44(0.56)	97.22(0.96)	97.50(0.52)
FUV+R	98.36(0.56)	100.00(0.00)	99.33(0.67)	100.00(0.00)	99.44(0.56)	98.19(0.76)	98.79(0.23)
FVIS+R	97.75(0.42)	99.17(0.83)	99.33(0.67)	98.75(1.25)	99.44(0.56)	97.05(1.60)	98.18(0.52)
FUV+FVIS+R	98.85(0.42)	99.23(0.77)	99.33(0.67)	100.00(0.00)	99.44(0.56)	98.91(0.76)	99.01(0.23)

[1] means (standard error), n=10.

APPENDIX B. Classification accuracy of filter combination models using available images.

Table B.1. Classification accuracy of filter combination models using available images on Honeycrisp (2-class scheme)

Normal	Disorder	Total	Filter Combinations
86.21	90.66	88.78	740
78.04	88.67	84.00	710
79.74	85.43	82.78	680
65.53	78.73	72.78	450
65.29	76.48	71.67	550
94.76	98.38	96.89	680 740
95.15	98.05	96.78	680 710
95.05	97.77	96.67	740 710
91.49	96.56	94.44	740 NF
87.89	97.96	93.67	550 740
97.67	98.96	98.44	680 740 710
96.79	99.17	98.22	680 740 NF
96.35	99.14	98.00	680 740 940
96.23	99.20	97.89	450 680 740
96.09	98.99	97.78	550 740 710
98.99	99.38	99.22	680 740 940 710
98.49	98.95	98.78	680 740 940 NF
98.65	98.77	98.78	680 740 880 710
97.97	99.40	98.78	450 680 740 880
97.92	99.18	98.67	680 740 905 710
99.02	99.59	99.33	680 740 940 710 NF
98.49	99.79	99.22	680 740 880 940 710
99.01	99.38	99.22	450 680 740 940 NF
98.81	99.43	99.11	450 680 740 940 710
98.36	99.60	99.11	450 680 740 880 940
99.31	99.79	99.56	680 740 880 940 710 NF
98.75	99.58	99.22	550 680 740 940 710 NF
98.46	99.79	99.22	450 680 740 905 940 710
99.01	99.38	99.22	450 680 740 880 940 NF
98.65	99.57	99.22	450 550 680 740 940 710
98.46	99.79	99.22	450 680 740 880 905 940 710
98.63	99.57	99.22	450 550 680 740 940 710 NF
98.37	99.79	99.22	450 550 680 740 880 940 710
98.81	99.45	99.11	450 680 740 880 940 710 NF
98.91	99.18	99.11	450 550 740 905 940 710 NF
98.64	99.79	99.33	450 550 680 740 880 940 710 NF
98.42	99.81	99.22	450 680 740 880 905 940 710 NF
98.65	99.57	99.22	450 550 680 740 880 905 940 NF
98.61	99.39	99.11	450 550 740 880 905 940 710 NF
98.68	99.36	99.11	450 550 680 740 905 940 710 NF
98.68	99.36	99.11	450 550 680 740 880 905 940 710 NF

Table B.2. Classification accuracy of filter combination models using available images on Redcort (2-class scheme)

Normal	Disorder	Total	Filter Combinations
80.22	85.55	83.20	680
77.15	78.74	78.00	740
73.16	69.67	71.60	710
72.44	70.10	70.40	550
66.54	70.74	68.40	905
95.68	97.45	96.80	450 680
95.49	97.09	96.40	740 905
95.11	95.17	95.60	550 680
93.99	96.33	95.20	905 710
93.98	96.45	95.20	680 740
99.33	100.00	99.60	550 680 905
99.33	99.29	99.20	450 680 905
100.00	97.17	98.80	740 905 710
98.50	99.00	98.80	680 880 NF
100.00	96.33	98.40	740 880 NF
100.00	100.00	100.00	550 680 880 905
100.00	99.41	99.60	680 740 880 NF
99.33	100.00	99.60	550 680 905 NF
98.89	100.00	99.60	550 680 905 940
98.22	100.00	99.20	550 680 940 NF
100.00	100.00	100.00	550 680 880 905 940
98.89	100.00	99.60	550 680 905 940 NF
98.89	100.00	99.60	550 680 880 940 NF
99.33	100.00	99.60	550 680 880 905 NF
98.75	100.00	99.60	550 680 740 880 NF
100.00	100.00	100.00	550 680 880 905 940 NF
100.00	100.00	100.00	550 680 740 880 940 NF
99.33	99.17	99.20	550 680 740 905 940 NF
98.67	100.00	99.20	550 680 740 880 905 NF
99.33	99.29	99.20	450 550 680 880 940 NF
99.33	99.17	99.20	550 680 740 880 905 940 NF
98.50	98.17	98.40	550 680 740 905 940 710 NF
98.67	98.58	98.40	450 680 740 880 905 940 710
97.83	99.29	98.40	450 550 680 905 940 710 NF
98.67	98.45	98.40	450 550 680 740 905 710 NF
98.67	97.68	98.00	450 550 680 740 905 940 710 NF
97.95	98.45	98.00	450 550 680 740 880 905 710 NF
98.67	96.33	97.60	550 680 740 880 905 940 710 NF
97.12	98.45	97.60	450 550 680 740 880 905 940 NF
98.67	96.62	97.60	450 550 680 740 880 905 940 710
97.29	96.62	96.80	450 550 680 740 880 905 940 710 NF

Table B.3. Classification accuracy of filter combination models using available images on Red Delicious (2-class scheme)

Normal	Disorder	Total	Filter Combinations
95.93	95.79	95.88	680
87.05	90.75	88.82	740
75.07	84.09	78.82	710
56.95	63.33	61.18	550
62.02	57.78	60.00	450
97.00	99.17	98.24	740 905
98.09	99.17	98.24	550 680
95.50	99.17	97.06	680 940
97.75	96.63	97.06	450 680
95.84	97.50	96.47	680 740
97.09	100.00	98.82	740 905 NF
100.00	97.74	98.82	740 905 710
98.00	99.17	98.82	740 905 940
98.00	100.00	98.82	680 940 NF
98.09	100.00	98.82	680 940 710
100.00	99.17	99.41	740 880 905 940
97.00	100.00	98.82	740 880 905 NF
98.00	100.00	98.82	680 880 940 NF
98.09	100.00	98.82	680 880 940 710
98.00	100.00	98.82	680 740 940 NF
98.00	100.00	99.41	680 740 880 905 710
98.09	100.00	98.82	740 880 905 940 NF
99.00	98.57	98.82	450 680 880 940 NF
98.00	97.74	98.24	740 880 905 710 NF
97.84	98.57	98.24	680 740 905 940 710
99.09	97.74	98.24	740 880 905 940 710 NF
96.84	100.00	98.24	680 880 905 940 710 NF
98.09	99.17	98.24	680 740 880 905 710 NF
99.00	97.74	98.24	550 680 880 940 710 NF
98.09	98.57	98.24	550 680 880 905 940 NF
99.09	97.74	98.24	550 740 880 905 940 710 NF
98.09	98.57	98.24	550 680 880 905 940 710 NF
97.00	98.57	98.24	450 550 740 880 940 710 NF
97.18	98.57	97.65	450 550 680 880 905 940 NF
96.00	98.57	97.65	450 550 680 740 940 710 NF
95.00	97.14	97.06	450 550 680 740 880 940 710 NF
97.75	94.88	96.47	550 680 740 880 905 940 710 NF
98.09	94.05	95.88	450 550 740 880 905 940 710 NF
97.09	95.48	95.88	450 550 680 740 905 940 710 NF
97.00	94.05	95.88	450 550 680 740 880 905 710 NF
98.09	94.05	95.88	450 550 680 740 880 905 940 710 NF

Table B.4. Classification accuracy of filter combination models using available images on combined variety (2-class scheme)

Normal	Disorder	Total	Filter Combinations
79.53	86.07	83.03	740
73.29	80.35	77.12	710
73.41	79.72	76.67	680
60.38	69.69	65.23	450
58.08	65.82	62.20	550
93.18	96.78	95.08	680 740
92.04	96.72	94.55	680 710
92.85	94.79	93.86	740 710
88.23	97.43	93.11	550 740
87.29	94.61	91.21	450 740
97.78	97.62	97.65	740 905 710
96.27	98.46	97.42	450 680 740
95.92	98.56	97.35	680 740 940
95.99	98.15	97.12	550 680 710
95.20	98.59	97.05	550 680 740
97.87	99.15	98.56	450 680 740 940
98.08	98.47	98.26	680 740 905 710
97.75	98.74	98.26	740 905 940 710
97.10	99.30	98.26	680 740 940 710
97.40	99.02	98.26	550 680 740 710
98.18	99.70	99.02	450 680 740 880 940
98.41	99.16	98.79	680 740 905 940 710
98.50	99.00	98.79	450 550 680 740 905
97.41	99.72	98.64	550 680 740 940 710
97.71	99.44	98.64	550 680 740 880 710
98.85	99.45	99.17	450 550 680 740 905 710
98.38	99.72	99.09	550 680 740 940 710 NF
98.40	99.72	99.09	550 680 740 905 940 710
98.38	99.58	99.02	550 680 740 880 710 NF
98.50	99.30	98.94	450 550 680 740 940 710
99.01	99.44	99.24	450 550 680 740 905 940 710
98.85	99.44	99.17	450 550 680 740 905 710 NF
98.35	99.72	99.09	550 680 740 880 940 710 NF
98.55	99.59	99.09	550 680 740 880 905 940 710
98.66	99.29	99.02	450 550 680 740 880 905 940
99.01	99.45	99.24	450 550 680 740 880 905 940 710
98.85	99.43	99.17	450 550 680 740 905 940 710 NF
98.52	99.57	99.09	450 550 680 740 880 940 710 NF
98.70	99.29	99.02	450 550 680 740 880 905 710 NF
98.40	99.44	98.94	550 680 740 880 905 940 710 NF
98.85	99.44	99.17	450 550 680 740 880 905 940 710 NF

Table B.5. Classification accuracy of filter combination models using available images on Honeycrisp (multiple-class scheme)

Normal	Bitter pit	Black rot	Decay	Soft scald	Total	Filter Combinations
86.21	79.21	98.17	95.47	63.10	84.89	740
78.04	85.73	98.17	93.60	59.34	81.33	710
79.74	76.70	85.71	87.48	73.83	80.44	680
63.83	39.23	87.96	72.01	39.66	61.67	905
65.53	52.07	44.01	84.77	52.75	61.00	450
95.15	96.42	98.89	100.00	96.19	96.67	680 710
94.76	96.91	97.89	100.00	95.92	96.56	680 740
95.05	97.14	98.89	100.00	93.51	96.44	740 710
91.49	91.50	98.89	97.57	88.66	93.11	740 NF
87.89	92.67	98.89	96.79	95.74	92.44	550 740
97.67	98.68	98.89	100.00	97.35	98.33	680 740 710
96.79	97.68	97.89	100.00	99.09	98.00	680 740 NF
96.35	100.00	97.89	99.17	96.63	97.67	680 740 940
96.09	97.19	98.89	99.29	99.29	97.56	550 740 710
96.23	96.91	97.89	100.00	99.29	97.56	450 680 740
98.99	99.44	100.00	100.00	98.26	99.22	680 740 940 710
97.92	98.40	100.00	100.00	98.26	98.67	680 740 905 710
98.65	97.07	98.89	100.00	98.26	98.67	680 740 880 710
97.97	98.12	97.89	100.00	100.00	98.56	450 680 740 880
98.49	98.44	97.89	99.17	97.35	98.44	680 740 940 NF
99.02	99.44	98.89	100.00	99.09	99.22	680 740 940 710 NF
98.49	100.00	100.00	100.00	99.09	99.22	680 740 880 940 710
98.81	99.23	100.00	99.33	99.29	99.11	450 680 740 940 710
98.21	98.45	100.00	100.00	100.00	99.00	550 680 740 940 710
99.01	98.68	99.00	100.00	98.26	99.00	450 680 740 940 NF
99.31	100.00	100.00	100.00	99.09	99.56	680 740 880 940 710 NF
98.65	99.23	100.00	99.29	100.00	99.22	450 550 680 740 940 710
98.42	100.00	100.00	99.29	100.00	99.22	450 550 680 740 905 710
98.75	98.52	99.00	100.00	100.00	99.11	550 680 740 940 710 NF
98.46	99.29	98.89	100.00	100.00	99.11	450 680 740 905 940 710
98.63	99.23	100.00	99.29	100.00	99.22	450 550 680 740 940 710 NF
98.37	100.00	100.00	99.29	100.00	99.22	450 550 680 740 880 940 710
98.81	99.44	100.00	99.33	99.29	99.11	450 680 740 880 940 710 NF
98.46	99.29	98.89	100.00	100.00	99.11	450 680 740 880 905 940 710
98.91	98.73	98.89	99.29	100.00	99.11	450 550 740 905 940 710 NF
98.64	100.00	99.00	99.29	100.00	99.22	450 550 680 740 880 940 710 NF
98.42	99.44	98.89	100.00	100.00	99.11	450 680 740 880 905 940 710 NF
98.61	98.45	98.89	99.29	100.00	99.00	450 550 740 880 905 940 710 NF
98.65	100.00	97.89	98.45	100.00	99.00	450 550 680 740 880 905 940 NF
98.68	99.29	98.89	98.45	100.00	99.00	450 550 680 740 880 905 940 710
98.68	99.29	98.89	98.45	100.00	99.00	450 550 680 740 880 905 940 710 NF

Table B.6. Classification accuracy of filter combination models using available images on combined variety (multiple-class scheme)

Normal	Bitter pit	Black rot	Decay	Soft scald	Superficial scald	Total	Filter Combinations
79.53	74.51	97.42	93.06	49.40	64.18	76.97	740
73.29	79.40	97.42	92.05	48.11	52.02	72.27	710
73.41	74.17	86.14	88.87	54.32	60.91	72.05	680
60.38	45.65	34.83	84.08	36.87	41.06	53.71	450
58.20	33.55	87.38	71.70	23.36	35.61	53.03	905
93.18	94.56	98.42	100.00	96.10	92.19	94.55	680 740
92.04	93.75	99.09	100.00	94.75	93.53	94.02	680 710
92.85	87.88	99.09	98.89	90.50	87.54	92.50	740 710
88.23	87.36	99.09	98.82	92.30	91.11	91.06	550 740
87.29	86.76	99.09	96.76	91.77	87.55	89.77	450 740
96.27	97.95	98.42	100.00	99.44	96.88	97.27	450 680 740
97.78	96.69	99.09	100.00	92.04	95.83	97.12	740 905 710
95.92	99.17	98.42	100.00	97.46	97.25	97.12	680 740 940
96.46	96.99	100.00	100.00	98.44	94.49	96.97	450 680 710
95.99	94.53	100.00	100.00	99.44	96.06	96.89	550 680 710
97.87	97.95	98.42	100.00	99.44	99.12	98.41	450 680 740 940
98.08	98.52	99.09	100.00	98.02	96.85	98.18	680 740 905 710
97.93	97.95	100.00	100.00	99.44	97.34	98.18	450 680 740 710
97.75	97.68	99.09	100.00	99.00	97.13	98.11	740 905 940 710
97.10	99.29	99.09	100.00	98.73	98.65	98.11	680 740 940 710
98.18	100.00	98.42	100.00	99.44	99.60	98.86	450 680 740 880 940
98.41	98.52	99.09	100.00	100.00	97.47	98.64	680 740 905 940 710
98.43	99.23	100.00	100.00	99.44	97.22	98.64	450 680 740 905 710
98.50	97.74	98.42	100.00	100.00	98.15	98.64	450 550 680 740 905
98.34	97.95	99.33	100.00	99.44	98.51	98.56	450 680 740 940 NF
98.85	99.23	100.00	100.00	99.44	98.83	99.09	450 550 680 740 905 710
98.40	99.23	99.09	100.00	100.00	99.26	98.94	550 680 740 905 940 710
98.72	99.17	99.09	100.00	99.44	98.10	98.86	680 740 880 905 940 710
98.38	100.00	98.42	100.00	99.44	99.26	98.86	550 680 740 940 710 NF
98.50	99.38	99.33	100.00	99.44	98.59	98.86	450 550 680 740 940 710
98.85	99.17	100.00	100.00	99.44	98.91	99.09	450 550 680 740 905 710 NF
99.01	99.23	98.42	100.00	99.44	99.18	99.09	450 550 680 740 905 940 710
98.55	99.23	99.09	100.00	100.00	99.31	99.02	550 680 740 880 905 940 710
98.66	99.23	99.33	100.00	99.44	98.78	98.94	450 550 680 740 880 905 940
98.25	100.00	99.09	100.00	100.00	99.26	98.94	550 680 740 905 940 710 NF
98.85	100.00	98.42	100.00	99.44	99.26	99.09	450 550 680 740 905 940 710 NF
99.01	99.23	99.33	100.00	99.44	98.83	99.09	450 550 680 740 880 905 940 710
98.52	100.00	99.33	100.00	99.44	99.26	99.02	450 550 680 740 880 940 710 NF
98.70	99.17	100.00	100.00	99.44	98.91	99.02	450 550 680 740 880 905 710 NF
98.40	100.00	99.09	100.00	100.00	98.91	98.94	550 680 740 880 905 940 710 NF
98.85	99.23	99.33	100.00	99.44	98.91	99.02	450 550 680 740 880 905 940 710 NF

APPENDIX C. Classification accuracy of filter combination models using UV-induced fluorescence (FUV) images.

Table C.1. Classification accuracy of filter combination models using UV-induced fluorescence (FUV) images on Honeycrisp (2-class scheme)

Normal	Disorder	Total	Filter Combinations					
72.12	76.13	74.56	740					
57.77	70.18	65.00	550					
61.26	66.53	64.56	710					
48.16	65.96	58.33	450					
51.08	61.83	57.22	905					
76.56	83.38	80.56	740	905				
75.10	83.33	79.89	740	710				
77.91	80.36	79.33	550	740				
73.44	80.50	77.78	450	740				
73.50	80.56	77.44	680	740				
91.58	94.26	93.00	680	740	710			
85.67	91.50	89.00	550	740	710			
84.48	90.63	88.00	450	680	740			
80.99	90.71	86.56	550	680	740			
83.18	89.26	86.44	680	740	905			
93.88	97.05	95.67	450	680	740	710		
89.85	97.02	93.89	550	680	740	710		
91.42	95.08	93.44	680	740	905	710		
88.89	95.01	92.33	450	680	740	905		
89.59	93.95	92.00	450	740	905	710		
94.74	98.25	96.67	450	680	740	905	710	
94.17	97.98	96.33	550	680	740	905	710	
91.71	97.12	94.78	450	550	740	905	710	
91.64	96.99	94.67	450	550	680	740	710	
87.38	96.55	92.56	450	550	680	740	905	
94.26	98.61	96.67	450	550	680	740	905	710

Table C.2. Classification accuracy of filter combination models using UV-induced fluorescence (FUV) images on Redcort (2-class scheme)

Normal	Disorder	Total	Filter Combinations					
61.32	64.66	62.40	680					
61.83	56.06	59.60	740					
57.17	59.16	58.80	550					
52.45	56.72	54.00	710					
51.88	53.23	53.20	450					
74.74	81.80	78.40	550	680				
78.56	76.55	76.80	450	550				
76.17	76.17	76.40	450	680				
75.59	75.28	75.60	740	710				
71.27	75.04	73.60	680	905				
88.20	93.73	91.20	450	550	680			
80.39	85.20	83.60	450	550	740			
81.21	84.85	82.80	450	740	710			
82.65	81.65	82.40	740	905	710			
76.39	84.66	80.80	450	680	740			
91.49	96.86	94.00	450	550	680	905		
91.25	95.03	93.60	450	550	740	905		
89.61	95.09	92.80	450	550	680	710		
87.52	96.45	92.40	450	550	680	740		
87.25	94.34	91.20	450	550	740	710		
93.68	95.40	94.80	450	550	740	905	710	
91.12	95.45	93.60	450	550	680	740	905	
89.78	95.68	93.20	450	550	680	740	710	
93.54	92.25	93.20	450	550	680	905	710	
90.96	93.50	92.80	450	680	740	905	710	
92.50	94.62	94.00	450	550	680	740	905	710

Table C.3. Classification accuracy of filter combination models using UV-induced fluorescence (FUV) images on Red Delicious (2-class scheme)

Normal	Disorder	Total	Filter Combinations					
94.02	87.06	91.18	680					
80.16	86.31	81.76	740					
70.70	63.29	65.88	710					
65.59	53.81	61.76	550					
65.27	51.27	59.41	450					
97.09	97.74	97.06	450	680				
96.84	94.60	95.88	550	680				
96.84	93.81	95.29	680	905				
93.84	95.24	94.71	740	710				
95.36	92.50	93.53	680	710				
99.00	100.00	99.41	740	905	710			
98.09	100.00	98.82	550	680	905			
97.75	100.00	98.82	450	550	680			
99.09	97.50	98.24	680	905	710			
98.09	99.17	98.24	550	680	710			
99.00	100.00	99.41	680	740	905	710		
98.75	99.17	98.82	450	550	680	905		
98.00	98.57	98.24	550	740	905	710		
98.00	99.17	98.24	450	740	905	710		
96.75	100.00	98.24	450	550	680	710		
99.00	100.00	99.41	550	680	740	905	710	
99.00	100.00	99.41	450	550	680	905	710	
99.00	100.00	99.41	450	550	680	740	905	
99.00	99.17	98.82	450	680	740	905	710	
99.00	98.57	98.82	450	550	740	905	710	
99.00	100.00	99.41	450	550	680	740	905	710

Table C.4. Classification accuracy of filter combination models using UV-induced fluorescence (FUV) images on combined variety (2-class scheme)

Normal	Disorder	Total	Filter Combinations					
61.81	67.53	64.85	740					
54.76	63.30	59.39	680					
55.03	62.34	58.86	710					
55.98	56.11	56.21	550					
51.48	58.77	55.38	905					
75.24	74.80	75.08	550	740				
69.80	76.98	73.64	740	710				
70.67	74.35	72.65	450	740				
67.95	73.74	71.14	680	740				
66.96	74.82	71.14	740	905				
85.55	89.87	87.80	680	740	710			
80.72	86.60	83.86	550	740	710			
78.73	85.50	82.42	450	680	740			
77.42	84.80	81.36	550	680	740			
81.05	81.57	81.29	740	905	710			
87.80	92.79	90.45	450	680	740	710		
86.53	92.91	89.92	550	680	740	710		
88.12	91.56	89.92	680	740	905	710		
85.72	93.00	89.70	450	680	740	905		
85.94	92.79	89.62	450	550	740	710		
92.66	95.91	94.39	450	680	740	905	710	
90.94	96.33	93.86	450	550	680	740	710	
90.54	95.17	93.03	550	680	740	905	710	
88.74	95.52	92.35	450	550	740	905	710	
87.77	95.80	92.05	450	550	680	740	905	
93.00	97.77	95.53	450	550	680	740	905	710

Table C.5. Classification accuracy of filter combination models using UV-induced fluorescence (FUV) images on Honeycrisp (multiple-class scheme)

Normal	Bitter pit	Black rot	Decay	Soft scald	Total	Filter Combinations
72.12	44.68	97.34	22.43	25.49	58.33	740
61.26	24.11	97.34	26.80	24.65	51.00	710
51.08	15.90	71.49	27.81	14.42	40.78	905
57.77	9.42	32.59	29.27	36.35	40.56	550
49.45	32.65	29.36	15.93	46.41	39.11	680
75.10	73.29	97.34	58.27	50.25	71.89	740 710
73.50	59.72	96.46	42.79	79.30	71.33	680 740
73.44	58.51	97.17	47.37	39.07	66.67	450 740
77.91	46.10	96.75	51.09	36.87	66.56	550 740
67.83	56.00	93.62	43.34	63.32	66.00	680 710
91.58	83.12	98.17	78.57	90.55	89.44	680 740 710
85.67	82.57	98.17	83.92	76.81	85.67	550 740 710
84.48	79.52	97.89	78.36	89.07	85.44	450 680 740
82.60	89.07	97.17	78.70	72.47	83.44	450 740 710
80.99	78.86	97.17	72.53	90.31	83.11	550 680 740
93.88	92.34	98.89	95.54	93.66	94.56	450 680 740 710
89.85	92.95	98.17	91.73	94.17	92.44	550 680 740 710
88.89	87.85	97.89	86.48	93.79	90.33	450 680 740 905
91.42	85.45	98.17	82.21	89.48	90.00	680 740 905 710
86.92	89.14	98.17	92.25	88.97	89.89	450 550 740 710
94.74	93.98	100.00	94.51	96.84	95.56	450 680 740 905 710
94.17	94.03	98.17	94.10	96.84	95.11	550 680 740 905 710
91.64	94.11	98.89	95.30	96.16	94.22	450 550 680 740 710
91.71	90.49	100.00	93.71	91.74	93.11	450 550 740 905 710
87.38	88.75	97.89	92.07	98.50	91.56	450 550 680 740 905
94.26	95.90	100.00	95.97	99.41	96.22	450 550 680 740 905 710

Table C.6. Classification accuracy of filter combination models using UV-induced fluorescence (FUV) images on combined variety (multiple-class scheme)

Normal	Bitter pit	Black rot	Decay	Soft scald	Super-ficial scald	Total	Filter Combinations
61.81	30.60	95.61	21.06	13.79	18.21	46.82	740
55.03	19.21	97.42	27.14	12.78	18.84	43.41	710
54.76	15.13	28.38	23.44	29.26	24.84	38.48	680
55.98	14.45	31.80	18.40	15.43	26.37	37.5	550
51.48	8.79	71.92	19.05	11.00	17.09	36.89	905
69.80	55.76	95.85	58.89	46.56	53.05	65.08	740 710
70.67	57.47	96.76	38.62	33.37	41.27	60.91	450 740
67.95	46.44	96.52	37.40	67.42	34.36	60.53	680 740
75.24	39.26	96.52	35.58	30.22	33.21	59.39	550 740
66.15	36.82	96.76	43.37	36.95	37.00	56.82	450 710
85.55	70.09	98.42	74.73	82.90	66.66	80.98	680 740 710
80.72	73.95	97.42	75.59	70.32	65.30	77.95	550 740 710
79.66	83.48	97.76	73.74	67.70	65.93	77.88	450 740 710
78.73	75.84	98.42	65.86	86.23	60.30	77.12	450 680 740
77.78	76.11	97.67	71.33	77.37	60.22	76.14	450 680 710
87.80	91.06	99.33	95.13	93.50	79.40	89.09	450 680 740 710
85.94	87.77	97.76	93.07	87.80	84.88	87.8	450 550 740 710
86.53	82.17	98.42	87.08	91.73	75.98	86.21	550 680 740 710
83.61	84.03	98.67	87.82	87.88	85.10	85.91	450 550 680 710
85.72	82.58	99.09	81.32	89.30	78.42	85.38	450 680 740 905
90.94	92.23	98.42	97.45	94.29	93.51	93.11	450 550 680 740 710
92.66	90.64	100.00	90.55	95.64	86.33	92.12	450 680 740 905 710
90.54	82.85	98.42	95.91	95.03	85.15	90.45	550 680 740 905 710
88.74	89.57	98.42	94.61	89.48	87.42	90.08	450 550 740 905 710
87.77	88.08	99.09	89.01	96.92	85.34	89.55	450 550 680 740 905
93.00	92.91	100.00	94.08	98.19	91.92	94.24	450 550 680 740 905 710

APPENDIX D. Classification accuracy of filter combination models using reflectance (R) images.

Table D.1. Classification accuracy of filter combination models using reflectance (R) images on Honeycrisp (2-class scheme)

Normal	Disorder	Total	Filter Combinations
60.12	69.26	65.44	550
58.71	65.24	62.22	880
57.17	66.09	62.00	710
58.81	64.27	61.89	905
53.90	67.38	61.56	450
79.79	83.57	81.89	905 710
78.79	83.20	81.22	740 710
77.53	81.44	79.67	880 710
76.59	81.98	79.67	740 905
78.13	79.57	78.89	740 940
90.86	93.72	92.44	740 905 NF
90.58	93.03	91.89	740 905 710
90.80	92.01	91.44	740 880 710
89.29	92.39	91.00	740 710 NF
87.78	92.88	90.67	550 905 940
94.58	96.48	95.56	740 905 710 NF
93.44	96.44	95.11	740 880 710 NF
93.66	95.88	94.89	740 905 940 710
91.92	97.11	94.78	550 680 740 NF
92.77	95.61	94.56	680 740 710 NF
96.75	97.29	97.00	740 880 905 940 710
95.64	97.88	96.78	550 680 740 905 NF
95.85	97.33	96.56	550 680 740 880 NF
95.57	97.03	96.44	680 740 880 940 NF
96.17	96.51	96.33	740 880 940 710 NF
95.94	98.80	97.56	680 740 880 905 940 710
96.53	98.43	97.56	450 550 680 740 905 710
97.08	97.80	97.44	740 880 905 940 710 NF
96.51	98.28	97.44	450 550 680 740 905 NF
96.50	98.07	97.33	450 550 680 740 880 NF
97.02	98.99	98.11	450 550 680 740 905 710 NF
96.70	99.20	98.11	450 550 680 740 905 940 710
95.97	99.22	97.78	550 680 740 880 905 940 710
96.52	98.82	97.78	450 550 680 740 880 940 NF
96.26	98.65	97.56	450 740 880 905 940 710 NF
96.44	99.20	98.00	450 550 680 740 905 940 710 NF
96.76	99.04	98.00	450 550 680 740 880 940 710 NF
96.81	98.82	97.89	450 550 740 880 905 940 710 NF
96.02	98.83	97.56	450 550 680 740 880 905 940 NF
95.41	99.04	97.44	550 680 740 880 905 940 710 NF
96.23	99.00	97.78	450 550 680 740 880 905 940 710 NF

Table D.2. Classification accuracy of filter combination models using reflectance (R) images on Redcort (2-class scheme)

Normal	Disorder	Total	Filter Combinations
69.48	65.48	66.40	710
62.11	60.57	60.80	905
57.42	60.76	60.40	880
58.64	61.17	59.60	NF
56.00	56.77	56.80	940
95.19	93.00	94.40	905 710
88.44	90.69	90.00	905 NF
86.21	88.21	88.40	740 940
87.48	87.17	88.00	740 905
88.97	86.12	88.00	740 880
97.98	95.66	97.20	740 905 NF
96.89	95.03	96.00	740 905 710
94.24	95.30	95.20	680 905 710
92.20	96.82	95.20	680 740 880
94.34	94.44	94.80	905 710 NF
98.12	97.20	97.60	450 680 905 710
99.29	94.59	97.20	450 740 905 710
96.20	96.70	96.80	680 740 905 NF
96.48	96.73	96.80	680 740 880 905
93.93	99.09	96.80	550 680 905 710
98.62	99.17	98.80	550 680 740 880 905
98.62	98.45	98.40	550 680 740 905 940
97.90	99.00	98.40	450 680 740 905 710
97.25	98.09	98.00	680 740 880 905 710
96.67	98.40	97.60	550 680 740 905 NF
98.62	98.54	98.40	550 680 740 880 905 NF
98.57	98.33	98.40	550 680 740 880 905 940
97.37	99.17	98.40	450 550 680 740 880 905
98.56	97.17	98.00	450 680 740 905 940 710
97.12	99.17	98.00	450 550 680 740 905 NF
98.04	96.88	97.60	550 680 740 880 905 940 NF
97.85	97.83	97.60	450 550 680 740 880 905 NF
98.62	96.92	97.60	550 680 740 880 905 710 NF
97.90	97.33	97.60	550 680 740 880 905 940 710
98.62	95.85	97.20	450 550 680 740 905 940 710
97.79	96.62	97.20	550 680 740 880 905 940 710 NF
95.87	95.92	96.00	450 550 680 740 880 905 710 NF
93.02	96.62	95.20	450 550 680 880 905 940 710 NF
95.80	94.94	95.20	450 550 680 740 905 940 710 NF
94.68	95.24	95.20	450 550 680 740 880 905 940 NF
95.87	94.79	95.60	450 550 680 740 880 905 940 710 NF

Table D.3. Classification accuracy of filter combination models using reflectance (R) images on Red Delicious (2-class scheme)

Normal	Disorder	Total	Filter Combinations
62.05	60.95	62.94	550
64.50	58.49	61.76	740
65.77	55.75	60.59	450
61.89	53.69	58.24	905
57.00	58.21	57.65	710
96.00	96.67	96.47	740 905
94.09	95.56	94.71	740 940
90.11	92.18	91.18	740 880
87.02	82.06	85.88	905 NF
84.86	81.75	84.71	880 NF
97.00	98.33	98.24	740 905 NF
97.00	96.94	97.06	740 905 710
95.09	97.22	96.47	550 880 NF
95.09	97.74	96.47	740 905 940
95.00	97.74	96.47	680 740 905
97.00	98.89	98.24	740 905 710 NF
97.09	99.17	98.24	740 905 940 710
97.00	98.89	98.24	680 740 905 NF
96.00	98.89	97.65	740 880 940 NF
95.00	100.00	97.65	740 880 905 NF
98.00	100.00	99.41	550 680 740 905 710
99.00	99.17	98.82	740 880 905 940 710
99.00	98.89	98.82	680 740 880 905 710
96.09	100.00	98.24	550 740 905 710 NF
97.00	98.89	98.24	550 680 740 905 NF
99.00	98.89	98.82	680 740 880 905 940 710
98.00	98.89	98.82	550 680 740 880 905 710
96.09	100.00	98.24	740 880 905 940 710 NF
96.09	100.00	98.24	550 680 740 905 710 NF
97.00	98.89	98.24	450 680 740 880 905 710
97.00	97.46	97.65	680 740 880 905 940 710 NF
96.00	98.89	97.65	550 680 740 880 905 710 NF
95.75	98.89	97.65	450 740 880 905 940 710 NF
96.00	98.89	97.65	450 680 740 880 905 710 NF
96.09	97.46	97.06	550 740 880 905 940 710 NF
97.00	98.89	98.24	450 680 740 880 905 940 710 NF
97.00	97.46	97.65	550 680 740 880 905 940 710 NF
98.09	96.63	97.06	450 550 740 880 905 940 710 NF
96.09	97.22	96.47	450 550 680 740 880 905 940 710
95.09	95.56	95.29	450 550 680 740 880 940 710 NF
96.09	96.63	96.47	450 550 680 740 880 905 940 710 NF

Table D.4. Classification accuracy of filter combination models using reflectance (R) images on combined variety (2-class scheme)

Normal	Disorder	Total	Filter Combinations
59.55	61.51	60.61	740
53.85	62.50	58.41	710
54.12	60.66	57.50	NF
50.60	62.44	56.97	880
55.21	58.19	56.67	550
79.42	82.56	81.06	905 710
75.67	80.75	78.41	740 905
75.76	79.44	77.58	880 710
74.34	78.69	76.74	740 880
73.27	77.08	75.30	905 NF
89.79	91.57	90.76	740 905 NF
88.25	91.02	89.77	740 905 710
86.20	90.65	88.56	740 880 NF
86.08	88.89	87.58	905 710 NF
84.98	89.71	87.58	740 880 710
91.71	95.22	93.56	550 740 905 NF
91.51	94.14	92.95	740 905 940 710
91.27	94.21	92.88	740 905 710 NF
91.39	94.16	92.88	550 740 905 710
91.82	92.94	92.42	740 905 940 NF
93.97	95.47	94.77	450 680 740 905 NF
92.97	96.35	94.77	550 680 740 905 NF
92.36	96.35	94.47	550 680 740 940 NF
92.86	95.74	94.39	550 740 905 710 NF
92.73	95.89	94.39	550 740 880 940 710
95.62	97.30	96.52	450 550 680 740 905 710
95.29	97.32	96.36	450 550 680 740 905 NF
94.98	97.19	96.14	450 550 680 740 880 NF
94.16	97.44	95.91	450 550 680 740 940 710
95.51	96.08	95.76	450 680 740 905 940 NF
95.82	97.87	96.89	450 550 680 740 905 940 710
95.95	97.46	96.74	450 550 680 740 905 710 NF
95.79	97.44	96.67	450 550 680 740 880 905 NF
95.48	97.45	96.52	450 550 680 740 905 940 NF
95.76	97.06	96.44	450 550 740 880 905 940 710
96.14	97.74	96.97	450 550 680 740 880 905 710 NF
95.96	97.75	96.89	450 550 680 740 905 940 710 NF
96.12	97.44	96.82	450 550 680 740 880 905 940 NF
95.52	97.88	96.74	450 550 680 740 880 905 940 710
94.73	97.76	96.29	550 680 740 880 905 940 710 NF
96.14	97.87	97.05	450 550 680 740 880 905 940 710 NF

Table D.5. Classification accuracy of filter combination models using reflectance (R) images on Honeycrisp (multiple-class scheme)

Normal	Bitter pit	Black rot	Decay	Soft scald	Total	Filter Combinations
57.17	38.00	91.07	31.32	33.31	52.33	710
55.79	37.68	91.83	29.66	33.77	51.22	740
58.81	18.66	68.04	53.72	37.92	50.89	905
58.71	30.79	59.49	50.76	32.53	49.56	880
60.12	44.39	38.13	42.20	29.75	48.11	550
79.79	94.20	98.06	72.68	67.57	81.56	905 710
78.13	80.46	98.89	74.10	65.09	78.89	740 940
76.59	84.36	98.06	86.18	52.81	78.78	740 905
74.06	75.10	93.99	84.12	70.87	77.78	550 940
73.86	70.56	98.89	87.67	63.22	77.56	680 940
90.86	94.08	97.47	91.50	88.08	91.78	740 905 NF
90.58	97.91	98.89	81.56	93.51	91.78	740 905 710
90.80	94.27	98.30	81.56	85.27	90.33	740 880 710
87.78	88.73	95.11	89.02	96.29	90.33	550 905 940
89.17	99.44	98.89	77.58	88.48	90.22	740 940 710
94.58	98.68	98.89	91.58	94.65	95.22	740 905 710 NF
93.44	99.44	98.89	90.81	95.47	95.00	740 880 710 NF
93.66	96.63	98.89	89.82	97.25	94.67	740 905 940 710
92.77	98.06	97.89	88.69	96.31	94.33	680 740 710 NF
93.72	99.44	98.89	89.68	91.91	94.33	680 740 940 NF
96.75	98.52	98.89	94.54	97.01	97.00	740 880 905 940 710
95.64	99.44	97.30	93.40	99.29	96.44	550 680 740 905 NF
95.57	97.89	98.30	92.23	98.45	96.22	680 740 880 940 NF
96.17	99.44	98.89	91.61	96.06	96.22	740 880 940 710 NF
95.06	97.34	98.89	92.86	100.00	96.22	550 740 905 940 710
95.94	99.29	98.89	96.83	100.00	97.56	680 740 880 905 940 710
97.08	98.52	98.89	95.29	98.18	97.44	740 880 905 940 710 NF
96.53	98.68	98.89	95.12	99.29	97.33	450 550 680 740 905 710
96.18	99.44	98.89	93.57	99.29	97.11	680 740 880 940 710 NF
95.75	98.52	98.89	95.12	100.00	97.11	550 740 880 905 940 710
95.97	100.00	98.89	97.83	100.00	97.78	550 680 740 880 905 940 710
97.02	99.44	98.30	96.79	99.29	97.78	450 550 680 740 905 710 NF
96.70	99.44	97.89	97.79	99.29	97.78	450 550 680 740 905 940 710
96.52	99.23	99.41	96.40	100.00	97.67	450 550 680 740 880 940 NF
96.26	98.52	98.30	96.95	100.00	97.44	450 740 880 905 940 710 NF
96.76	98.46	100.00	97.79	100.00	98.00	450 550 680 740 880 940 710 NF
96.81	98.52	98.30	97.79	100.00	97.78	450 550 740 880 905 940 710 NF
96.44	99.44	97.30	97.79	99.29	97.56	450 550 680 740 905 940 710 NF
95.41	100.00	98.89	97.17	100.00	97.44	550 680 740 880 905 940 710 NF
96.02	98.52	98.89	97.12	100.00	97.44	450 550 680 740 880 905 940 NF
96.23	98.52	98.89	97.79	100.00	97.67	450 550 680 740 880 905 940 710 NF

Table D.6. Classification accuracy of filter combination models using reflectance (R) images on combined variety (multiple-class scheme)

Normal	Bitter pit	Black rot	Decay	Soft scald	Superficial scald	Total	Filter Combinations
59.55	31.72	91.03	16.17	21.88	22.80	46.44	740
53.85	29.53	91.79	19.75	23.83	22.90	44.32	710
51.70	24.83	47.48	51.53	31.56	28.38	43.26	940
50.60	20.69	62.32	55.61	20.64	29.05	43.11	880
50.80	14.12	64.79	56.23	23.13	26.56	42.35	905
79.42	85.52	98.59	76.64	53.26	52.04	74.85	905 710
75.67	82.28	98.59	88.46	48.06	53.17	73.33	740 905
75.76	76.49	98.59	82.58	36.43	49.82	70.76	880 710
73.27	57.34	98.59	81.83	47.74	59.18	70.15	905NF
70.16	61.57	92.94	81.86	66.11	52.00	69.7	550 940
89.79	89.97	97.68	87.21	72.17	77.72	86.67	740 905NF
88.25	94.75	99.09	83.90	79.02	73.95	86.14	740 905 710
86.08	91.39	97.76	87.76	68.97	82.33	85.53	905 710NF
85.30	85.36	98.59	86.81	86.14	71.52	84.47	905 940 710
83.52	84.61	99.09	85.54	83.05	78.13	84.32	905 940NF
91.51	98.45	99.09	91.95	97.26	83.34	92.2	740 905 940 710
91.27	97.23	99.09	89.77	89.88	90.31	92.12	740 905 710NF
91.71	94.80	98.18	88.79	92.80	89.34	92.05	550 740 905NF
91.82	96.79	98.18	90.48	96.37	83.19	91.82	740 905 940NF
91.39	96.28	99.09	88.97	90.61	84.61	91.36	550 740 905 710
92.97	99.29	97.52	92.29	97.22	94.16	94.47	550 680 740 905NF
93.97	97.68	98.18	91.22	94.26	93.69	94.32	450 680 740 905NF
92.36	98.66	98.18	92.29	97.50	93.51	94.09	550 680 740 940NF
92.86	97.74	98.42	90.70	96.46	91.34	93.79	550 740 905 710NF
93.25	96.97	99.09	94.10	98.15	87.01	93.79	450 740 905 940 710
95.29	97.74	98.18	94.29	97.22	95.36	95.83	450 550 680 740 905NF
95.62	95.38	99.09	95.17	97.28	93.24	95.76	450 550 680 740 905 710
94.03	100.00	99.09	93.39	98.06	95.18	95.61	550 680 740 880 905 710
95.51	98.45	98.18	94.57	98.05	91.82	95.45	450 680 740 905 940NF
94.16	96.61	100.00	93.83	98.06	95.42	95.45	450 550 680 740 940 710
95.82	99.29	98.42	95.17	99.44	96.13	96.74	450 550 680 740 905 940 710
95.95	97.74	98.18	96.28	97.84	95.91	96.52	450 550 680 740 905 710NF
95.79	97.62	100.00	94.88	98.06	96.44	96.52	450 550 680 740 880 905NF
95.76	98.45	99.09	95.72	99.44	94.34	96.44	450 550 740 880 905 940 710
95.48	99.29	98.18	95.40	99.44	94.76	96.36	450 550 680 740 905 940NF
96.14	97.62	99.09	96.94	98.06	97.06	96.89	450 550 680 740 880 905 710NF
95.96	99.29	98.18	96.28	99.44	95.16	96.74	450 550 680 740 905 940 710NF
96.12	98.45	99.09	95.40	99.44	95.39	96.74	450 550 680 740 880 905 940NF
95.52	98.45	99.09	95.83	99.44	96.81	96.74	450 550 680 740 880 905 940 710
95.64	98.45	98.18	95.72	99.44	94.60	96.29	450 550 740 880 905 940 710NF
96.14	99.17	99.09	96.94	99.44	96.01	97.05	450 550 680 740 880 905 940 710 NF

APPENDIX E. Classification accuracy of feature combination models

Table E.1. Classification accuracy of feature combination models on Honeycrisp (2-class scheme)

Normal	Disorder	Total	Feature combinations
80.63	74.21	77.42	FUV740
58.05	78.65	68.35	R550
54.54	81.81	68.17	FUV550
70.14	64.92	67.53	FVIS740
71.11	63.52	67.31	R940
62.77	71.59	67.18	R450
69.43	64.72	67.08	FUV710
68.33	64.50	66.41	R880
66.20	66.02	66.11	FVIS710
68.62	63.30	65.96	R905
65.71	63.03	64.37	FVIS680
62.16	64.19	63.17	RNF
67.21	58.52	62.86	R680
66.63	58.94	62.79	R710
65.16	57.50	61.33	R740
49.52	69.60	59.56	FUV450
62.82	55.14	58.98	FUV905
61.74	55.23	58.48	FUV680
80.36	84.72	82.89	FUV740 FVIS710
79.79	83.57	81.89	R905 R710
78.79	83.20	81.22	R740 R710
77.27	83.53	80.78	FUV740 FVIS740
78.25	82.39	80.67	FVIS710 R940
91.58	94.26	93.00	FUV680 FUV740 FUV710
90.86	93.72	92.44	R740 R905 RNF
90.58	93.03	91.89	R740 R905 R710
90.80	92.01	91.44	R740 R880 R710
87.39	94.15	91.11	FUV680 FUV740 FVIS740
95.17	97.89	96.56	FUV680 FUV740 FUV710 FVIS740
95.50	97.09	96.33	FVIS710 R740 R905 R940
93.46	97.41	95.78	FVIS710 R905 R940 RNF
93.39	97.47	95.67	FUV680 FUV740 FUV710 R905
94.72	96.49	95.67	FVIS710 R740 R905 R710

Table E.2. Classification accuracy of feature combination models on Redcort (2-class scheme)

Normal	Disorder	Total	Feature combinations
67.76	59.88	63.82	R710
59.13	66.33	62.73	RNF
63.36	61.60	62.48	FUV680
60.14	64.24	62.19	R905
59.21	60.93	60.07	FUV740
57.42	61.72	59.57	R940
61.86	54.70	58.28	R880
56.17	60.17	58.17	R550
55.40	58.84	57.12	FVIS680
57.13	56.28	56.70	FVIS710
52.27	60.61	56.44	FUV550
46.15	61.40	53.77	R680
54.37	51.86	53.12	R740
50.07	52.40	51.24	FUV450
46.41	55.86	51.13	R450
46.69	54.52	50.61	FUV710
55.01	45.88	50.44	FUV905
41.74	44.58	43.16	FVIS740
95.19	93.00	94.40	R905 R710
88.44	90.69	90.00	R905 RNF
86.21	88.21	88.40	R740 R940
87.48	87.17	88.00	R740 R905
88.97	86.12	88.00	R740 R880
97.98	95.66	97.20	R740 R905 RNF
97.31	95.08	96.40	FUV680 R905 R710
95.49	96.33	96.40	FUV680 R740 R905
96.89	95.03	96.00	R740 R905 R710
94.24	95.30	95.20	R680 R905 R710
98.75	98.26	98.80	FUV680 R740 R905 RNF
98.17	98.09	98.40	FUV680 R680 R740 R880
96.87	98.29	98.00	FUV680 FVIS710 R740 R880
96.16	99.00	98.00	FUV680 FVIS740 R740 R880
95.54	99.17	97.60	FUV680 R740 R880 R905

Table E.3. Classification accuracy of feature combination models on Red Delicious (2-class scheme)

Normal	Disorder	Total	Feature combinations
94.02	96.11	95.07	FUV680
76.25	81.51	78.88	FUV740
67.27	77.58	72.43	FUV710
59.64	72.06	65.85	FVIS710
62.43	63.57	63.00	R740
57.05	67.82	62.43	FUV450
58.11	63.37	60.74	R450
52.82	64.37	58.59	R550
55.84	59.84	57.84	R710
53.07	60.60	56.83	FVIS740
48.82	63.53	56.17	R905
49.98	62.30	56.14	FUV550
62.20	48.89	55.55	FVIS680
45.07	56.63	50.85	R880
42.36	55.99	49.18	R940
44.68	53.13	48.91	FUV905
43.27	52.54	47.91	R680
43.18	47.90	45.54	RNF
97.09	97.74	97.06	FUV450 FUV680
96.00	96.67	96.47	R740 R905
96.84	94.60	95.88	FUV550 FUV680
95.84	94.40	95.29	FUV680 R740
95.59	94.96	95.29	FUV680 FVIS680
99.00	100.00	99.41	FUV740 FUV905 FUV710
98.09	100.00	98.82	FUV550 FUV680 FUV905
97.75	100.00	98.82	FUV450 FUV550 FUV680
97.00	98.33	98.24	R740 R905 RNF
98.09	99.17	98.24	FUV680 R450 R550
100.00	99.17	99.41	FUV680 R740 R905 R710
100.00	99.17	99.41	FUV680 R680 R740 R905
100.00	99.17	99.41	FUV680 R550 R880 R905
100.00	99.17	99.41	FUV680 FVIS710 R905 R710
99.00	100.00	99.41	FUV680 FVIS710 R740 R940

Table E.4. Classification accuracy of feature combination models on combined variety (2-class scheme)

Normal	Disorder	Total	Feature combinations
81.81	68.00	74.91	FUV740
65.69	63.78	64.73	FVIS710
52.28	75.01	63.65	FUV550
67.76	58.94	63.35	R710
67.83	56.76	62.29	FUV710
66.58	57.91	62.24	FVIS740
63.04	60.38	61.71	R450
68.67	54.00	61.33	FVIS680
61.16	60.16	60.66	RNF
62.42	58.68	60.55	FUV680
65.43	54.64	60.03	R880
61.89	58.18	60.03	R740
53.87	65.53	59.70	R550
58.72	57.29	58.01	R680
63.51	51.63	57.57	R940
52.62	62.45	57.53	FUV450
63.96	50.21	57.08	R905
60.98	51.47	56.22	FUV905
79.42	82.56	81.06	R905 R710
75.67	80.75	78.41	R740 R905
75.76	79.44	77.58	R880 R710
75.77	78.65	77.35	FUV740 FVIS710
74.34	78.69	76.74	R740 R880
89.79	91.57	90.76	R740 R905 RNF
88.25	91.02	89.77	R740 R905 R710
86.20	90.65	88.56	R740 R880 RNF
85.55	89.87	87.80	FUV680 FUV740 FUV710
86.08	88.89	87.58	R905 R710 RNF
93.66	95.60	94.70	FVIS710 R740 R905 R710
93.11	95.21	94.24	FVIS710 R740 R905 RNF
91.90	95.36	93.71	FVIS740 R740 R880 RNF
91.71	95.22	93.56	R550 R740 R905 RNF
89.92	96.49	93.41	FUV680 FUV740 FUV710 FVIS740

Table E.5. Classification accuracy of feature combination models on Honeycrisp (multiple-class scheme)

Normal	Bitter pit	Black rot	Decay	Soft scald	Total	Filter Combinations
36.28	79.43	79.88	66.15	39.02	60.15	FVIS710
57.74	53.29	97.34	53.98	26.53	57.78	FUV740
33.33	57.63	65.39	76.44	51.54	56.86	R880
30.31	55.28	90.13	60.17	46.22	56.42	R740
13.11	57.44	92.25	70.27	44.70	55.55	R710
35.98	66.86	84.64	39.34	49.18	55.20	FVIS740
40.67	61.60	44.70	77.22	50.69	54.98	R550
25.64	53.88	65.61	73.52	47.01	53.13	R905
18.89	57.69	66.30	63.16	58.90	52.99	R680
26.76	50.66	66.86	54.32	60.74	51.87	FVIS680
34.54	46.61	97.34	46.26	28.39	50.63	FUV710
32.23	52.06	55.23	63.57	49.98	50.62	R940
35.71	42.61	81.93	45.18	43.62	49.81	FUV550
36.74	42.57	78.49	52.61	22.03	46.49	RNF
31.16	41.72	21.44	86.58	50.69	46.32	R450
18.20	49.46	43.80	33.49	62.17	41.42	FUV680
21.30	23.66	82.07	34.18	20.71	36.39	FUV905
24.38	36.29	32.53	19.57	39.98	30.55	FUV450
79.79	94.20	98.06	72.68	67.57	81.56	R905 R710
78.13	80.46	98.89	74.10	65.09	78.89	R740 R940
76.59	84.36	98.06	86.18	52.81	78.78	R740 R905
78.25	77.66	87.60	90.26	58.02	78.67	FVIS710 R940
74.06	75.10	93.99	84.12	70.87	77.78	R550 R940
90.86	94.08	97.47	91.50	88.08	91.78	R740 R905 RNF
90.58	97.91	98.89	81.56	93.51	91.78	R740 R905 R710
90.80	94.27	98.30	81.56	85.27	90.33	R740 R880 R710
87.78	88.73	95.11	89.02	96.29	90.33	R550 R905 R940
89.17	99.44	98.89	77.58	88.48	90.22	R740 R940 R710
95.50	98.89	98.89	96.79	92.33	96.11	FVIS710 R740 R905 R940
95.17	95.36	98.17	97.56	95.91	96.00	FUV680 FUV740 FUV710 FVIS740
94.72	98.68	98.89	93.67	94.58	95.67	FVIS710 R740 R905 R710
93.46	99.44	98.89	96.54	92.10	95.44	FVIS710 R905 R940 RNF
93.66	98.23	98.89	95.68	94.34	95.44	FVIS740 R550 R680 R940

Table E.6. Classification accuracy of feature combination models on combined variety (multiple-class scheme)

Normal	Bitter pit	Black rot	Decay	Soft scald	Superficial scald	Total	Filter Combinations
30.22	78.43	81.73	60.82	40.96	43.31	55.91	FVIS710
22.36	61.55	85.30	42.22	46.76	50.81	51.50	FVIS740
7.86	39.86	64.95	83.59	40.92	55.31	48.75	R905
12.54	50.04	92.70	64.98	34.80	34.30	48.23	R710
39.51	48.08	95.61	54.34	26.28	24.82	48.10	FUV740
21.95	60.93	41.74	71.22	46.69	45.78	48.05	R550
9.60	54.18	67.11	76.84	36.82	42.76	47.88	R880
16.91	36.15	58.56	66.00	50.63	52.50	46.79	R940
20.43	50.72	62.79	60.46	41.65	39.21	45.87	FVIS680
11.96	53.42	64.38	66.19	41.90	33.98	45.30	R680
17.94	52.45	88.88	37.03	39.16	26.69	43.69	R740
26.07	40.65	96.52	48.35	19.20	27.26	43.01	FUV710
25.91	41.88	82.12	32.00	42.72	32.54	42.86	FUV550
13.73	32.52	21.62	97.00	44.55	37.30	41.12	R450
25.45	41.48	77.82	41.05	18.09	34.21	39.68	RNF
19.97	52.00	37.26	32.28	41.29	34.44	36.21	FUV680
14.67	17.40	80.82	35.00	16.61	31.26	32.63	FUV905
20.96	35.62	29.08	18.52	34.42	49.22	31.30	FUV450
79.42	85.52	98.59	76.64	53.26	52.04	74.85	R905 R710
75.67	82.28	98.59	88.46	48.06	53.17	73.33	R740 R905
75.76	76.49	98.59	82.58	36.43	49.82	70.76	R880 R710
73.27	57.34	98.59	81.83	47.74	59.18	70.15	R905 RNF
70.16	61.57	92.94	81.86	66.11	52.00	69.70	R550 R940
89.79	89.97	97.68	87.21	72.17	77.72	86.67	R740 R905 RNF
88.25	94.75	99.09	83.90	79.02	73.95	86.14	R740 R905 R710
86.08	91.39	97.76	87.76	68.97	82.33	85.53	R905 R710 RNF
83.77	86.39	98.42	98.68	65.27	81.19	84.70	FUV740 FUV710 FVIS740
85.30	85.36	98.59	86.81	86.14	71.52	84.47	R905 R940 R710
93.66	96.28	99.09	96.56	88.67	89.94	93.56	FVIS710 R740 R905 R710
91.51	98.45	99.09	91.95	97.26	83.34	92.20	R740 R905 R940 R710
91.27	97.23	99.09	89.77	89.88	90.31	92.12	R740 R905 R710 RNF
93.01	96.25	99.09	97.56	87.83	82.33	92.12	FVIS710 R740 R905 R940
92.64	98.45	99.09	96.49	89.05	82.04	92.05	FVIS740 R740 R905 R940

BIBLIOGRAPHY

BIBLIOGRAPHY

Abbott, J. A. 1999. Quality measurement of fruits and vegetables. *Postharvest Biology and Technology* 15: 207-225.

Abbott, J. A., Lu, R., Upchurch, B. L., and Stroshine, R. L. 1997. Technologies for nondestructive quality evaluation of fruits and vegetables. *Horticultural Reviews* 20: 1-119.

Aha, D. W. 1997. Lazy learning. *Artificial Intelligence Review* 11: 7-10.

Aleixos, N., Blasco, J., Navarron, F., and Molto, E. 2002. Multispectral inspection of citrus in real-time using machine vision and digital signal processors. *Computers and Electronics in Agriculture* 33(2): 121-137.

Aneshansley, D. J., Throop, J. A., and Upchurch, B. L. 1997. Reflectance spectra of surface defects on apples. In *Sensors for Nondestructive Testing, Measuring the Quality of Fresh Fruits and Vegetables*, pp. 143-160. NRAES, Ithaca, New York.

Back, A. D., and Trappenberg, T. P. 2001. Selecting inputs for modeling using normalized higher order statistics and independent component analysis. *IEEE Transactions on Neural Networks* 12(3): 612-617.

Beaudry, R. M., Armstrong, P. R., Song, J., and Deng, W. 1998. Non-destructive method and apparatus for detection of fruit and vegetable quality. US. Patent No. 5,822,068

Bedford, D. 2001. Honeycrisp. *Compact Fruit Tree* 34(4): 98-99.

Birth, G. S. 1976. How light interact with foods. In *Quality detection in foods* (J. J. Gaffney, ed.), pp. 6-11. American Society of Agricultural Engineers, St. Joseph, Michigan.

Bittner, D. R., and Norris, K. H. 1968. Optical properties of selected fruits vs maturity. *Transactions of the ASAE* 11(4): 534-536.

Brosnan, T., and Sun, D.-W. 2002. Inspection and grading of agricultural and food products by computer vision systems-a review. *Computers and Electronics in Agriculture* 36: 193-213.

Brown, G. K., Segerlind, L. J., and Summit, R. 1974. Near-infrared reflectance of bruised apple. *Transactions of the ASAE* 17(1): 17-19.

Chao, K., Mehl, P. M., and Chen, Y. R. 2002. Use of hyper- and multi-spectral imaging for detection of chicken skin tumors. *Applied Engineering in Agriculture* 18(1): 113-119.

Chappelle, E. W., Wood, F. M., Newcomb, W. W., and McMurtrey, J. E. 1985. Laser-induced fluorescence of green plants. 3:LIF spectral signatures of five major plant types. *Applied Optics* 24(1): 74-80.

Chen, P. 1978. Use of optical properties of food material in quality evaluation and materials sorting. *Journal of Food Process Engineering* 2: 307-322.

Codrea, M., Tyystjarvi, E., Ven, M. v., Valcke, R., and Nevalainen, O. 2002. Using fluorescence images in classification of apples. *Proceedings of the IASTED-VIIP 2nd International Conference Artificial Intelligence and Applications, Visualization, Imaging and Image Processing* (J. J. Villaneuva, ed.). Acta Press, Benalmadena, Spain.

Crowe, T. G., and Delwiche, M. J. 1996a. Real-time defect detection in fruit. I. Design concepts and development of prototype hardware. *Transactions of the ASAE* 39(6): 2299-2308.

Crowe, T. G., and Delwiche, M. J. 1996b. Real-time defect detection in fruit. II. An algorithm and performance of a prototype system. *Transactions of the ASAE* 39(6): 2309-2317.

Cunningham, P., Carney, J., and Jacob, S. 2000. Stability problems with artificial neural networks and the ensemble solution. *Artificial Intelligence in Medicine* 20: 217-225.

Davenel, A., Guizard, C., Labarre, T., and Sevila, F. 1988. Automatic detection of surface defects on fruit by using a vision system. *Journal of Agricultural Engineering Research* 41(1): 1-9.

DeEll, J. R., Kooten, O., Prange, R. K., and Murr, D. P. 1999. Applications of chlorophyll fluorescence techniques in postharvest physiology. *Horticultural Reviews* 23: 69-107.

DeEll, J. R., Prange, R. K., and Murr, D. P. 1995. Chlorophyll fluorescence as a potential indicator of controlled-atmosphere disorders in 'Marshall' McIntosh apples. *HortScience* 30(5): 1084-1085.

Duda, R. O., Hart, P. E., and Stork, D. G. 2001. *Pattern classification*. Second/Ed., New York.

Forney, C. F., Jordan, M. A., Nicholas, K., and DeEll, J. R. 2000. Volatile emissions and chlorophyll fluorescence as indicators of freezing injury in apple fruit. *HortScience* 35(7): 1283-1287.

Garson, G. D. 1991. Interpreting neural network connection weights. *AI Expert*(Apr.): 47-51.

Gat, N., Subramanian, S., Barhen, J., and Toomarian, N. 1997. Spectral imaging applications: remote sensing, environmental monitoring, medicine, military operations, factory automation and manufacturing. *Proc. SPIE* 2962: 63-77.

Glorfield, L. W. 1996. A methodology for simplification and interpretation of backpropagation-based neural network models. *Expert Systems With Applications* 10(1): 37-54.

Guyer, D., and Yang, X. 2000. Use of genetic artificial neural networks and spectral imaging for defect detection on cherries. *Computers and Electronics in Agriculture* 29(3): 179-194.

Hand, D. J. 1981. *Discrimination and classification*. John Wiley & Sons, New York.

Haykin, S. 1999. *Neural networks: a comprehensive foundation*. Second/Ed. Prentice Hall, Upper Saddle River, New Jersey.

Heinemann, P. H., Varghese, Z. A., Morrow, C. T., III, H. J. S., and Crassweller, R. M. 1995. Machine vision inspection of Golden Delicious apples. *Applied Engineering in Agriculture* 11(6): 901-906.

Herman, B. 1998. *Fluorescence Microscopy*. Second/Ed. Springer-Verlag, New York.

Ingle, M., and D'Souza, M. C. 1989. Physiological and control of superficial scald of apples: a review. *HortScience* 24(1): 28-31.

Ingle, M., and Hyde, J. F. 1968. The effect of bruising on discoloration and concentration of phenolic compounds in apple tissue. *Proceedings of the American Society for Horticultural Science* 93: 738-745.

Jolliffe, I. T. 1972. Discarding variables in a principal component analysis I:artificial data. *Applied Statistics* 21: 160-173.

Kavdir, I., and Guyer, D. E. 2002. Apple sorting using artificial neural networks and spectral imaging. *Transactions of the ASAE* 45(6): 1995-2005.

Kim, M. S., Chen, Y. R., and Mehl, P. M. 2001a. Hyperspectral reflectance and fluorescence imaging system for food quality and safety. *Transactions of the ASAE* 44(3): 721-729.

Kim, M. S., Lefcourt, A. M., Chao, K., Chen, Y. R., Kim, I., and Chan, D. E. 2002a. Multispectral detection of fecal contamination on apples based on hyperspectral imagery: Part I. application of visible and near-infrared reflectance imaging. *Transactions of the ASAE* 45(6): 2027-2037.

Kim, M. S., Lefcourt, A. M., Chao, K., Chen, Y. R., Kim, I., and Chan, D. E. 2002b. Multispectral detection of fecal contamination on apples based on hyperspectral imagery: Part II. application of hyperspectral fluorescence imaging. *Transactions of the ASAE* 45(6): 2039-2047.

Kim, M. S., McMurtrey, J. E., Mulchi, C. L., Daughtry, C. S. T., Chappelle, E. W., and Chen, Y. R. 2001b. Steady-state multispectral fluorescence imaging system for plant leaves. *Applied Optics* 40(1): 157-166.

Kittler, J. 1986. Feature selection and extraction. In *Handbook of Pattern Recognition and Image Processing* (T. Y. Young and K.-S. Fu, eds.). Academic Press, Inc., San Diego, California.

Krzanowski, W. J. 1987. Selection of variables to preserve multivariate data structure, using principal components. *Applied Statistics* 36(1): 22-33.

Lang, M., Lichtenthaler, H. K., Sowinska, M., Heisel, F., and Miehe, J. A. 1996. Fluorescence imaging of water and temperature stress in plant leaves. *Journal of Plant Physiology* 148: 613-621.

Leemans, V., Magein, H., and Destain, M. F. 1998. Defects segmentation on 'Golden Delicious' apples by using colour machine vision. *Computers and Electronics in Agriculture* 20(2): 117-130.

Leemans, V., Magein, H., and Destain, M. F. 1999. Defect segmentation on 'Jonagold' apples using colour vision and a Bayesian classification method. *Computers and Electronics in Agriculture* 23(1): 43-53.

Li, Q., Wang, M., and Gu, W. 2002. Computer vision based system for apple surface defect detection. *Computers and Electronics in Agriculture* 36: 215-223.

Lichtenthaler, H. K., lang, M., Sowinska, M., Heisel, F., and Miehe, J. A. 1996. Detection of vegetation stress via a new high resolution fluorescence imaging system. *Journal of Plant Physiology* 148: 599-612.

Lott, R. V. 1943. Some spectral curves of maturing apples. *Proceedings of the American Society for Horticultural Science* 43: 59-62.

Lu, R. 2003. Detection bruises on apples using near-infrared hyperspectral imaging. *Transactions of the ASAE* 46(2): 523-530.

Mak, B., and Blanning, R. W. 1998. An empirical measure of element contribution in neural networks. *IEEE Transactions on Systems, Man, Cybernetics. C* 28(4): 561-564.

McCabe, G. P. 1984. Principal Variables. *Technometrics* 26(2): 137-144.

Meheriuk, M., Prange, R. K., Lidster, P. D., and Porritt, S. W. 1994. *Postharvest disorders of apples and pears*. Agric. Canada Publication 1737/E, Ottawa, Canada.

Mehl, P. M., Chao, K., Kim, M., and Chen, Y. R. 2002. Detection of defects on selected apple cultivars using hyperspectral and multispectral image analysis. *Applied Engineering in Agriculture* 18(2): 219-226.

Meyer, S., and Gentry, B. 1998. Mapping intercellular CO2 mole fraction (Ci) in Rosa rubiginosa leaves fed with abscisic acid by using chlorophyll fluorescence imaging. *Plant Physiology* 116: 947-957.

Micheli-Tzanakou, E. 2000. *Supervised and unsupervised pattern recognition: feature extraction and computational intelligence*. CRC Press, Boca Raton, Florida.

Miller, W. M., Throop, J. A., and Upchurch, B. L. 1998. Pattern recognition models for spectral reflectance evaluation of apple blemishes. *Postharvest Biology and Technology* 14(1): 11-20.

Mir, N., Wendorf, M., Perez, R., and Beaudry, R. M. 1998. Chlorophyll fluorescence in relation to superficial scald development in apple. *Journal of the American Society for Horticultural Science* 123(5): 887-892.

Mucciardi, A. N., and Gose, E. E. 1971. A comparison of seven techniques for choosing subsets of pattern recognition properties. *IEEE Transactions on Computers* C-20(9): 1023-1031.

Muir, A. 1993. Machine vision and spectral imaging. *Agricultural Engineer* 48(4): 124.

Muir, A. Y., Shirlaw, A. D. G., and McRae, D. C. 1989. Machine vision using spectral imaging techniques. *Agricultural Engineer* 44(3): 79-81.

Nakano, K. 1997. Application of neural networks to the color grading of apples. *Computers and Electronics in Agriculture* 18(2-3): 105-116.

Narendra, P. M., and Fukunaga, K. 1977. A branch and bound algorithm for feature subset selection. *IEEE Transactions on Computers* C-26(9): 917-922.

Nath, R., Rajagopalan, B., and Ryker, R. 1997. Determining the saliency of input variables in neural network classifier. *Computers and Operations Research* 24: 767-773.

Nedbal, L., Soukupova, J., Whitmarsh, J., and Trtilek, M. 2000. Postharvest imaging of chlorophyll fluorescence from lemons can be used to predict fruit quality. *Photosynthetica* 38(4): 571-579.

Omasa, K., Shimazaki, K. I., and Aiga, I. 1987. Image analysis of chlorophyll fluorescence transients for diagnosing the photosynthetic system of attached leaves. *Plant Physiology* 84: 748-752.

Park, B., Chen, Y. R., and Nguyen, M. 1998. Multi-spectral image analysis using neural network algorithm for inspection of poultry carcasses. *Journal of Agricultural Engineering Research* 69(4): 351-363.

Pen, C. L., Bilanski, W. K., and Fuzzen, D. R. 1985. Classification analysis of good and bruised peeled apple tissue using optical reflectance. *Transactions of the ASAE* 18(1): 326-330.

Pierson, C. F., Ceponis, M. J., and McColloch, L. P. 1971. *Market diseases of apples, pears, and quinces*. Agricultural Research Service, USDA.

Polder, G., Heijden, G. W. A. M., and Young, I. T. 2002. Spectral image analysis for measuring ripeness of tomatoes. *Transactions of the ASAE* 45(4): 1155-1161.

Rehkugler, G. E., and Throop, J. A. 1986. Apple sorting with machine vision. *Transactions of the ASAE* 29(5): 1388-1397.

Rehkugler, G. E., and Throop, J. A. 1989. Image processing algorithm for apple defect detection. *Transactions of the ASAE* 32(1): 267-272.

Reid, W. S. 1976. Optical detection for skin, bruise flesh, stem, calyx. *Journal of Agricultural Engineering Research* 21(3): 291-295.

Rumelhart, D. E., Hinton, G. E., and Williams, R. J. 1986. Learning representations of back-propagation errors. *Nature (London)* 323: 533-536.

Schalkoff, R. 1992. *Pattern Recognition : Statistical, Structural, and Neural Approaches*. John Wiley & Sons, Inc., New York.

Shaw, G., and Manolakis, D. 2002. Signal processing for hyperspectral image exploitation. In *IEEE Signal Processing Magazine*, January, pp. 12-16.

Song, J., Deng, W., and Beaudry, R. M. 1997. Changes in chlorophyll fluorescence of apple fruit during maturation, ripening, and senescence. *HortScience* 32(5): 891-896.

Song, J., Fan, L., Forney, C. F., and Jordan, M. A. 2001. Using volatile emissions and chlorophyll fluorescence as indicators of heat injury in apples. *Journal of the American Society for Horticultural Science* 126(6): 771-777.

Steinmetz, V., Roger, J. M., Molto, E., and Blasco, J. 1999. On-line fusion of colour camera and spectrophotometer for sugar content prediction of apples. *Journal of Agricultural Engineering Research* 73: 207-216.

Sugar, D. 2002. Management of postharvest diseases. In *Fruit quality and its biological basis* (M. Knee, ed.). CRC Press LLC, Boca Raton, FL.

Taiz, L., and Zeiger, E. 1998. *Plant physiology*. second/Ed. Sinauer Associates, Inc., Sunderland, Massachusetts.

Tao, Y., Heinemann, P. H., Varghese, Z., Morrow, C. T., and III, H. J. S. 1995. Machine vision for color inspection of potatoes and apples. *Transactions of the ASAE* 38(5): 1555-1561.

Tao, Y., and Wen, Z. 1999. An adaptive spherical image transform for high-speed fruit defect detection. *Transactions of the ASAE* 42(1): 241-246.

Throop, J. A., Aneshansley, D. J., and Upchurch, B. L. 1995. Coocurence texture feature variation for a moving window over apple images. In *Optics in agriculture, forestry, and biological processing* (J. A. DeShazer and G. E. Meyer, eds.), Vol. 2345. Proc SPIE.

Upchurch, B. L., Affeldt, H. A., Hruschka, W. R., Norris, K. H., and Throop, J. A. 1990. Spectrophotometric study of bruises on whole Red Delicious apples. *Transactions of the ASAE* 33(2): 585-589.

Upchurch, B. L., Affeldt, H. A., Hruschka, W. R., Norris, K. H., and Throop, J. A. 1991. Optical detection of bruises and early frost damage on apples. *Transactions of the ASAE* 34(3): 1004-1009.

Wen, Z., and Tao, Y. 2000. Dual-camera NIR/MIR imaging for stem-end/calyx identification in apple defect sorting. *Transactions of the ASAE* 43(2): 449-452.

Williams, P., and Norris, K., eds. 1987. "Near-Infrared Technology in the Agricultural and Food Industries,". American Association of Cereal Chemists, St. Paul, MN.

Wills, R., McGlasson, B., Graham, D., and Joyce, D. 1998. *Postharvest: An introduction to the physiology and handling of fruits, vegetables, and ornamentals*. 4th/Ed. CAB International, New York.

Wills, R. B. H., and Scott, K. J. 1982. Use of dips containing diphenylamine and edible oils to reduce soft scald of apples. *HortScience* 17(6): 964-965.

Yang, Q. 1993. Finding stalk and calyx of apples using structured lighting. *Computers and Electronics in Agriculture* 8: 31-42.

Yang, Q. 1994. An approach to apple surface feature detection by machine vision. *Computers and Electronics in Agriculture* 11(2/3): 249-264.

Yang, Q. S., and Marchant, J. A. 1996. Accurate blemish detection with active contour models. *Computers and Electronics in Agriculture* 14(1): 77-89.